# Accuracy of Image Guided Robotic Assistance
# in Cochlear Implant Surgery

Von der Fakultät für Maschinenbau
der Gottfried Wilhelm Leibniz Universität Hannover
zur Erlangung des akademischen Grades
Doktor-Ingenieur
genehmigte

**Dissertation**

von
Dipl.-Ing. Hubertus Eilers
geboren am 05. November 1977
in Georgsmarienhütte

2011

1. Referent:      Prof. Dr.-Ing. T. Ortmaier
2. Referent:      Prof. Dr.-Ing. habil. Dr. h.c. Prof. E.h. B. Heimann
3. Referent:      Prof. Dr.-Ing. E. Reithmeier

Tag der Promotion:  15.12.2011

# Vorwort

# Abstract

Cochlear implant surgery is a medical discipline, which is characterized by a high degree of demanded accuracy because of the sensitive anatomical structures that are located in direct proximity to the operating area. The standard surgical approach to get access to the cochlea includes extensive milling to remove large parts of the temporal bone. In this context, a minimally invasive approach to reduce the invasiveness would have numerous advantages. However, this also requires the use of technological assistance systems to maintain the demanded level of accuracy. To assess the feasibility, information about the system's performance in terms of an expected error is crucial and needs to be investigated thoroughly.

The concept investigated in this thesis consists of a robot which is used to drill a minimally invasive canal from the surface of the mastoid straight to the basal turn of the cochlea. This task cannot be performed manually since anatomic landmarks, which are used during the traditional surgical intervention to guide a safe way towards the target, remain hidden within the temporal bone. Therefore, they are not visible to the surgeon. To face this challenge, image guided surgery (IGS) is used to locate anatomical structures and to prevent them from being violated by the drill. This concept includes that the drill canal is defined in preoperatively acquired CT image data. Sensitive areas such as the facial nerve and the chorda tympani nerve need to be identified and sufficient safety margins have to be established between the canal's outer wall and these structures. Afterwards, the planning data is mapped to the intraoperative situation with the help of artificial landmarks. Thus, moving commands according to the drill path are calculated for the robot. Additionally, an optical localizer is used during drilling to acquire actual pose information about the instrument, the robot and the patient. This information is used in a closed loop control to adjust the pose of the surgical drill.

This work examines the inaccuracies that are involved in the described concept in a theoretical and experimental way. A mathematical error description is used that accounts for the statistical distribution of errors that occur especially during target point localization, drill localization, and positioning of the instrument, respectively. The expected error distribution is further compared to experimental results in order to verify the applicability of the theoretical model. The acquired information about the system's inaccuracy has an impact on the planning process. Consequently, a method which allows optimizing the drill path coordinates is presented, that takes individual priorities of the anatomic structures into consideration. The feasibility of the minimally invasive concept is finally evaluated in experimental studies on temporal bone specimens. The results show that the observed deviations between the drilled canal and its intended location at the entry point can be well predicted by the error model. Nevertheless, further improvements to the accuracy of this concept are necessary before bringing this concept to the operating theater.

**Keywords:** Robot assisted surgery, image guided surgery, cochlear implant, accuracy assessment.

# Kurzfassung

Die Cochlea Implantation stellt einen chirurgischen Eingriff zur Behandlung innenohrbedingter Taubheit dar, der aufgrund der unmittelbaren Nähe des Operationsgebietes zu sensitiven anatomischen Strukturen hohe Anforderungen an die Genauigkeit des Eingriffs stellt. Das klassische Vorgehen beinhaltet unter anderem großvolumiges Fräsen an der seitlichen Schädelbasis, um Zugang zur Hörschnecke (Cochlea) zu erhalten. Ein minimalinvasiver Ansatz zur Reduzierung der Invasivität besitzt zahlreiche Vorteile, erfordert jedoch den Einsatz technischer Assistenzsysteme, um die geforderte Genauigkeit sicher zu stellen. Für die Bewertung eines solchen Ansatzes sind Informationen über die zu erwartende Systemgenauigkeit unerlässlich.

Im Rahmen dieser Arbeit wird ein Ansatz zur Umsetzung eines minimalinvasiven Zugangs untersucht, der aus einem kleinen Kanal besteht, der mit Hilfe eines Roboters von der Schädeloberfläche zur Cochlea gebohrt wird. Ein solcher Zugang kann nicht rein manuell angelegt werden, da wichtige Orientierungspunkte im Felsenbein verborgen bleiben und somit nicht für den Chirurgen sichtbar sind. Das Konzept der bildgeführten Chirurgie (*Image Guided Surgery, IGS*) stellt in diesem Zusammenhang einen Lösungsansatz für dieses Problem dar. Der Bohrkanal wird in präoperativen CT-Bilddaten definiert, wobei anatomisch sensitive Strukturen wie beispielsweise der Gesichts- oder Geschmacksnerv bei der Planung identifiziert und mit einem ausreichenden Sicherheitsabstand zur Außenwandung des Kanals versehen werden. Mit Hilfe künstlicher Landmarken werden die Planungsdaten anschließend auf die intra-operative Situation abgebildet, sodass der Roboter zur Führung des Bohrers entsprechend angesteuert werden kann. Hierzu werden während des Bohrvorgangs die Lagen des Roboters, des Instruments und des Patienten kontinuierlich erfasst und für eine Positionsregelung verwendet.

Das vorgestellte Konzept zur Umsetzung des minimalinvasiven Zugangs wird in Hinblick auf die zu erwartende Systemgenauigkeit theoretisch und experimentell untersucht. In diesem Zusammenhang findet ein mathematisches Fehlermodell Verwendung, das die statistische Verteilung der Abweichungen berücksichtigt, die während der Lokalisation der Zielstrukturen und des Bohrers, sowie bei der Instrumentenführung auftreten. Um die Aussagekraft des Fehlermodells zu überprüfen, wird der ermittelte Erwartungswert der Systemgenauigkeit mit Ergebnissen aus experimentellen Untersuchungen verglichen. Darüber hinaus werden die gewonnenen Informationen für eine Optimierung der Bahnplanung bezüglich vorhandener Sicherheitsabstände verwendet. Hierzu werden die Koordinaten des Bohrkanals unter Berücksichtigung individueller Prioritäten angrenzender Strukturen optimiert. Das Gesamtkonzept wird abschließend an einer Reihe von Felsenbeinpräparaten experimentell getestet und ausgewertet. Die Ergebnisse zeigen, dass die Abweichungen des Bohrkanals am Eintrittspunkt korrekt durch das Fehlermodell vorhergesagt werden können. Nichtsdestotrotz ist eine Verbesserung der Systemgenauigkeit notwendig, bevor das Konzept am Patienten getestet werden kann.

**Schlagwörter:** Roboter assistierte Chirurgie, bildgeführte Chirurgie, Cochlea Implantat, Genauigkeitsanalyse.

# Contents

# List of Figures

# List of Tables

# List of Abbreviations, Definitions and Notation

**Abbreviations**

| | |
|---|---|
| 2D | Two-dimensional |
| 3D | Three-dimensional |
| FLE | Fiducial Localization Error |
| FRE | Fiducial Registration Error |
| MLE | Marker Localization Error |
| ART | Advanced Realtime Tracking GmbH |
| CAS | Computer Assisted Surgery |
| CF | Coordinate Frame |
| CI | Cochlear Implant |
| CMM | Coordinate Measuring Machine |
| CNC | Computerized Numerical Control |
| CRF | Coordinate Reference Frame |
| CT | Computed Tomography |
| DICOM | Digital Imaging and Communications in Medicine |
| DOF | Degrees of Freedom |
| EAS | Electrical and Acoustic Stimulation |
| HMI | Human-Machine-Interface |
| IGS | Image Guided Surgery |
| IR | Infra-Red |
| LED | Light Emitting Diode |
| LPS | Left-Posterior-Superior |
| mCIS | Minimally Invasive Approach to Cochlea Implant Surgery |
| MIS | Minimally Invasive Surgery |
| MPTA | Mastoidectomy Posterior Tympanotomy Approach |
| MRI | Magnetic Resonance Imaging |
| MSCT | Multi Slice Computed Tomography |
| MTF | Modulated Transfer Function |
| NDI | Northern Digital Inc. |
| NIH | U.S. National Institute of Health |
| OCT | Optical Coherence Tomography |
| PACS | Picture Archiving and Communication System |
| PMMA | Poly Methyl Methacrylate |
| POI | Point of Interest |
| QALY | Quality Adjusted Life Years |

| | |
|---|---|
| RAS | Robot Assisted Surgery |
| RMS | Root Mean Square |
| SD | Standard Deviation |
| STL | Surface Tessellation Language |
| SVD | Singular Value Decomposition |
| TB | Temporal Bone |
| TCP | Tool Center Point |
| TNE | Target Navigation Error |
| TRE | Target Registration Error |
| VCT | Volume Computed Tomography |
| VTK | Visualization Toolkit |

**Definitions**

| | |
|---|---|
| accuracy | Accuracy as defined in DIN ISO 5725 |
| fiducial point | Reference point used for registration purposes |
| pose | Position and orientation of an object |
| precision | Precision as defined in DIN ISO 5725 |
| trueness | Trueness as defined in DIN ISO 5725 |

**Notation**

| | |
|---|---|
| $\Delta$ | Error in positioning of an instrument |
| $\varepsilon_{\text{tool}}$ | Calibration error of a tool |
| $\gamma$ | Anisotropic relation factor |
| $\psi_I$ | Insertion angle |
| $\theta$ | Angular variable |
| $d(p_i, S_j)$ | Distance between point $p_i$ and anatomic structure $S_j$ |
| $g_1$ | Grid spacing parameter |
| $h(\theta)$ | Height function of a spiral |
| $\bar{\mathbf{p}}$ | Centroid of a weighted sum of fiducial points |
| $\tilde{p}_i$ | Distance of a fiducial point $i$ to the centroid $\bar{\mathbf{p}}$ |
| $r(\theta)$ | Radius function of a spiral |
| $\mathbf{t}_{\text{A}\rightarrow\text{B}}$ | Translational vector. $\mathbf{t}_{\text{A}\rightarrow\text{B}} \in \mathbb{R}^{3\times 1}$ |
| $_{(\text{A})}\mathbf{x}_{\text{P}}$ | Homogeneous position vector of $P$ in $CF_{\text{A}}$ |
| $\hat{x}$ | True value of the observed value $x$ |
| $\langle x \rangle$ | Expected value of $x$ |
| $\bar{D}_S(A, B)$ | Mean absolute surface distance between objects $A$ and $B$ |
| $_{\text{A}}\text{FLE}_i$ | FLE of the fiducial point $i$ in $CF_{\text{A}}$ |
| $H(A, B)$ | Hausdorff distance between objects $A$ and $B$ |
| $^{\text{A}}\mathbf{R}_{\text{B}}$ | Rotation matrix |
| $^{\text{A}}\mathbf{T}_{\text{A}}$ | Homogeneous transformation. $_{(\text{A})}\mathbf{x}_{\text{P}} =^{\text{A}} \mathbf{T}_{\text{A}}\ {}_{(\text{A})}\mathbf{x}_{\text{P}}$. |

# 1 Introduction

From the very beginning of surgical interventions, various types of technological assistance systems have been used in order to ensure a maximum level of safety as well as an optimal surgical result for the patient. This progress was pushed particularly by the introduction of new imaging technologies such as computed tomography (CT) in the 1970s and the increasing calculational power of personal computers in the 1980s [Hou73]. The introduction of Computer Assisted Surgery (CAS) gave the possibility of planning and simulating surgical interventions based on preoperative images of the patient. Thus, the surgeons were able to specify the location of a structure, e.g. a tumor within these images, and perform the required surgical intervention with a better outcome for the patient. The first systems displaying the acquired image information during a surgical intervention, were introduced by ROBERTS ET AL. in 1986 [RSH+86]. Their approach was to overlay the image of an operating microscope with additional tomographic images of the patient in order to guide the surgeon to the target structure. Hence, the first assistance system of a new surgical technique, called *Image Guided Surgery* (IGS) was established. The principle of IGS includes a continuous localization of the surgical instrument and the patient as well as a mapping of the patient's image data to the intraoperative situation. This information is used to give feedback to the surgeon about the instrument's actual pose[1] in relation to adjacent anatomic structures. Nowadays, IGS is a common technique in the operating theater. Its realization can be characterized by five different tasks, which have to be performed [GP08]:

1. preoperative image acquisition

2. intraoperative localization of the instrument

3. intraoperative registration of the localizer volume (i.e. navigation system) with the image data

4. display of the instrument's pose within the image data

5. consideration of changes between image data and intraoperative reality

The development of IGS was furthered by the success of minimally invasive surgery (MIS). The use of IGS allows the surgeon to operate through minimally invasive incisions without the need of a direct view to the instrument's tip. Instead, its current pose is visualized on a computer screen in relation to the surrounding anatomy of the patient. Vitally important anatomic areas can therefore be easily identified and secured by the surgeon, which enhances the safety of the intervention. Applications of IGS can be found in numerous interventions: from the removal of tumors in

---

[1]Throughout this thesis, the term pose is used to describe the position and orientation of an object.

neurosurgery, to the placement of implants in maxillo-facial surgery, to cardiac or orthopaedic surgery [PS02].

A further development of this principle is the integration of robotic devices into the surgical procedure in order to guide the instrument with a higher precision than the surgeon is able to perform manually. This so called Robot Assisted Surgery (RAS) has been a field of intensive research in the last two decades. The common goal is to develop a surgical assistance system which increases the safety and accuracy of a surgical intervention by reducing its invasiveness at the same time. In this way, new types of interventions can be developed in order to enhance the possibilities of surgical treatment and to get the patient recovering from his disease as fast as possible.

## 1.1 Accuracy in IGS

One of the most important tasks in IGS is maintaining the highest possible accuracy during tissue manipulation. Especially in the presence of anatomically important structures which need to be preserved during surgery (i.e. blood vessels and nerves), the reliability and accuracy of the information obtained by the IGS system is crucial to the success of the intervention. Any measuring error which yields to a displacement of the instrument from its desired pose can cause serious injuries if the instrument is moved too close to these structures. Therefore, the accuracy of an IGS system needs to be examined carefully prior to using it in the operating room. In the context of this thesis, the term accuracy is defined according to international standard ISO 5725, incorporating two properties: trueness and precision:

> "*Trueness* refers to the closeness of agreement between the arithmetic mean of a large number of test results and the true or accepted reference value. *Precision* refers to the closeness of agreement between test results. [...] The general term *accuracy* is used in ISO 5725 to refer to both trueness and precision." [ISO04]

In order to quantify trueness, the mean or median value is normally used, whereas precision is described by the variance or covariance of the measurement data. Concerning accuracy in IGS, a lot of different notations and definitions can be found in the literature. This is further complicated by the fact that the terms 'accuracy' and 'precision' are often misleadingly used with the same meaning. The main deficit from a clinical point of view is that no commonly accepted regulation exists that defines the conditions for the determination of an IGS system's accuracy [SHK+06]. As a consequence, a lot of contributions cannot be compared to others due to their different individual conditions.

The most common term used in the literature to express application accuracy in IGS is the Target Registration Error (TRE), introduced by MAURER ET AL. [MMF93]. It represents the distance between two points, with the first point being the point of interest, which is defined in image space in order to mark a target for a surgeon. During IGS, the image space is mapped to the intraoperative situation by means of aligning reference points (registration landmarks) in both spaces, which is inherently affected by errors. The second point is the true location of the target

in physical space. If the surgeon tries to locate the target as implied by the IGS system, an error occurs, which can be quantified by the Euclidean distance from the assumed to the true location of the target. Figure 1.1 depicts this error.
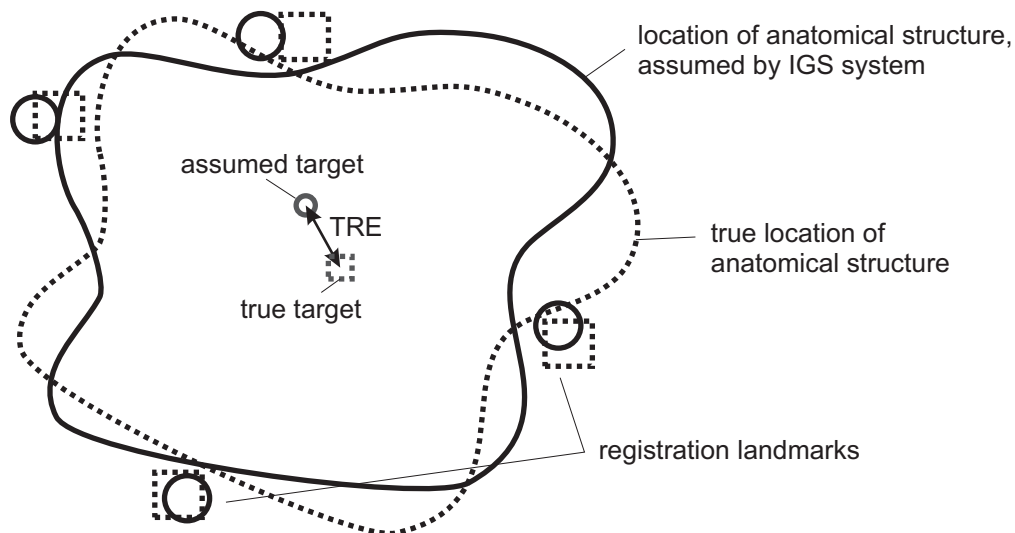


**Figure 1.1:** Illustration of the target registration error (TRE). The assumed target point does not correspond to its true location in physical space due to errors in the localization and registration process.

Although the goals of IGS are the same in many different medical applications, the designs of the instruments as well as the whole setup of the surgical interventions are unique and differ for each application. This means that the accuracy performance of IGS is always subject to a particular surgical intervention and can be affected by a variety of errors. This effect is embodied in the broadly varying values of the accuracy of IGS applications that can be found in the literature. For instance, a TRE of approximately 1.0 mm [SKR$^+$05] is documented as well as a TRE of up to 7.2 mm [SJSS09]. A comparison of these values is not meaningful, since they refer to different surgical workflows. A significant accuracy assessment of IGS technology is a very complex procedure and needs to be adapted individually to the target application [WTF04].

## 1.2  IGS in Cochlear Implant Surgery

Surgical interventions demanding a high degree of accuracy can be found especially in domains relating to the head, since a lot of delicate structures such as nerves, blood vessels and the brain are located in direct proximity to each other. The human sense of hearing is an example of a complex process in order to create a specific impression for the brain according to a sound reaching the ear. It requires interaction of various anatomic structures of extraordinary small size. In Germany approximately 12 million people are severely to profoundly hearing impaired and require surgical treatment. In 10 million cases the reason can be found in a degeneration of hair cells caused by

genetic defects, infectious diseases or excessive noise [Len08]. However, in 98 % of these cases the auditory nerve stays intact, so that a hearing aid can be implanted into the ear in order to substitute for the function of the hair cells. Since the consensus conference of the U.S. National Institutes of Health (NIH) in 1995, cochlear implantation is accepted to be the most suitable treatment for patients with severe hearing impairment [NIH95]. A cochlear implant (CI) is a hearing aid, which is implanted into the windings of the inner ear (cochlea). It stimulates the auditory nerve electrically with the help of small electrodes, which are part of the implant. The surgical intervention needs to be performed with high accuracy, since delicate anatomic structures are located in direct proximity to the cochlea.

### 1.2.1 Process of Normal Hearing

The ability to perceive sound is a complex interactive process of various anatomic structures. Sound waves traveling through the air enter the auditory canal and cause vibrations of the tympanic membrane. These movements in turn are transmitted to the attached ossicles, consisting of three small bones, called the malleus, incus and stapes (see Figure 1.2). They are the smallest bones of the human body and are located in the tympanum, a cavity within the skull base. The shape and the suspension of the ossicles are realized in such a way that an impedance matching is performed and vibrations from the tympanic membrane are optimally transmitted to the entrance membrane of the inner ear, called the oval window. Additionally, properties of the acoustic transmission can be adapted individually to the actual situation. For example, during excessive noise, attached muscles may stiffen the ossicles, resulting in a damped transmission. Thus, the transfer of vibrations is muffled and less acoustic energy is transmitted to the inner ear (cochlea) preventing it from damage (tympanic reflex). Approximately 60% of the acoustic energy reaches the cochlea via the oval window, which is a membrane located at the base of the inner ear and connected to the footplate of the stapes [Zen07]. The cochlea itself is shaped like a snail containing 2.5 tubular windings. Its internal structure can be divided into three compartments, named scala tympani, scala media and scala vestibuli. The scala tympani and the scala vestibuli are connected to each other at the top of the cochlea (helicotrema). They are filled with watery liquid, which is moving due to the vibrations of the oval window. As a result a wandering wave propagates along the basilar membrane, which separates the scala tympani and scala vestibuli. The mechanical properties of the basilar membrane are designed in a way that a maximum magnitude of displacement develops at a certain location within the cochlea depending on the frequency of the received sound. The motion of the basilar membrane is sensed by thousands of hair cells, which are located within the scala vestibuli. Through a complex molecular cascade the auditory nerve is stimulated and a hearing impression is sent to the brain.

### 1.2.2 History and Functionality of Cochlear Implants

In 1790, ALLESSANDRO VOLTA discovered, that an electrical stimulation is able to create a hearing impression [Blu10]. The first stimulation of the auditory nerve using an electrode was done in
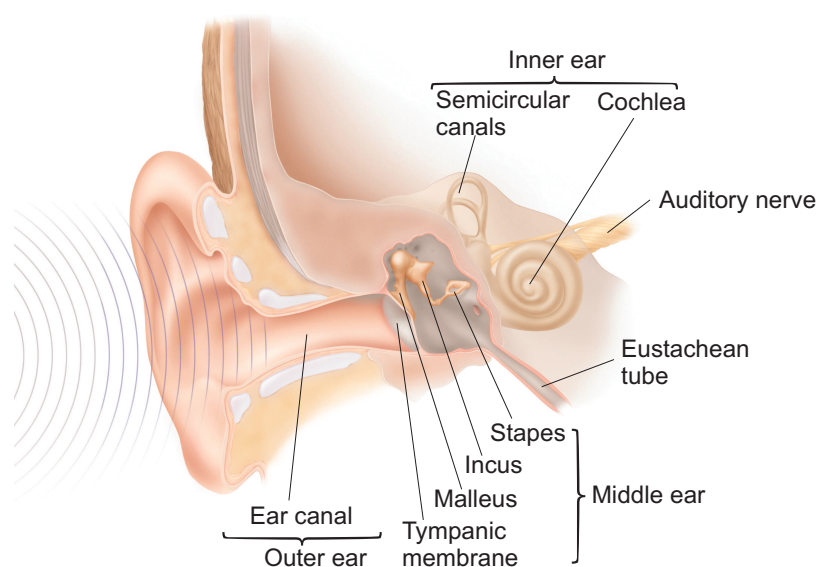
**Figure 1.2:** Anatomy of the ear (figure of the ear: courtesy of Cochlear Ltd., Australia)

the 1950s by DJOURNO ET AL. [Djo53]. That was the beginning of cochlear implant surgery and the technology of cochlear implants has been greatly improved since that time. Another historical landmark was in 1981, when the first digital multi-channel implant was developed by CLARK ET AL. [CT81]. Today's cochlear implants consist of three main components (see Figure 1.3). With the help of a microphone, sound is detected and processed by a speech processor suitably for the requirements of the implant. The signals are transmitted to a receiver, which is implanted under the skin within the skull behind the ear. This receiver converts the signal into electrical impulses and forwards them to the electrode array, which is located in the cochlea close to the auditory nerve. State of the art arrays contain up to 24 electrodes, which are used to create the hearing impression via electrical stimulation of the auditory nerve. With the help of a CI patients are able to understand spoken words or listen to music. Children with pre-lingual deafness are even able to acquire spoken language if implanted at an early age.

Besides this ethical effect, cochlear implantation is also a procedure with a high degree of socio-economic relevance. Worldwide 188,000 patients have received a cochlear implant by April 2009 [NIC09]. The costs of a cochlear implantation are estimated to be approximately $60,000[2]. In comparison, socioeconomic costs related to a deaf child are evaluated to be more than $1 million[3] [NIH06]. Other surveys indicate the cost effectiveness of cochlear implants by calculating the amount of quality-adjusted life years (QALYs). The sum of gained QALYs are an indicator of the benefit which has been gained by a medical treatment in quality and quantity of life. In terms of cochlear implantation, the mean cost for gaining a QALY are even lower when highest priority is given to young children with great loss of hearing [BSFS06]. These studies demonstrate that

---

[2]$60,000 = €43,038 (11.10.2010).

[3]$1,000,000 = €717,300 (11.10.2010).
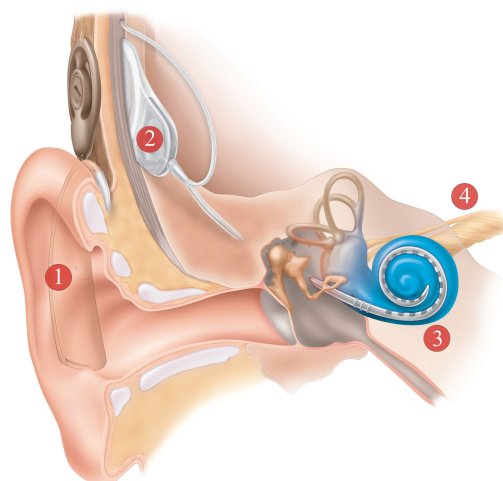
**Figure 1.3:** Cochlea implant system (courtesy of Cochlear Ltd., Australia). A speech processor (1) receives acoustic signals via microphone and transmits the encoded audio signals to the internal receiver (2), which forwards them to the intra-cochlea placed electrode-array (3). Thus, the auditory nerve (4) is stimulated.

beside the social benefit of the patient, cochlear implant surgery has also a financial benefit for the economy. Consequently, a lot of research is done in order to improve the functional outcome as well as to reduce the invasiveness of the surgical procedure.

### 1.2.3 Traditional Approach in Cochlear Implant Surgery (CIS)

The standardized surgical procedure of cochlear implantation takes approximately $2-3$ hours and is performed under general anesthesia. The intervention is characterized by extensive milling, since the cochlea is embedded within the temporal bone (a compartment of the lateral skull base) at a depth of approximately 30 mm. The most common method to gain access to the cochlea is the so called mastoidectomy posterior tympanotomy approach (MPTA). It can be divided into three main steps: the mastoidectomy, the posterior tympanotomy, and the cochleostomy [Len06]. Each step is described in detail in the following.

### Step 1: Mastoidectomy

The mastoidectomy is the most time consuming step of cochlear implantation and consists of removing parts of the temporal bone between the surface and the inner ear. During milling, the surgeon needs to localize functionally important structures such as the sigmoid sinus, the carotid artery, the outer wall of the ear canal, the facial nerve, the chorda tympani nerve, and the labyrinth, in order to protect them from damage. For example, a puncture of the sigmoid sinus and carotid artery, which are high-volume blood vessels, would lead to excessive bleeding which is usually fatal for the patient. Any damage to the chorda tympani nerve would lead to a limitation of the taste

sense, since this nerve serves the taste buds in the front of the tongue. A very delicate structure is the facial nerve, which innervates the facial muscles. It needs to be kept intact in order to preserve control of facial expression including the ability to close the eye lid. Unfortunately, it is located in direct proximity to the milling area. Thus, it is given the highest priority in terms of preventing it from damage. During mastoidectomy, the surgeon resects large parts of the mastoid, until these structures are skeletonized but not harmed. This is done in order to ensure their safety, but also for orientation purposes. For instance, the chorda tympani nerve together with the facial nerve serve as important anatomical landmarks for the surgeon to find the right access to the middle ear.

**Step 2: Posterior Tympanotomy**

The second step of the intervention is the posterior tympanotomy. A space of about $2.5 - 3$ mm between the facial nerve and the chorda tympani nerve, called the facial recess, is removed. In case of a very narrow facial recess, the surgeon has to decide if the chorda tympani has to be sacrificed in order to keep a minimum safety margin to the facial nerve. This is done in approximately 20 % of the cases [BGNO04]. After resecting the facial recess using a drill of $1.0 - 1.8$ mm, the surgeon enters the middle ear and acquires a view of the cochlear promontory, the stapes, and the round window niche (see Figure 1.4).
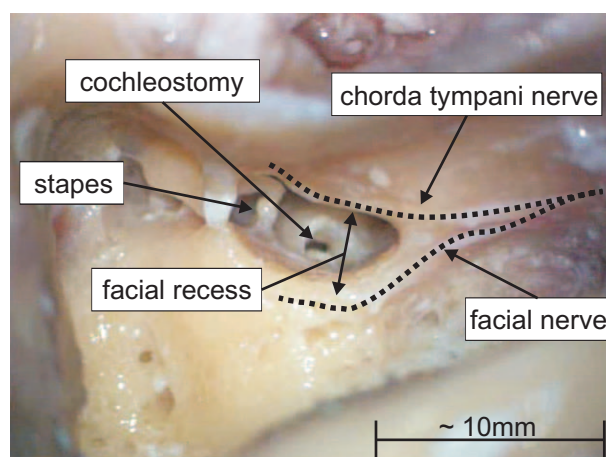


**Figure 1.4:** Picture of a temporal bone with MPTA and cochleostomy

**Step 3: Cochleostomy and Insertion**

The final step is the opening of the cochlea (cochleostomy). The surgeon uses a drill which is slightly larger than the outer diameter of the implant (approximately $0.8 - 1.0$ mm) and resects a part of the outer wall of the cochlea in order to gain access to the scala tympani. The size of the cochleostomy is $1.4 - 1.5$ mm and its position is considered to be anterior (to the front of the patient) and inferior (to the bottom of the patient) to the round window with involvement of the round window membrane [Len06]. The opening of the cochlea is one of the most crucial parts of

the intervention and needs to be performed with a precision of about 0.5 mm [SKA$^+$04]. With the use of MPTA the cochlea can be opened from a direction which is rather tangential to the basal turn of the cochlea. This enables a smooth insertion of the implant into the basal turn of the cochlea. To preserve the residual function of the inner ear, the insertion needs to be done carefully using the soft surgery technique [Leh93].

### 1.2.4 Minimally Invasive Approach in Cochlear Implant Surgery (mCIS)

Since cochlear implant surgery is dominated by tiny structures which need to be preserved during the intervention, IGS is adopted by several research groups. Besides safety aspects and accuracy, minimizing the invasiveness of the intervention is of special interest in this context. The main reasons can be found in a reduction of the operating time compared to conventional CI surgery as well as the postoperative recovery time of the patients. The biggest improvement can be achieved by avoiding the time consuming resection of bone during mastoidectomy. This can be achieved by redesigning the surgical procedure in a way that

- the removal of bone is minimized by means of establishing a direct access to the cochlea that is slightly larger than the implant (see Figure 1.5),

- all functionally important structures are preserved during the intervention and

- the implant can be inserted with a minimally invasive access using an appropriate tool.
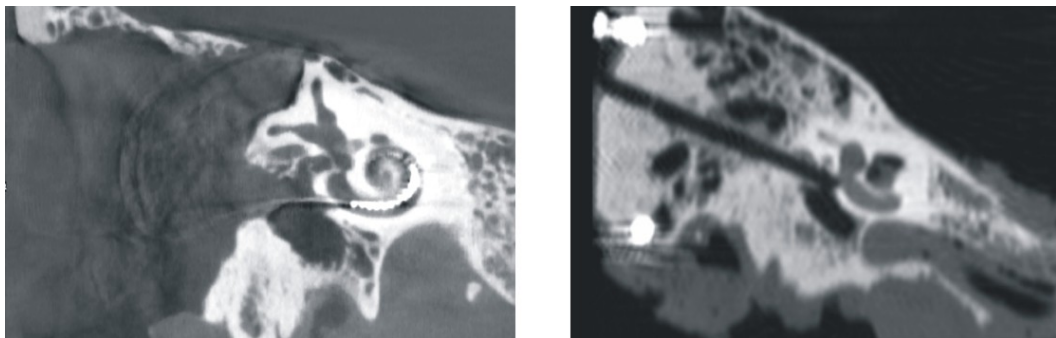


**Figure 1.5:** CT-slides of a traditional approach (left) and a minimally invasive approach (right) for cochlear implant surgery. Instead of resecting large parts of the mastoid, a single channel was drilled to access the cochlea.

This approach has, in contrast to the traditional approach (see Section 1.2.3), the consequence that no anatomical landmarks need to be skeletonized. Consequently, the location of the cochleostomy cannot be identified directly by the surgeon. In this case, IGS systems are able to provide the missing information. Since its introduction to otolaryngology by SCHLÖNDORFF ET AL. [SMME$^+$89], IGS has been an established intraoperative assistance system which is capable of compensating

for the loss of anatomic landmarks by using artificial substitutes. Using image guidance, information about the instrument's actual pose in relation to the preoperatively acquired image data is obtained. This information can be used in order to guide the surgical instrument to the target along a predefined path. However, maintaining the correct three-dimensional orientation during drilling is a very difficult task when done manually by checking the instructions displayed in a two-dimensional way on the IGS monitor. Any misinterpretation would lead to a deviation of the drill from its desired path and thus endanger the patient due to the very small safety margin. This is even more crucial if the drill has to be guided in direct proximity to vitally important structures, as during cochlea implantation. In order to cope with this drawback, robotic assistance can be used in order to precisely guide the instrument. By combining robotic assistance and IGS, a setup can be designed to realize a mCIS [MBL$^+$05, LBE$^+$07]. This states the central experimental approach which is examined in this thesis.

Cochlear implant surgery is considered as an important medical intervention, which can be improved by robotic applications due to its demands on the surgical accuracy [CRPB07]. Hence, numerous research groups are working on the integration of mechatronics into this field. Besides the mentioned approach of the Hannover group, LABADIE ET AL. are working on a setup which is capable of drilling a direct access via the mastoid towards the cochlea. Their approach uses a patient specific drill guide, which is affixed to the patient's head. In 2008, the system was tested successfully in a clinical setup of reduced functionality, to proof the concept [LND$^+$08].

Other groups are evaluating the use of robots in order to improve the quality of the cochleostomy. KLENZNER ET AL., for example, uses a surgical robot for the placement of the cochleostomy in order to improve the accuracy of its location [KNK$^+$09]. Maintaining an optimal cochleostomy is also investigated by BRETT ET AL. [BTP$^+$07] as well as by MANRIQUE ET AL. [MSCP$^+$07]. The common goal is to remove the outer bone tissue of the cochlea in a way that its delicate internal structure, i.e. the endosteal membrane, is kept intact. This is achieved with the help of special developed micro-manipulators. Furthermore, a robotic guided laser is used by BURGNER ET AL. for the cochleostomy instead of a surgical drill [BKK$^+$09].

Other approaches can be found in the literature that are related to the safety of the mastoidectomy. In [FGHP03], a robot with force feedback is presented which is used to drill cavities into human temporal bone specimens. Another approach is called Navigated Control$^®$. The power of a manually guided drill is controlled due to its pose estimated by an IGS system in relation to the surrounding anatomical structures [SDB$^+$08].

Besides getting optimal access to the cochlea, developing appropriate assistance systems for the insertion of the implant into the cochlea is also a field of research. ZHANG ET AL. present steerable electrodes with reduced forces applied to the internal structures of the cochlea during insertion [ZWM$^+$08]. An insertion tool, which is designed to be used through the mentioned minimally invasive access of this thesis has been developed by HUSSONG ET AL. Detailed information about this concept can be found in [HRE$^+$08].

## 1.3 Thesis Outline

As described in Section 1.2.4, mCIS is an example of a medical intervention which cannot be performed manually by the surgeon due to two main limitations. On the one hand, without performing a mastoidectomy, anatomic landmarks are missing. They are, however, necessary in order to guide the way for the surgeon towards the cochlea which is hidden within the temporal bone. On the other hand, the surgical procedure is characterized by a high degree of complexity and required accuracy in order to preserve important anatomical structures from damage. The use of robotic assistance and IGS states a possible solution for the implementation of an mCIS by means of drilling a direct channel to the basal turn of the cochlea. In this case, the accuracy of such an approach is of special interest and thus needs to be determined thoroughly.

In this thesis, the accuracy of a robotically performed mCIS is investigated. Therefore, an experimental setup is used consisting of an industrial robot, a surgical drill attached at its end effector, a stereo optical localizer, and a control workstation. The robot is controlled by the computer to guide the drill in accordance with continuously acquired localization data of an optical localizer. A closed loop control is used to establish a precise guidance according to the coordinates, which are defined in image data of the target.

This thesis is structured as follows. In Chapter 2, the principal workflow as well as the main components used in IGS applications and the current status of medical robotics are presented. Chapter 3 provides an overview of error definitions that are commonly used to describe the accuracy of IGS applications. Furthermore, experiments are presented in order to quantify the effect of different types of IGS components on the accuracy for the given experimental setup. Thus, the optimal configuration can be chosen in order to establish a high degree of accuracy during the navigation process and the overall error of the approach can be appraised. Therefore, the term 'target navigation error' (TNE) is introduced. Empirical TNE studies are presented in Chapter 4. Based on the statistical distribution of the TNE, consequences in terms of safety margins can be stated for the robot assisted IGS process. Chapter 5 presents a semi-automatic path planning approach. It allows for the definition of drilling coordinates in a three dimensional model of the temporal bone including segmentations of the most important structures. The start and target coordinates of the minimal invasive access are optimized, so that safety margins to the adjacent structures can be established according to their individual priority. The robot assisted mCIS approach is applied to a series of cadaveric specimens. The setup and results are presented and discussed in Chapter 6. Finally, a conclusion as well as research perspectives are given in Chapter 7.

# 2 Technological Aspects of a Robot Assisted mCIS Approach

The purpose of this chapter is to give an overview of the main technological components which are part of the robot assisted and image guided intervention of an mCIS. The principal workflow of IGS applications are presented in Section 2.1. The chronological order of an image guided process also illustrates the relation of each technology involved in the whole setup. In the following sections a closer look is taken at the core technologies of this approach. These are, in particular, the imaging modality (Section 2.2), the segmentation software (Section 2.3), the components of the intraoperative navigation process (Section 2.4), and the robot which is used to guide the drill (Section 2.5).

## 2.1 Workflow

The workflow of robot assisted IGS can basically be divided into three main phases, which are the preoperative, the intraoperative, and the postoperative phase. Apart from medical worksteps, each phase may be subdivided into the following technologically relevant steps [HML02] (see also Figure 2.1).
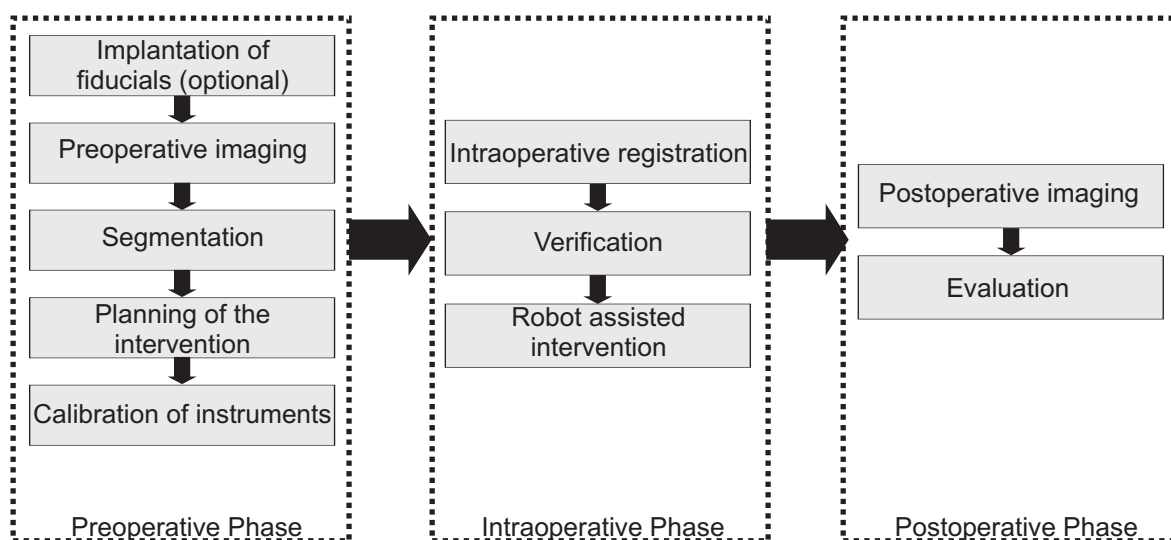


**Figure 2.1:** Workflow of a robot assisted IGS application

**Preoperative Phase**

- *Fixation of artificial fiducials (optional):* A geometric structure with at least three unique
  reference points (landmarks) is required that can be identified both in the image data of the
  patient as well as in the physical measurement volume of the localizer. I is used for the reg-
  istration step, which maps the image data to the intraoperative situation (see Section 2.4.3).
  These landmarks can either be anatomical structures or artificial markers. In the latter case,
  these have to be fixed in close proximity to the target structure on the body of the patient
  prior to imaging. This can be done, for example, by implanting titanium screws into the
  bone of the patient or by using skin affixed markers.

- *Preoperative imaging:* Three dimensional imaging of the target area is performed and usu-
  ally saved in a set of slice images. Thus, the surgeon is able to examine the patient's indi-
  vidual anatomy prior to the intervention and can decide on a definite surgical strategy.

- *Segmentation of the relevant anatomical structures (optional) and identification of each
  landmark's position:* With the help of segmentation software, relevant anatomical struc-
  tures can be delineated within the image data. This provides an overview of the shape and
  spatial distribution of these structures for the surgeon and helps identify them during the in-
  traoperative phase. Furthermore, the position of every landmark has to be identified within
  the coordinate system of the image data.

- *Planning of the intervention:* The anatomical area, which is targeted during the intervention,
  has to be defined within the image data. Concerning the mCIS, this planning step particu-
  larly includes the definition of entry and target coordinates for the drill canal. They have
  to be chosen so that the implant can be inserted while no anatomical structure is violated
  during the intervention.

- *Preoperative calibration of the instruments and the robot:* Localizers usually measure the
  point of interest of an object (e.g. the tip of an instrument) with the help of a reference
  structure. In the case of optical localization, a unique arrangement of reflective markers is
  used for this purpose. They are attached to each object which needs to be localized during
  the intervention. A calibration step has to be performed prior to the intervention in order
  to determine the spatial relationship between the object's point of interest and its reference
  adapter.

**Intraoperative Phase**

- *Registration of the patient:* As the patient is also equipped with a reference adapter, a correla-
  tion between the coordinate frame provided by this reference adapter and the preoperatively
  acquired image data needs to be determined. The registration step consists of measuring the
  location of landmarks and calculating a transformation which allows for an intra-operatively
  mapping of measured poses to the coordinates of the image data and vice versa.

- *Verification:* In order to check the success of the calibration as well as the registration step, a verification step is conducted by guiding the instrument to a specific point (e.g. a landmark) and checking its corresponding location.

- *Robot assisted intervention:* A robot can be used to guide the instrument in accordance with the level of automation defined for the intervention. During the operation, poses of the robot together with actual poses of the instrument as well as the patient are tracked permanently by the navigation system. This enables the robot to guide the instrument according to the surgical plan.

**Postoperative Phase**

- *Postoperative imaging (optional) and evaluation:* After finishing the operation, postoperative imaging is usually performed in order to evaluate the surgical outcome. Since intraoperative movements of the instruments are stored to disk, the intervention can be reproduced and analyzed at a later date.

Generally, each step of the workflow has an influence on the overall accuracy of the intervention and, therefore, affects the surgical outcome. From the technological point of view, the main components and the main sources of errors are the medical imaging unit, the segmentation and planning software, the navigation system, and the robot. These elements will be further introduced in the following sections.

## 2.2 Medical Imaging

With the help of a medical imaging unit the surgeon gets a view of the patient's anatomy prior to the intervention without the need to open his body. Besides two dimensional (2D) modalities such as X-ray imaging and ultrasound imaging, modalities exist providing three dimensional (3D) data sets of the imaged body section. 3D modality is necessary for the imaging of the temporal bone structures due to their complex spatial arrangement. Various types of imaging units exist for this purpose. Depending on their physical principle, the available technologies differ in terms of scanning volume, resolution, and image characteristics. Since each technology has its advantages as well as disadvantages, none of them can serve for all medical purposes [Wes09]. Very commonly used 3D imaging modalities are magnetic resonance imaging (MRI) and computed tomography (CT). Due to its functional principle MRI provides a great contrast resolution which is beneficial especially when scanning soft tissue. Nevertheless, the spatial resolution is generally lower compared to CT imaging. Thus, images of anatomy with naturally high contrast such as bony structures are usually of better quality when using CT technology.

**Computed Tomography**

CT is usually used in cochlea implant surgery, since the anatomical structures of the ear are embedded in bone and therefore provide natural high contrast for the imaging. The acquisition of 3D CT image data is based on a series of X-ray images which are taken from the target area, while the X-ray source and sensor elements are rotating on a gantry around the patient. Each X-ray image provides projections of the tissues' density distribution. Using these projections, slice images of the patient's anatomy can be computed with the help of an inverse Radon transform. Figure 2.2 depicts an experimental CT unit from GE Healthcare, located at the Göttingen University Hospital, as well as a reconstructed slice image of a temporal bone specimen.
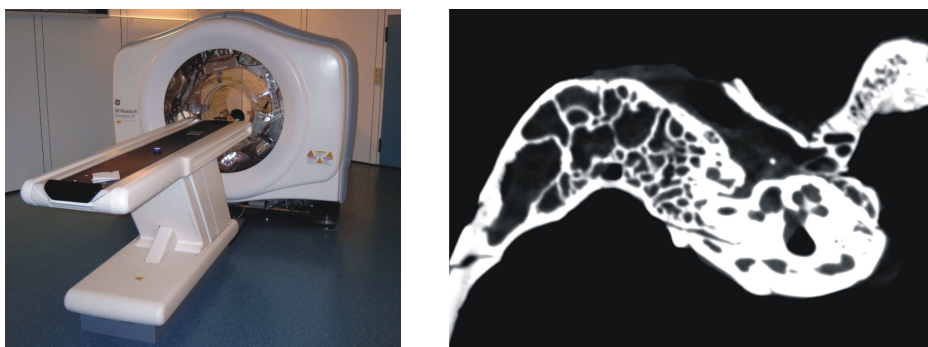


**Figure 2.2:** Left: experimental Volumetric CT from GE-Healthcare, located at Göttingen University Hospital. Right: reconstructed slice image of a temporal bone specimen.

Concerning the technology of image acquisition, current CT units can be divided into multi-slice CT (MSCT) and volume CT (VCT). MSCT scanners are commonly used in hospitals and usually consist of a number of detector elements arranged in rows (usually 4, 16, or 64) which are used to acquire the image information. The target is moved through the gantry during scanning, so that the scanning elements describe a helical trajectory around the object. Therefore, this type of CT is also called a spiral scan CT.

VCT is a technology under development that can provide a higher spatial resolution by replacing the rows of detector elements with a planar detector containing an 2D array of elements. Particularly with regard to the anatomy of the temporal bone, high resolution imaging may be necessary in order to visualize important structures, such as the chorda tympani nerve or the stapes. Section 3.3 provides more details concerning this aspect. In the context of this thesis, a prototype device of a flat-panel VCT (fpVCT, GE R&D, Schenectady, NY, USA) was used for pre-experimental imaging of temporal bone specimens. More detailed information about the principles of MSCT and VCT can be found in [Kal05] and [GGS+06], respectively.

**Image Representation**

After the acquisition, a set of slice images is reconstructed from the X-ray data and usually exported in DICOM (Digital Imaging and Communications in Medicine) format. DICOM is a stan-

dard data format used to handle medical image data by providing additional information about the imaging as well as a communication protocol. This allows for the integration of the data into a central picture archiving and communication system (PACS) and the processing on different computer architectures. Each slice image depicts a cross-sectional image of the patient and is usually formatted to $512 \times 512$ pixels[1] (other sizes are also possible).

The arrangement of the pixels depends on an anatomically oriented coordinate system. In case of DICOM images, the $x$ coordinate usually spans from the patient's right to the left side, the $y$ coordinate spans from anterior (patient's front) to posterior (patient's back) and the $z$ coordinate from inferior (patient's feet) to superior (patient's head). It is therefore called LPS (Left-Posterior-Superior) coordinate system.

## 2.3 Segmentation of Medical Image Data

Medical image data is a useful source of information for the surgeon since it provides an overview of the patient's individual anatomy prior to the intervention. The surgeon is able to check for abnormalities, plan surgical steps, and, in case the surgical intervention includes image guidance, identify landmarks and define their coordinates (see Section 2.4.3). Unfortunately, the nature of volumetric data requires doing this in two dimensional slice views of the data set and thus checking a large number of slices. This is not intuitive and requires a high level of training to securely identify specific structures and follow them from slice to slice. Especially in the area of the temporal bone where structures are highly complex in shape and spatial arrangement, this is a difficult task even for experienced surgeons [NDWL09].

Image segmentation is used in order to cope with these challenges. It can be described as outlining the shape of anatomical structures in each slice image. Every pixel which belongs to a certain structure is identified and its boundary to its surrounding area is delineated within the images. Using this information, three dimensional models can be calculated with the help of common image processing methods (e.g. the marching cube algorithm [LC87]). Thus a 3D model can be presented to the surgeon, which facilitates the understanding of the anatomical arrangement greatly (see Figure 2.3). Furthermore, 3D models also allow for a quantification of spatial relationships between structures as well as an automated planning of the intervention. In effect, the safety as well as the efficiency of the surgical planning process can be improved.

A lot of techniques have been developed that can be used to extract or segment structures from medical image data. Nevertheless, image segmentation is still a field of intensive research in biomedical image processing. The methodology of these techniques can be found in numerous publications and, therefore, is not discussed in detail within this section. Interested readers are referred to [Rog08]. In the following, a short overview of the different approaches to image segmentation is given.

In order to classify segmentation techniques, several categories can be found in the literature. Technically, they can be divided into two classes, i.e. low level segmentation and model based

---

[1]pixel = picture element
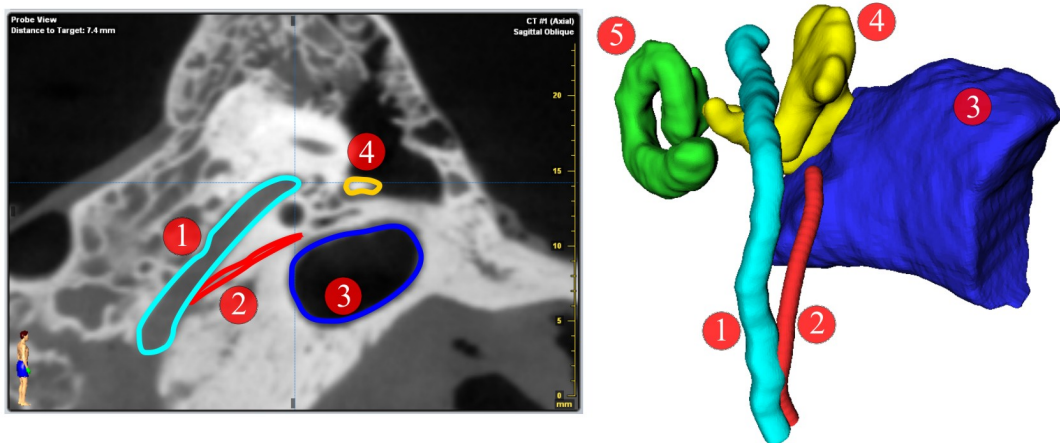
**Figure 2.3:** Segmentation of ear structures (left) and corresponding three dimensional visualization (right). Legend: facial nerve (1), chorda tympani nerve (2), auditory canal (3), ossicle (4), cochlea (5, not visible in slice view).

segmentation. From an operator's point of view, they can also be divided into the following groups:

- Manual segmentation

- Semi-automatic segmentation

- Automatic segmentation

*Manual segmentation* is the most accurate but also the most time consuming approach [HRR08]. Each structure is traced manually by a trained observer (e.g. a surgeon) usually with the help of mouse interaction within a software framework. This process can be expedited by using mathematical functions such as thresholding which identifies the contour of a structure based on a gradient in intensity values. Since this step has to be performed for each structure in each slice image, it makes segmentation very laborious. An example of manual segmentation software of this kind is iPlan® (Brainlab, Feldkirchen, Germany, see Figure 2.3 left) which was partly used in context of this thesis.

*Semi-automatic segmentation methods* require initial interaction of the operator followed by an automated determination of the segmented structure. The initial information may be the placement of a seed point which is used to look for a given structure in the neighborhood automatically. These algorithms can be applied to 3D data and reduce the amount of interaction by the user. A common example of this technique is seeded region growing. Adjacent voxels[2] are checked against a predefined homogeneity criterion. If a voxel meets the criterion, it will be included in the region. For further information, the interested reader is referred to [Han09].

---

[2]voxel = volumetric picture element

In contrast to this, *automatic segmentation algorithms* do not require manual input. Very common in this context is atlas-based segmentation. The image data is compared to a known reference model (atlas), which contains accepted segmentations of the desired structures. Once a transformation is calculated which maps the atlas to the given image data set, these segmentations can be employed to identify the location of the structures within the examined image data. The basic assumption of this technique is that images of different individuals are similar in topology. Consequently, the success of the segmentation depends on how much each structure varies from patient to patient. In order to improve atlas based segmentation, it is often combined with additional segmentation techniques. A promising approach for the identification of temporal bone anatomy was developed by NOBLE ET AL. [NDWL09]. It is an atlas based segmentation technique and was partly used in the context of this thesis to segment relevant structures such as facial nerve, chorda tympani nerve, external auditory canal, ossicles, and labyrinth. The most important advantage of automatic segmentation is the amount of time which can be saved, since manual segmentation is very costly in terms of labor, especially when using high resolution imaging. In case of the temporal bone, automatic segmentation could be accomplished for the mentioned structures in less than 10 min. In contrast to this, manual segmentation of the same structures takes more than 64 min [Hei10].

After segmentation, each object can be exported to a 3D representation, for instance the STL (Surface Tessellation Language) format. STL files consist of a set of triangles representing the surface geometry (see Figure 2.3 right). Thus, the amount of data which is necessary to represent an object can be reduced drastically. This particularly improves the handling of large image data sets with high resolution. Further mathematical operations can be performed on the resulting objects, including data reduction algorithms and surface smoothing [TZG96].

## 2.4 Surgical Navigation

Surgical navigation can be regarded as the core part of IGS (see Figure 2.4). It consists of three steps which have to be performed in order to link the preoperative planning data to the intraoperative situation and to assist the surgeon during the intervention:

1. Localizing the pose of instrument(s) and the patient (surgical tracking)

2. Registering patient to planning data set

3. Comparing the actual pose information with the surgical plan and deducing a type of action

In the following sections the essential parts of surgical navigation will be described. In Section 2.4.1 the basic mathematical notation for the description of the localization process is introduced. Section 2.4.2 gives an overview of localization technologies and Section 2.4.3 focuses on the registration of the image space to the intraoperative situation. Section 2.4.4 finally addresses, how this knowledge can be used to assist the surgeon during an intervention.
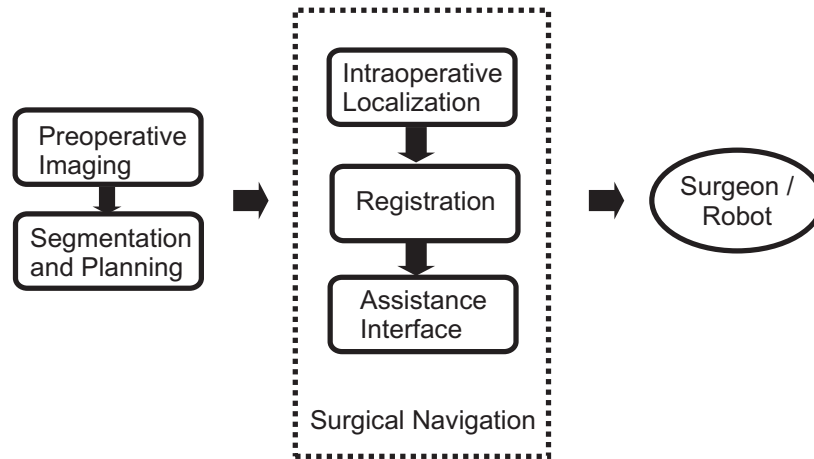
**Figure 2.4:** Surgical navigation as the central part of IGS

### 2.4.1 Mathematical Notation

The position of an arbitrary object $P$ in space is mathematically described in relation to a coordinate frame A, in the following denoted as $(CF)_A$. The distances $x_P$, $y_P$ and $z_P$ of $P$ along the Cartesian axes of $(CF)_A$ to its origin can be used to set up a homogeneous vector

$$_{(A)}\mathbf{x}_P = \begin{bmatrix} _{(A)}x_P & _{(A)}y_P & _{(A)}z_P & 1 \end{bmatrix}^T. \tag{2.1}$$

The use of homogeneous notation allows for applying affine transformations to a point in order to transform $_{(A)}\mathbf{x}_P$ to another coordinate frame. Thus, translation as well as rotation can be applied to $_{(A)}\mathbf{x}_P$ using a single matrix multiplication.

In tracking applications, the use of coordinate reference frames (CRF) is very common. These coordinate frames are defined by tracking markers which are detected by the localizer and refer to the target point $P$. If $P$ is given in a relation to $(CRF)_B$ by $_{(B)}\mathbf{x}_P$, it can be calculated in relation to $(CF)_A$ by

$$_{(A)}\mathbf{x}_P = {}^A\mathbf{T}_B \, _{(B)}\mathbf{x}_P, \tag{2.2}$$

where ${}^A\mathbf{T}_B \in \mathbb{R}^{4\times4}$ is a homogeneous transformation. It consists of a rotation matrix ${}^A\mathbf{R}_B \in SO(3, \mathbb{R})$ as well as a translation vector $\mathbf{t}_{A\rightarrow B} \in \mathbb{R}^{3\times1}$ and is defined as

$$^A\mathbf{T}_B = \begin{bmatrix} {}^A\mathbf{R}_B & \mathbf{t}_{A\rightarrow B} \\ 0 \; 0 \; 0 & 1 \end{bmatrix}. \tag{2.3}$$

See Figure 2.5 for an illustration of the spatial relationship.

If the orientation of the object is also of interest, it can be described by using a coordinate frame which is located at the point of interest with a given orientation. Thus, a homogeneous transformation matrix ${}^A\mathbf{T}_P$ can be used instead of a position vector in order to describe the object's
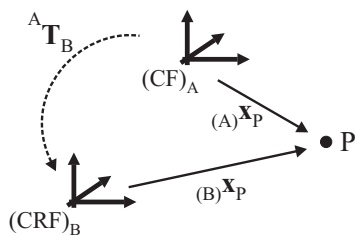
**Figure 2.5:** Illustration of a transformation matrix $^A\mathbf{T}_B$ to determine the position $_{(A)}\mathbf{x}_P$

pose in relation to $(CF)_A$. This allows for applying the same mathematical transformation as in Equation 2.2 in order to change its reference coordinate frame, so that it can be written as

$$^A\mathbf{T}_P =^A \mathbf{T}_B \ ^B\mathbf{T}_P. \tag{2.4}$$

This is depicted in Figure 2.6.
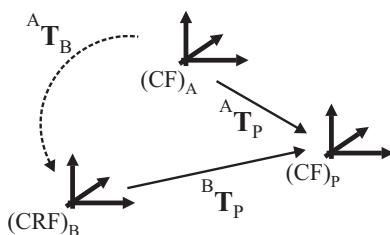


**Figure 2.6:** The use of a transformation matrix $^A\mathbf{T}_B$ to determine the pose $^A\mathbf{T}_P$

### 2.4.2 Principles of Localization Technologies

Localization systems are technical devices that allow for measuring and dynamically tracking the pose of an object in a given coordinate frame, which is defined in the localization system. Usually the system is able to detect special sensor devices, which are mounted to the target object. For medical applications, typically the patient as well as some instruments are tracked at the same time to determine their relative spatial arrangement. Therefore, different technical approaches exist while the most important ones for medical purposes are presented in the following.

- *Mechanical localization:* The instrument is rigidly linked to a serial structure consisting of various passive joints. The actual angle of each link is measured by joint encoders and the instrument's pose is determined by calculating the direct kinematics of the structure. Mechanical localizers are able to provide high accuracy (e.g. portable measurement arm FARO Gage, FARO EUROPE GmbH & Co. KG: 0.005 mm [FAR08]). Nevertheless, their cumbersome handling within the operation room and their inability to track more than one

device at the same time are the reasons why mechanical localizers are no longer used in most IGS applications.

- *Optical localization:* Each object is equipped with special markers that can be detected by two or more cameras. These are either active markers consisting of light emitting diodes (LEDs) or passive markers having a dedicated appearance or reflecting infrared light from an external light source. The position of each marker is calculated with the help of geometrical triangulation. The pose of a reference adapter can be calculated by using a known arrangement of three or more markers rigidly connected to it. It is important that the adapter is fixed to the target object and placed within the cameras' field of view in order to be detected. Optical localizers provide an accuracy in the range of 0.3 mm [NDIb]. Their key limitation is the necessity of a free line of sight between camera and adapter.

- *Electromagnetic localization:* Sensor coils are fixed to the target objects and controlled magnetic fields of low strength are generated by an external field generator. Due to the change of magnetic field intensity, voltages are induced in the sensor coils, which are used to determine the sensor's actual pose in relation to the field generator. In contrast to optical localization, no direct line of sight is necessary for the localization of the sensors, which allows for an in-body localization of instruments. Additionally, magnetic localization markers can be realized at a smaller size than light emitting markers. The accuracy of electromagnetic localizers is in the range of 0.48 mm [NDIa]. Nevertheless, the accuracy of tracking suffers if it is interfered with by magnetic fields from other devices or is influenced by metal objects.

In the past decade, optical tracking systems have evolved to be the solution with the highest accuracy, versatility, and reliability [BHWC08]. Because of the high requirements on the accuracy of the mCIS approach, this technique was chosen to be used in the experimental setup. Figure 2.7(left) shows a stereo optical tracking system (Polaris$^{\circledR}$, Northern Digital Inc., Waterloo, Ontario, Canada) using passive markers for localization. The system consists of two rigidly connected cameras surrounded by light emitting diodes and a processing unit. The diodes emit infrared (IR) light which is reflected by markers of a reference adapter and afterwards measured by the cameras. In order to determine the actual pose of the adapter, a minimum of three markers is needed. With a frequency of $20-60$ Hz the localizer sends a stream of Cartesian coordinates as well as a set of rotation angles or quaternions defining the target adapter's actual pose. They can easily be used to determine the pose $^{\text{loc}}\mathbf{T}_{\text{target}}$ of a target object. Figure 2.7 (right) shows a reference adapter with three reflective markers, which is mounted to the base of a robot.

One of the main advantages of optical localizers is the ability to track multiple reference adapters at the same time. This allows for calculating the position $_{(\text{pat})}\mathbf{x}_{\text{tip}}$ of the drill's tip in relation to the coordinate frame of a reference adapter $(CRF)_{\text{pat}}$, mounted to the patient by using

$$_{(\text{pat})}\mathbf{x}_{\text{tip}} = {}^{\text{loc}}\mathbf{T}_{\text{pat}}^{-1} \, {}^{\text{loc}}\mathbf{T}_{\text{tool}} \, _{(\text{tool})}\mathbf{x}_{\text{tip}}. \tag{2.5}$$

Figure 2.8 illustrates this relation.

**Figure 2.7:** Left: Polaris stereo optical localizer (Northern Digital Inc.). Right: Reference adapter with three reflective markers, mounted to the base of a robot.
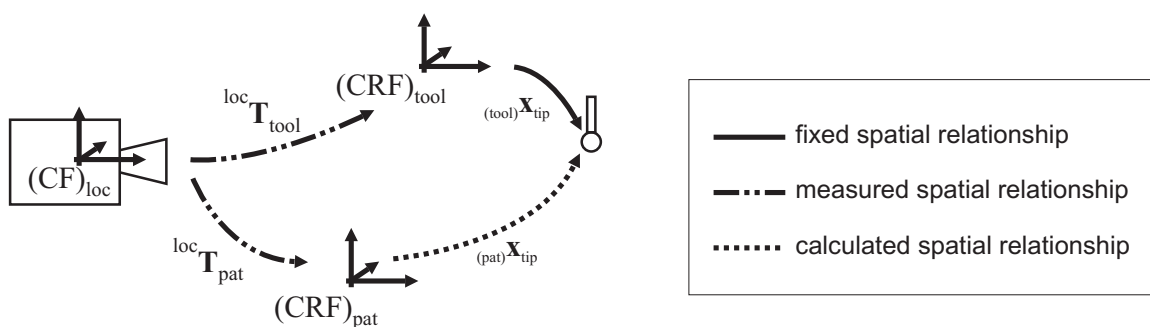


**Figure 2.8:** Transformations used to determine the location $_{(pat)}\mathbf{x}_{tip}$ of a drill's tip in relation to a patient's reference adapter

### 2.4.3 Registration

The coordinate frame of a reference adapter is usually defined in a fixed relation to the arrangement of reflective markers. The location of its CRF usually does not correspond with the coordinate frame of the image data, as the adapter is attached to the patient after image acquisition. In order to map the preoperative image data to the physical space, a registration step is necessary. The goal is to determine a transformation $^{pat}\mathbf{T}_{img}$ which can be used to locate the coordinate frame of the image data in relation to the patient, represented by its reference adapter. After this transformation is known, current positions of the instrument's tip $_{(loc)}\mathbf{x}_{tip}$ that are continuously measured by the localizer can be projected onto the image data set of the patient (cp. dotted arrow in Figure 2.9).

Generally, registration denotes the determination of a transformation that can be used in order to map one representation of an object onto another representation of the same object. In the case of surgical navigation, these representations are in particular preoperatively acquired images of the target object on the one hand and intraoperative measurements performed on the physical object itself on the other hand (image to physical registration). A perfect registration would lead to a transformation that maps any point from one representation to the corresponding point of the other representation. The registration can either be rigid or non-rigid. Whereas non-rigid registration

techniques are usually used to map one image data set to another (image to image registration), its application to register deformable physical objects is still a subject of research [Fit10]. Rigid registration techniques imply that the anatomy remains rigid during image acquisition and surgical intervention.

A variety of registration techniques can be found in the literature including point based methods, surface based methods and intensity based methods [FHM00]. For image to physical registration, point based as well as surface based methods are common. Point based methods are based on a number of fiducial points $\mathbf{p}$ that can be identified both in image space and in physical space. Since the localization of any fiducial is inherently affected with errors, no perfect registration can be found. Thus, the registration problem leads to an optimization of the transformation matrix $^{\text{phys}}\mathbf{T}_{\text{img}}$, which minimizes the weighted sum of the squares of Euclidean distances

$$^{\text{phys}}\mathbf{T}_{\text{img}} = argmin \left\{ \sum_{i=1}^{N} \omega_i^2 \left\| ^{\text{phys}}\mathbf{T}_{\text{img}\ (\text{img})}\mathbf{p}_i - _{(\text{phys})}\mathbf{p}_i \right\|_2^2 \right\}, \qquad (2.6)$$

that remain between corresponding points after the transformation has been applied. In this equation, $\omega_i$ denotes a weighting factor for the fiducial point $i$.

**Point Based Rigid Body Registration**

The existing approaches to the solution of the registration problem (i.e. Equation 2.6) can be classified into numerous categories [MV98]. In the field of surgical intervention at bony structures (e.g. the skull), point based rigid body registration states the standard approach that is used. The reason is that bony structures do not change their structure significantly under external forces. This allows for applying $^{\text{loc}}\mathbf{T}_{\text{img}}$ to any of the points in image space (e.g. the target coordinates of the intervention) in order to get its corresponding location in the measurement volume of the localizer. The derivation of the isotropic solution of point based rigid body registration as given in the following is according to [FHM00] but can also be found in numerous other publications. The transformation $^{\text{loc}}\mathbf{T}_{\text{img}}$ consists of a rotational matrix $^{\text{loc}}\mathbf{R}_{\text{img}} \in \text{SO}(3, \mathbb{R})$ as well as a translational vector $\mathbf{t}_{\text{img}\rightarrow\text{loc}} \in \mathbb{R}^{3\times1}$. This allows for splitting the registration problem into two separate tasks: finding $^{\text{loc}}\mathbf{R}_{\text{img}}$ and $\mathbf{t}_{\text{img}\rightarrow\text{loc}}$. For the registration, $N$ fiducial points $_{(\text{img})}\mathbf{p}_i$ ($i = 1..N$) are given in image space, as well as their corresponding points $_{(\text{loc})}\mathbf{p}_i$, measured by the localizer. Thus, the optimization criterion of Equation 2.6 can be rewritten using spatial coordinate vectors of $_{(\text{img})}\mathbf{p}_i$ and $_{(\text{loc})}\mathbf{p}_i$:

$$\Sigma^2 = \sum_{i=1}^{N} \omega_i^2 \left\| ^{\text{loc}}\mathbf{R}_{\text{img}\ (\text{img})}\mathbf{p}_i + \mathbf{t}_{\text{img}\rightarrow loc} - _{(\text{loc})}\mathbf{p}_i \right\|_2^2, \qquad (2.7)$$

Each fiducial point suffers from errors in the localization process, which means that $\Sigma^2$ is generally not zero. Nevertheless, from the assumption of an isotropic error distribution[3] it can be concluded

---

[3]The assumption of an isotropic error distribution is a standard approach in point based rigid body registration. Note

that both sets of fiducial points have the same centroid. This relationship allows for eliminating the translational part in Equation 2.7 by using the centroid of the weighted sum of the fiducial points

$$
\begin{aligned}
{}_{(\text{img})}\bar{\mathbf{p}} &= \frac{\sum\limits_{i=1}^{N} \omega_i^2 \,{}_{(\text{img})}\mathbf{p}_i}{\sum\limits_{i=1}^{N} \omega_i^2} \quad \text{and} \\[2em]
{}_{(\text{loc})}\bar{\mathbf{p}} &= \frac{\sum\limits_{i=1}^{N} \omega_i^2 \,{}_{(\text{loc})}\mathbf{p}_i}{\sum\limits_{i=1}^{N} \omega_i^2}
\end{aligned}
\tag{2.8}
$$

as well as the distance of each fiducial point to this centroid

$$
\begin{aligned}
{}_{(\text{img})}\tilde{\mathbf{p}}_i &= {}_{(\text{img})}\mathbf{p}_i - {}_{(\text{img})}\bar{\mathbf{p}}, \quad \text{and} \\
{}_{(\text{loc})}\tilde{\mathbf{p}}_i &= {}_{(\text{loc})}\mathbf{p}_i - {}_{(\text{loc})}\bar{\mathbf{p}}.
\end{aligned}
\tag{2.9}
$$

The assumption of corresponding centroids yields to the consequence that the registration algorithm maps these points without a remaining error. Hence, it can be concluded that the translation vector $\mathbf{t}_{\text{img} \to loc}$ in Equation 2.7 is equal to their spatial displacement:

$$
\mathbf{t}_{\text{img} \to \text{loc}} = {}_{(\text{loc})}\bar{\mathbf{p}} - {}^{\text{loc}}\mathbf{R}_{\text{img}} \,{}_{(\text{img})}\bar{\mathbf{p}}.
\tag{2.10}
$$

By using Equation 2.8 to Equation 2.10, the optimization problem of Equation 2.7 can be rewritten as

$$
\Sigma^2 = \sum_{i=1}^{N} \omega_i^2 \left\| {}^{\text{loc}}\mathbf{R}_{\text{img}} \,{}_{(\text{img})}\tilde{\mathbf{p}}_i - {}_{(\text{loc})}\tilde{\mathbf{p}}_i \right\|^2.
\tag{2.11}
$$

Hence, it is reduced to the problem of finding the rotation matrix ${}^{\text{loc}}\mathbf{R}_{\text{img}}$ that maps the fiducial point set of the image data to the fiducial point set of the localizer data, while no additional translation vector is needed.

This kind of optimization problem is historically known as the *orthogonal procrusted problem*. In 1966, an analytical solution for this problem was presented by PETER SCHÖNEMANN [Sch66]. It is based on a singular value decomposition (SVD) of the common covariance matrix $\mathbf{H}$, which is defined by

$$
\mathbf{H} = \sum_{i=1}^{N} \omega_i^2 \,{}_{(\text{img})}\tilde{\mathbf{p}}_i \,{}_{(\text{loc})}\tilde{\mathbf{p}}_i^T.
\tag{2.12}
$$

After applying the SVD

$$
\mathbf{H} = \mathbf{U}\mathbf{\Lambda}\mathbf{V}^T,
\tag{2.13}
$$

---

that iterative solutions for a registration with anisotropic weighting have been published recently [BF09].

$^{\text{loc}}\mathbf{R}_{\text{img}}$ can be estimated by

$$^{\text{loc}}\mathbf{R}_{\text{img}} = \mathbf{V}\, diag\,(1,1,det\,(\mathbf{VU}))\, \mathbf{U}^{T}. \tag{2.14}$$

Note that the *diag* (...) term in Equation 2.14 ensures that only proper rotation matrices are accepted as a solution. In addition, all fiducial points are usually weighted equally, so that $\omega_i = 1$. After the rotational matrix is known, the translation vector $\mathbf{t}_{\text{img}\to loc}$ can be calculated using Equation 2.10, while $^{\text{loc}}\mathbf{R}_{\text{img}}$ is applied to the fiducial points in image space. $^{\text{loc}}\mathbf{T}_{\text{img}}$ can be determined with the solutions of $^{\text{loc}}\mathbf{R}_{\text{img}}$ and $\mathbf{t}_{\text{img}\to\text{loc}}$. The transformation is depicted as a dashed line in Figure 2.9.

During the registration procedure, the positions of the fiducial points in localizer space $_{(\text{loc})}\mathbf{p}_i$ are determined using a pointing device. Additionally, the pose of the patient's reference adapter $^{\text{loc}}\mathbf{T}_{\text{pat}}$ is measured in the same space. It is used to determine the fixed spatial relationship

$$^{\text{pat}}\mathbf{T}_{\text{img}} = \left(^{\text{loc}}\mathbf{T}_{\text{pat}}\right)^{-1}\; {}^{\text{loc}}\mathbf{T}_{\text{img}} \tag{2.15}$$

between the patient's reference adapter and the image space. The position of an instrument's tip can be calculated in relation to the image data set by

$$_{(\text{img})}\mathbf{x}_{\text{tip}} = {}^{\text{pat}}\mathbf{T}_{\text{img}}^{-1}\; {}^{\text{loc}}\mathbf{T}_{\text{pat}}^{-1}\; {}^{\text{loc}}\mathbf{T}_{\text{tool}}\; {}_{(\text{tool})}\mathbf{x}_{\text{tip}}. \tag{2.16}$$

Note that $_{(\text{tool})}\mathbf{x}_{\text{tip}}$ denotes the position of the instrument's tip in relation to its coordinate reference frame $CRF_{\text{tool}}$. It is a fixed relation which is obtained during the calibration of the instrument. The determination of $_{(\text{img})}\mathbf{x}_{\text{tip}}$ thus depends on actual measurements of the coordinate reference frames $(CRF)_{\text{pat}}$ and $(CRF)_{\text{tool}}$ by the localizer, while the remaining matrices describe fixed relationships. This has the effect that the localizer or the patient can be moved during the localization process without the need of a new registration step. However, it has to be mentioned that additional dynamic errors decrease the accuracy of the localization process in this case. Figure 2.9 depicts the spatial relationships included in the tracking process.
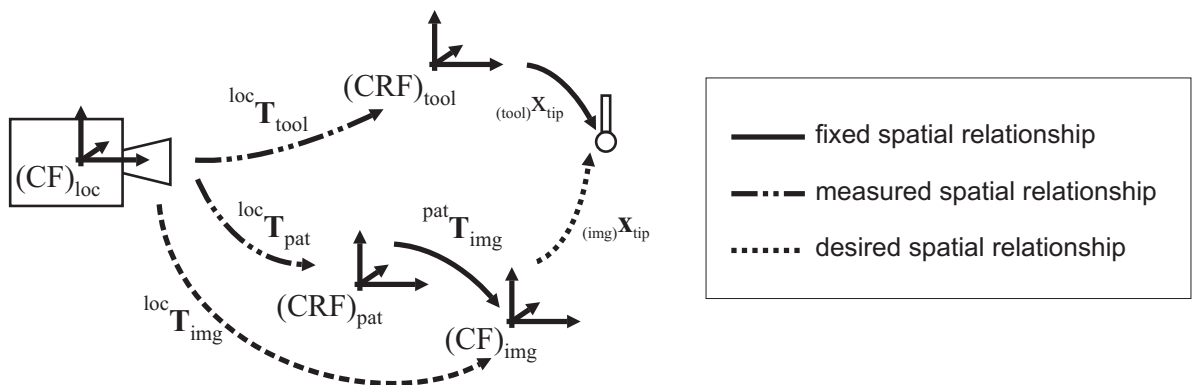


**Figure 2.9:** Overview of coordinate frames included in an image to patient registration

Further analytical solutions of the point based rigid registration problem can be found in the literature. They are based on using orthogonal matrices, unit quaternions, or dual quaternions. Nevertheless, a comparison of each of these solutions showed no substantial differences in the results of these algorithms [ELF97].

### 2.4.4 Types of Surgical Assistance

Surgical navigation also includes a type of action, which is deduced from the gathered pose information. The way how the navigation system assists the surgeon may vary due to the requirements of the intervention. The following three types of surgical assistance can be mentioned in this context.

1. The instrument's actual pose is visualized in reference to the patient's image data on a display. Beyond that, specific instructions on how to guide the instrument to reach the target can also be provided. This is the most common form of assistance, which is provided by commercial systems. The surgeon decides how to deal with this information.

2. The pose information can also be used to control a positioning system (e.g. a robot) in order to actively drive the instrument according to a predefined trajectory.

3. Single functionalities of an instrument are controlled by the navigation system. An example for this type of assistance is called Navigated Control®. The principle of Navigated Control is to adjust the power of an instrument depending on its actual location within the situs. Therefore, an area of operation is defined during the planning procedure which spares all vital important structures. If the surgical navigation system detects that the instrument leaves the working space, its power will be turned off. This provides an additional safety issue for the surgeon and eases the cognitive burden [SKR+05].

## 2.5 Medical Robotics

If IGS is performed manually, the greatest challenge for the surgeon is to establish the spatial correlation between the high resolution preoperative image data and the patient's actual pose in the operation room. This is necessary in order to transfer information from the images to the intraoperative situation and requires a lot of training. Any misinterpretation by the surgeon produces a displacement of the instrument from its desired pose and thus affects the accuracy of the intervention. Further human limitations exist which have an impact on the outcome of a surgical intervention. Among others, these include a natural tremor on the fine motion control of the surgeon's hand as well as errors resulting from fatigue and inattention of the surgeon.

That is why medical robotics became a field of intensive research in the past decades. Table 2.1 gives an overview of the strength and limitations of robots and humans. In contrast to humans, robots are untiring and have excellent geometrical precision. Complex geometrical instructions

can be implemented by the robot in precise physical actions. Thus, the interaction between instrument and patient can be enhanced greatly.

**Table 2.1:** Complementary strength of human surgeons and robots [TJ03]

|  | Strength | Limitations |
|---|---|---|
| **Humans** | Excellent judgement | Prone to fatigue and inattention |
|  | Excellent hand-eye coordination | Limited fine motion control due to tremor |
|  | Excellent dexterity (at natural human scale) | Limited manipulation ability and dexterity outside natural scale |
|  | Able to integrate and act on multiple information sources | Cannot see through tissue |
|  | Easily trained | Bulky end-effectors (hands) |
|  | Versatile and able to improvise | Limited geometrical accuracy |
|  |  | Hard to keep sterile |
|  |  | Affected by radiation, infection |
| **Robots** | Excellent geometric accuracy | Poor judgement |
|  | Untiring and stable | Hard to adapt to new situations |
|  | Immune to ionizing radiation | Limited dexterity |
|  | Can be designed to operate at many different scales of motion and payload | Limited hand-eye coordination |
|  | Able to integrate multiple sources of numerical and sensor data | Limited haptic sensing (today) |
|  |  | Limited ability to integrate and interpret complex information |

The common goal of research in medical robotics is to combine the complementary strength of robots and humans in order to improve medical interventions. In the field of surgical interventions at the lateral skull base, the use of robotic assistance allows for a reduction of the surgeon's tremor as well as a precise and reproducible drilling technique. Furthermore, the duration of interventions could possibly be reduced, leading to a better cost-benefit relation of the intervention. Last but not least, improvements in guiding surgical instruments by the use of robots allow for the development of new minimally invasive surgical approaches such as the mCIS which are not feasible by hand. More generally, the advantages of medical robots can be divided into three areas [TMFD08]:

- Improvement of the surgeon's technical capability by providing higher accuracy, dexterity, and the possibility to operate within radiological and infectious environments.

- Promotion of surgical safety by preventing surgical instruments from damaging delicate structures.

- Capturing and recording consistent and detailed information about the intervention that can be used in order to analyze the intervention and adapt future surgical plans.

Medical robots can be classified into various categories. They can be divided either by manipulator design (e.g. serial or parallel kinematics), by the targeted anatomy, or by the level of automation [SMDM07]. From an operator's point of view, the type of human-machine cooperation is of special interest, leading to the following three types of medical robots:

- Teleoperated systems

- Preprogrammed robots

- Robots with constrained cooperational control

A *teleoperated robot* mimics the surgeon's motions in real-time. The vision of telepresence surgery is to virtually insert the surgeon into the remote field of operation. The *daVinci® Surgical System* is an example of a teleoperated robot (see Figure 2.10, left). Instruments are connected to a robot and controlled by the surgeon from a console, consisting of a 3D image device and hand controllers for human machine interaction. It is probably the most successful medical robot on the market and mainly used for prostatectomies, cardiologic interventions and gynecologic surgical procedures using a minimally invasive approach. A teleoperated robot providing haptic force feedback is the *MIROSurge* robotic system developed by the Institute of Robotics and Mechatronics of the German Aerospace Center (see Figure 2.10, right) [KHN$^+$09].

In contrast to teleoperation, *preprogrammed robots* (also called surgical CAD/CAM systems in order to emphasize the analogy to industrial CAD/CAM systems) are characterized by a high degree of autonomy. Each surgical step that is defined during the preoperative planning phase is performed by the robot without any operator input during the intervention. An example is the *Robodoc®* system (Curexo Technology Corp., Freemont, CA) which was the first commercially available surgical robot. Initially developed by TAYLOR ET AL. [TPM$^+$90], the robot was used to establish implant pockets with high precision in knee and hip replacement procedures.

Systems with *constrained cooperational control* allow for an intuitive interaction with the user. An example of this kind of control is established in the *Kinemedic* robot (German Aerospace Center, Institute of Robotics and Mechatronics) [OWH$^+$06]. This principle, called Hands On Robotics, enables a manual guidance of a torque controlled robot by pushing or pulling it at any point of its structure. Deviations of the robot's actual pose from the surgical plan can be compensated by the robot, while the surgeon keeps full control of the robot.

The first medical intervention with robotic assistance was performed in 1985. A robot was working as a positioning device in order to orientate a needle for biopsy of the brain. Robots for the lateral skull base are not commercially available and can be found only as research objects at universities [CSW$^+$09].

The development of robotic devices for medical purposes continues to evolve. Besides research, other aspects are also important for the dissemination of medical robots. In particular these include training and credentialing, specification of clinical applications, risks of surgery and cost-benefit analysis [SAG07].

**Figure 2.10:** Examples of surgical robots: daVinci Surgical System, Intuitive Surgical (left); MIROSurge System, German Aerospace Center, Institute of Robotics and Mechatronics (right)

# 3 Error Analysis of a Robot Assisted mCIS Approach

Performing an mCIS is an example of a surgical intervention which is addicted to a high degree of technological assistance in accordance with an exceptional high demand of accuracy. Thus, the technology used in this approach plays a crucial role for the success of the intervention and needs to be examined carefully. However, the determination of the accuracy performance is ambiguous, since there are no commonly accepted rules for the assessment of a certain IGS application. In the context of a robot assisted mCIS, a number of questions arise which have to be answered. These include in particular:

- How accurate is the imaging technology?

- Can the intervention be planned correctly on the basis of the image data?

- How accurate is the tracking system?

- How accurate is the image to patient registration?

- How reliable is the calibration of instruments?

- How accurate can instruments be localized in relation to the patient?

- What is the overall accuracy of the system?

The goal of this chapter is to examine the workflow of a robot assisted mCIS. The impact of applied instruments and technologies on the accuracy performance of the intervention is assessed for each step of the proposed workflow. This approach requires a definition as well as a mathematical description of errors that can be observed. Effects of changes that are made to a particular component of the setup can be easily evaluated with a given analytical error model. Thus, suggestions can be made in order to improve the accuracy of the setup.

Section 3.1 introduces the most important types of errors, while Section 3.2 provides the terminology and a statistical description for these inaccuracies. In the subsequent sections, each part of the mCIS application is investigated and some improvements to the standard setup are suggested. Section 3.3 focuses on the imaging technology and discusses the role of different segmentation techniques as well as the complexity of defining coordinates of the mCIS. In the following sections, various types of inaccuracies that are embedded in the navigation process are examined. These include the concept of stereo optical localization which is evaluated in Section 3.4 as well as fiducial landmarks which are investigated in Section 3.5. Another sensitive procedure is the calibration of instruments as well as the use of robotic assistance for the guidance of an instrument. Investigations concerning this aspect are presented in Section 3.6 and Section 3.7, respectively.

The question about the system's overall accuracy can be answered based on a model based combination of each component's error contribution. Section 3.8 provides an appraisal of the application accuracy based on the experimentally evaluated inaccuracies. Section 3.9 finally concludes this chapter and summarizes some suggestions for the experimental setup. Note that an empirical evaluation of the system's overall accuracy is performed separately and described in Chapter 4.

## 3.1 Types of Errors

Basically, systematic as well as random errors can be observed in a robotic assisted IGS application. Systematic errors on the one hand are caused by imperfections of the measuring device or the test setup. Usually, these include varying conditions during the measurement process as well as inaccurate theoretical models that are used to calculate the actual pose of a target. Random errors on the other hand can be found in almost every part of the IGS setup. However, they cannot be predicted by the user due to their random nature. This section identifies different sources of inaccuracies that are included in the given experimental setup (cp. Figure 3.1). Note that their error values are examined in Sections 3.3 to 3.7.
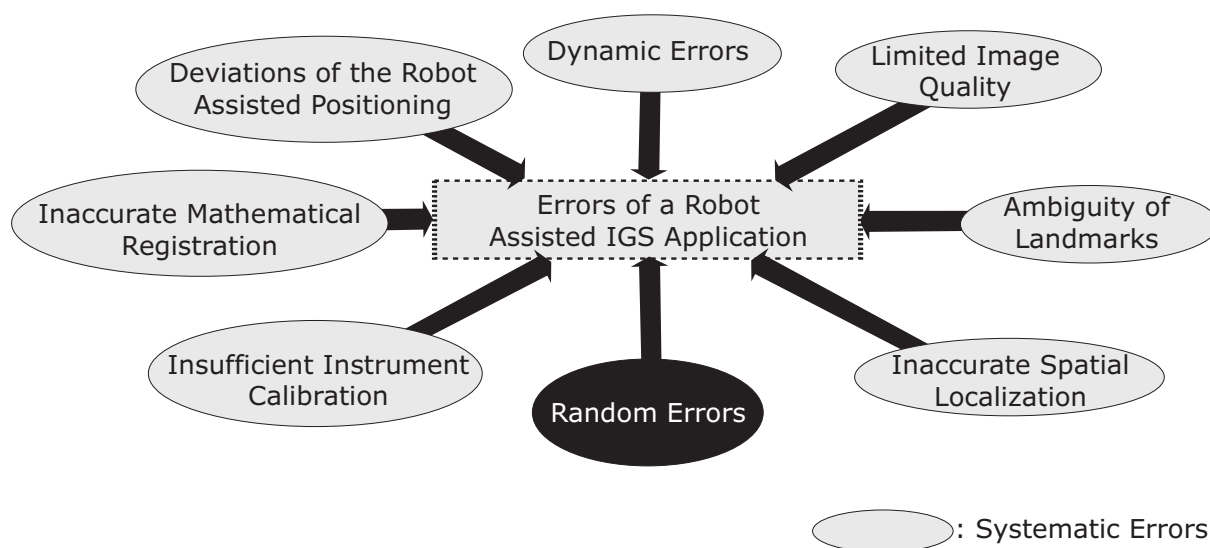


**Figure 3.1:** Errors of a robot assisted IGS application

**Inaccuracies caused by Limited Image Quality**

A limited resolution as well as image artefacts arising from metal objects yield a reduced quality of CT images. As a consequence, anatomical structures cannot be identified perfectly, which results in a defective localization of target coordinates and registration landmarks. This decreases the accuracy of the IGS intervention.

**Inaccuracies caused by Ambiguity and Fixation of Landmarks**

The quality of landmarks plays an important role for the registration performance. While having the advantage of being less invasive, anatomical landmarks usually cannot provide the same accuracy as artificial landmarks. These are, due to their well defined shape, more accurate but need to be attached to the patient. Shifting effects due to an improper fixation of artificial landmarks lead to large inaccuracies of the image registration and thus need to be avoided.

**Inaccuracies of Optical Localization**

The determination of a reflective marker's position in space as well as the arrangement of markers on a reference adapter are crucial for the performance of the optical localization process. The most important reasons for inaccuracies are listed in the following:

- Camera lenses inherently suffer from optical distortion. An imperfect compensation of the optical distortion yields to a deviation in the marker's pose estimation.

- An accurate calibration of the cameras' spatial arrangement to each other is crucial, since it directly affects the calculation of a marker's position in physical space.

- The tracking unit needs to reach its specified operating temperature before pose values are in the range of the localizer's specified accuracy. A temperature change of internal components affects the accuracy of the localization process and yields a drift of calculated marker positions.

- Reflective markers need to be of good quality (i.e. correct size and shape, clean and with good reflecting properties), since positions of dirty or partly covered markers are estimated with a deviation due to their different appearances in the images of the localizer unit. In addition to that, proper light conditions as well as a free line of sight between cameras and markers need to be established for an accurate localization.

- Each reflecting marker needs to be completely visible in both images of the localizer. Fiducials that are partly overlapping with another cannot be distinguished by the localizer.

- Some basic rules have to be considered for the arrangement of markers on a reference adapter. Among others, these include a unique arrangement and preferably large distances between single markers.

**Inaccuracies caused by Insufficient Calibration of Instruments**

The calibration of an instrument consists of the determination of the spatial relationship between the instrument's point of interest (e.g. the tip of a drill) and its reference adapter. Usually, optical tracking is used for this purpose. However, the calibration methodology has to be chosen with exceptional care, since any error that is made during this step remains constant throughout the subsequent process of navigation.

**Inaccuracies of the Mathematical Registration Methodology**

The standard registration algorithm that is used to map image data to physical space minimizes the fiducial registration error of measured landmarks (see Equation 2.6). The methodology assumes a certain error distribution of the localization process. As mentioned before, this does not necessarily coincide with the true nature of the collected measurement data. Therefore the result of the registration is not perfectly accurate which is the reason for further inaccuracies of the navigation process.

**Inaccuracies caused by Limited Spatial Control of the Robot's End Effector**

Every robot is equipped with internal sensors that have a limited resolution. Furthermore, the robot's true structure differs from the kinematic model which is used by its embedded controller to drive the robotic structure to a specified pose. This yields to a deviation between the end effector's actual and its desired pose.

**Inaccuracies caused by Dynamic Errors**

Dynamic errors occur when the robot and/or the target are in motion. A moving object causes artefacts within the images of the localizer so that its location cannot be determined correctly. In addition to that, due to system latencies that are caused by data synchronization, signal transmission, as well as internal calculations of the control computer, measurement values are outdated when a control command has been calculated since the object has moved to another pose in the meantime.

**Random Errors**

Random errors can be found in almost every part of the IGS setup. However, they cannot be predicted by the user due to their random nature. Regarding an image guided and robot assisted intervention, numerous sources of random errors can be identified. Medical image data, for example, is usually affected by image noise that is caused by the components of the imaging unit. Another example is the intraoperative localization of markers within the two dimensional image planes of the tracking cameras, which is also superimposed by a measurement jitter. Furthermore, vibrations of the robotic structure yield to small displacements of the instrument from its intended location and thus states an example of random errors.

Random errors decrease the accuracy of the intervention but might be reduced by redesigning the hardware. However, most of them cannot be fully eliminated. This leads to the consequence that they need to be considered in the mathematical error model when evaluating the accuracy of a certain image guided process. A mathematical way to handle random errors consists of using statistical distribution functions in order to predict upper and lower error limits according to a given probability.

## 3.2 Terminology and Statistical Description of Errors in IGS

Most of the mentioned errors follow a statistical pattern, even if they are random and therefore unpredictable. Hence, a statistical analysis can be used in order to describe their behavior. The most important and widely accepted mathematical description of errors in IGS was introduced in 1993 by MAURER ET. AL. [MMF93]. The terms of *Fiducial Localization Error* (FLE), *Fiducial Registration Error* (FRE) and *Target Registration Error* (TRE) were introduced in order to distinguish between different types of errors. In the following years, a lot of research has been done to describe the statistical correlation of measurement errors and the accuracy of the observed target location [FHM00, FW01, Fit09]. The derivations are summarized in Subsections 3.2.1 to 3.2.3. Additionally, a new type of error called *Target Navigation Error* (TNE) is introduced in Section 3.2.4.

### 3.2.1 Fiducial Localization Error (FLE)

$_{(A)}\text{FLE}_i$ denotes the displacement between a measured position $_{(A)}\mathbf{x}_i$ of a fiducial point $i$ and its true location $_{(A)}\hat{\mathbf{x}}_i$ in the coordinate frame of a measurement system ($A$) by its Euclidean distance

$$_{(A)}\text{FLE}_i = \left\| _{(A)}\mathbf{x}_i - _{(A)}\hat{\mathbf{x}}_i \right\|_2. \tag{3.1}$$

Figure 3.2(a) depicts an illustration of the FLE for a number of four fiducial points. The value of $_{(A)}\text{FLE}_i$ is generally non-zero, since measurement errors result in an offset of the determined position. These errors are assumed to be normally distributed, zero-mean, and independent in each spatial direction. Although this assumption does not necessarily express the true behavior of the localization process, it is a commonly accepted way to describe the statistics of the occurring errors [Fit10]. As a consequence, the variance of the entire fiducial localization process can be used as a sufficient parameter to describe the statistical error behavior. The expected value of this error, denoted by $\left\langle _{(A)}\text{FLE}^2 \right\rangle$ is given for a set of $N$ fiducial points by

$$\left\langle _{(A)}\text{FLE}^2 \right\rangle = \frac{1}{N} \sum_{i=1}^{N} {}_{(A)}\text{FLE}_i^2. \tag{3.2}$$

In case of IGS applications which include a registration between the image space (*img*) and the localizer space (*loc*), a combined $\text{FLE}^2$ of both spaces can be calculated by adding the variances:

$$\left\langle _{(\text{img + loc})}\text{FLE}^2 \right\rangle = \left\langle _{(\text{img})}\text{FLE}^2 \right\rangle + \left\langle _{(\text{loc})}\text{FLE}^2 \right\rangle. \tag{3.3}$$

Besides FLE the denotation of *Marker Localization Error* (*MLE*) can also be found in the literature, in case the fiducial point is a reflective marker.
FLE or MLE are caused by imperfections of the measurement device. They are the root cause for most of the subsequent registration errors. Therefore the FLE can be regarded as the most important value to describe the accuracy of an image guided process. Nevertheless, a major dis-

advantage is that the true location of a fiducial is not known. This means that the FLE cannot be determined online by a tracking system [FHM00].

### 3.2.2 Fiducial Registration Error (FRE)

A set of fiducial points is usually used to register two representations $(A)$ and $(B)$ of the same object. Therefore each fiducial point $\mathbf{x}_i$ is identified within both views and a registration matrix $^{B}\mathbf{T}_A$ is calculated, mapping any point from view $(A)$ to view $(B)$. Due to the presence of FLE, a perfect alignment of the fiducial points is usually not possible. As a measure to describe the resulting misalignment, $\text{FRE}_i$ denotes the displacement between the coordinates of a fiducial point $_{(B)}\mathbf{x}_i$ and its corresponding point $_{(A)}\mathbf{x}_i$ after the registration transform has been applied (cp. Figure 3.2(b)). It is calculated by

$$\text{FRE}_i = \left\| _{(B)}\mathbf{x}_i - {}^{B}\mathbf{T}_A \, _{(A)}\mathbf{x}_i \right\|_2. \tag{3.4}$$

Figure 3.2(b) depicts an illustration of the FRE for a number of four fiducial points. In order to specify the overall FRE, usually the root mean square (RMS) value

$$_{(B)}\text{FRE} = \sqrt{\frac{1}{N} \sum_{i=1}^{N} {}_{(B)}\text{FRE}_i^2} \tag{3.5}$$

is used. The relationship between FLE and FRE can be approximated based on the assumption of an independent and isotropic probability distribution of the FLE. The expected value of $\langle \text{FRE}^2 \rangle$ is then approximated by

$$\langle \text{FRE}^2 \rangle \approx \left( 1 - \frac{2}{N} \right) \langle \text{FLE}^2 \rangle, \tag{3.6}$$

where $N$ is the number of fiducials, incorporated in the registration process [FHM00]. Since the FRE is independent from the actual configuration of fiducials, an estimation of the FLE may be obtained from a set of measurements which is taken from preferably differing directions and configurations. By performing registrations of each combination and measuring the resulting FRE, $\langle \text{FLE}^2 \rangle$ can be estimated by the weighted average

$$\langle \text{FLE}^2 \rangle \approx \left( \frac{1}{M} \right) \sum_{m=1}^{M} \frac{N_m}{N_m - 2} \text{FRE}^2(m). \tag{3.7}$$

Note, that $N_m$ and $\text{FRE}(m)$ denote the number of fiducials and the FRE of registration step $m$, while $M$ is the sum of performed registrations [FHM00].

### 3.2.3 Target Registration Error (TRE)

Whereas $\text{FRE}_i$ amounts the error at a certain fiducial point, TRE denotes the registration error at any point of interest within the registered volume. Usually this point would be the location of a target structure of the surgical intervention. It depends on the arrangement of the fiducials as well

(a) Fiducial localization error FLE

(b) Fiducial registration error FRE
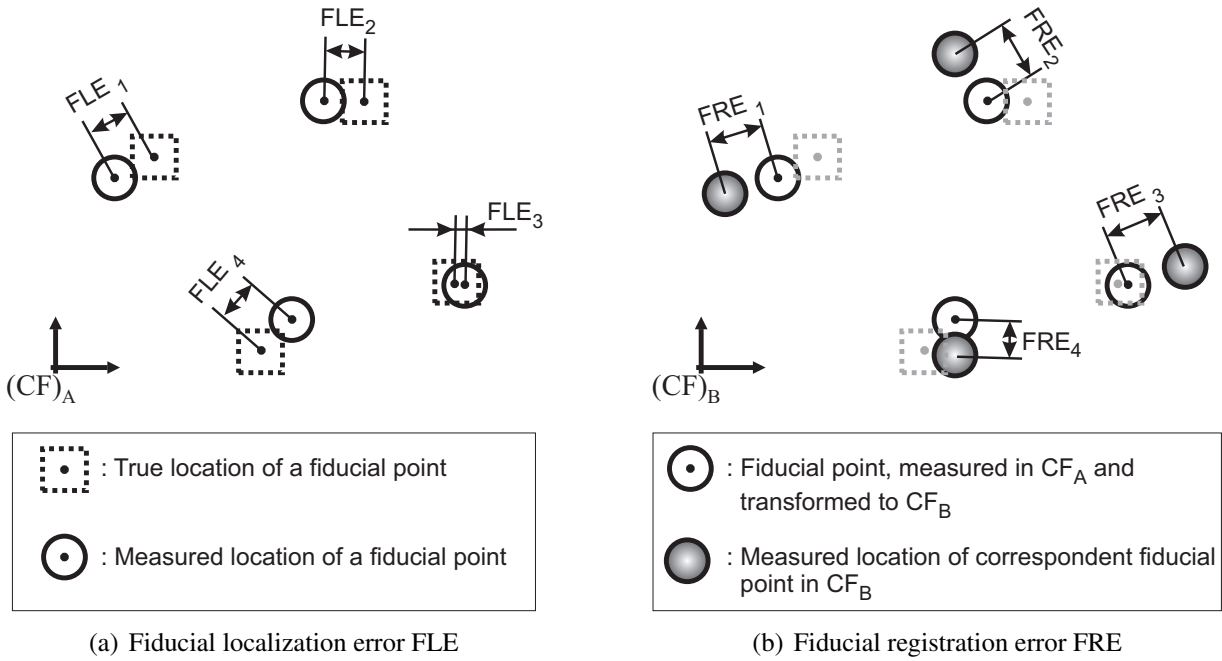
**Figure 3.2:** Illustration of the FLE and FRE, included in a registration process

as their location in relation to the target. A relationship between TRE and FLE is given based on the distances of fiducials and the target to the principal axes of the fiducial point set [FWM98]. It can be approximated by

$$\left\langle \text{TRE}^2 \right\rangle \approx \frac{1}{N} \left( 1 + \frac{1}{3} \sum_{k=1}^{3} \frac{d_k^2}{f_k^2} \right) \left\langle \text{FLE}^2 \right\rangle, \tag{3.8}$$

where $d_k$ is the distance between the target $\mathbf{x}_{\text{target}}$ to the principal axis $k$ of the fiducial set and $f_k$ is the RMS distance of all fiducials to that axis.

In order to give an indication of the TRE, tracking systems often provide the FRE. However, it is important to know, that the FRE, which is measured in a given case, does not correlate to the TRE of that specific case [Fit09]. In fact, the application accuracy is often worse than the value of the FRE. For example, an equal offset in the measurement of fiducial points (e.g. caused by a badly calibrated pointer) misleadingly results in a registration with a small FRE, whereas the real TRE may be large.

### 3.2.4 Target Navigation Error (TNE)

Three main errors can be pointed out that are included in the process of navigation during an IGS application:

1. The physical location of the target point $\mathbf{x}_{\text{target}}$ as defined in the preoperative image data

set of the patient is determined by the navigation system with the help of fiducial point registration. The process of localization is inaccurate and can be expressed by a $TRE_{target}$.

2. In order to provide information for the surgeon about the actual location of the instrument in relation to the target, the navigation system has to identify the location of the instrument's tool center point (tcp). This is done by measuring a set of reflecting markers which are attached to the instrument. The physical location of the tcp can be calculated by using a calibration matrix. However, this matrix is usually determined by registering the set of reflective markers to a model based description of the instrument. The error, which is embedded in the localization of the tcp step, therefore, can be expressed as a $TRE_{tcp}$ using the given error statistics of the target registration error.

3. The spatial manipulation ability of surgeons is limited (e.g. by a natural tremor), which is why instruments are never oriented exactly to the instructions of the navigation system. Even if a robot is used for positioning, a small displacement $\Delta$ occurs between the position of the instrument's tip and the coordinates given by the navigation system.

To describe the accuracy of the navigation process in an IGS application, different terms can be found in the literature. The most common are TRE and *application accuracy*. However, the term TRE is misleadingly in this case, since a combination of at least two *TREs* can be observed when instrument guidance is included in the IGS application. The *application accuracy* on the other hand covers any type of error at any stage of the intervention. Therefore, it is not restricted to the navigation process and includes additional errors such as the correctness of the target point definition during the planning of the intervention.

In order to address the error, which is hidden in the process of navigation, the term *Target Navigation Error (TNE)* is suggested in this thesis. The TNE covers the mentioned errors of the $TRE_{target}$, $TRE_{tcp}$, as well as the manipulation error $\Delta$ for the positioning of an instrument. In accordance to the given error model of the TRE, it is assumed that these errors are equally distributed and independent from each other. Therefore, the TNE can be approximated by

$$\langle TNE^2 \rangle \approx \langle TRE_{target}^2 \rangle + \langle TRE_{tcp}^2 \rangle + \langle \Delta^2 \rangle. \tag{3.9}$$

With FLE, FRE, TRE and TNE, a mathematical framework is given that can be applied to evaluate components of the image guided and robot assisted mCIS approach.

## 3.3 Imaging and Segmentation

Segmentation of temporal bone structures in CT images is a challenging task, since some of these structures are characterized by extremely small sizes, large interpatient variations, as well as a low image contrast to the adjacent anatomy. Especially the facial nerve and the chorda tympani, which are small but important tubular structures with diameters of approximately $1.0 - 1.5$ mm and $0.3 - 0.5$ mm, respectively need to be treated with exceptional care. MSCT is the state of the

art in CT imaging, whereas new types of computed tomography such as VCT offer an increased resolution. The benefit of high resolution imaging as well as methods for the segmentation of anatomic structures are discussed in the following.

### 3.3.1 Benefit of High Resolution VCT Imaging

The spatial resolution capability of CT imaging is defined as the minimum distance between two objects which can be separated as two entities in the images. Thus, a common parameter which is used to compare different types of CT units is the number of line pairs per centimeter ($\frac{lp}{cm}$). The separation of an object from the adjacent anatomy is usually defined at a minimum contrast level of 10 % which can be taken from the modulated transfer function (MTF). Hence, the higher the number of $\frac{lp}{cm}$, the higher is the spatial resolution capability of the scanning unit. The use of VCT imaging offers a significant increase of the resolution capability. A typical value of actual VCT units is an isotropic resolution of approx. 25 $\frac{lp}{cm}$ which is equivalent to a resolution of 200 $\mu m$ feature size [RDF04]. In contrast to this, typical resolutions of 16 slice MSCT scanners are approximately 14 $\frac{lp}{cm}$ which correspond to a resolution of 360 $\mu m$.

Increasing the resolution means that smaller structures can be visualized by these images. The following example illustrates this effect. An artificial test object with a number of countersinks, drill holes and cross recesses was reconstructed from VCT as well as MSCT images using a threshold segmentation technique. Figure 3.3 depicts a part of the reconstructed 3D-surface. The figure shows that larger structures such as the drill hole and the countersink can be identified in both reconstructions. The cross recess, however, which was milled into the phantom with a depth of 0.2 mm could be reconstructed from VCT images, whereas it almost disappears in the reconstruction from MSCT images. Hence, increasing the resolution capability allows for a reconstruction of smaller structures and states a potential benefit of VCT imaging.
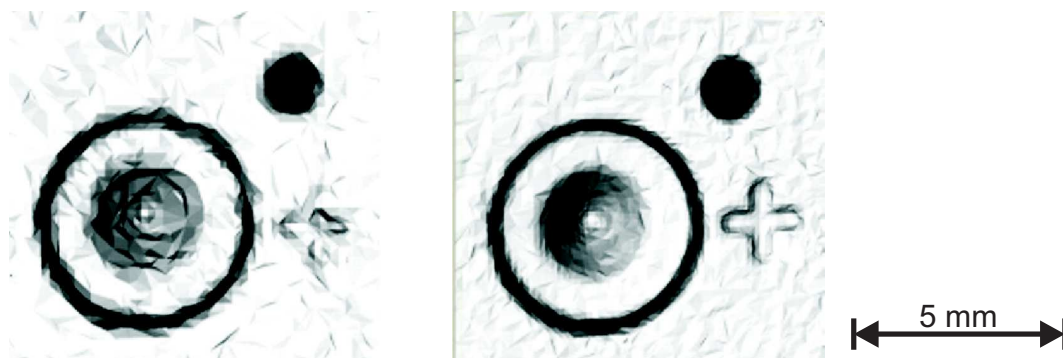


**Figure 3.3:** Reconstructed surface of an artificial accuracy phantom from MSCT (left) and VCT-images (right). The small cross almost disappears in the reconstruction from MSCT images.

Several publications exist, in which the improvements of VCT in comparison to MSCT are evaluated. BARTLING ET. AL. performed accuracy experiments in terms of measuring the target

registration error (TRE) on an artificial phantom. A significant higher TRE of 0.82 mm results when using MSCT compared to a TRE of 0.46 mm when using VCT [BLG$^+$07]. It is concluded that VCT might improve surgical accuracy especially in head and neck surgery. Nevertheless, the use of VCT imaging is not always regarded as beneficial for an intervention. MAJDANI ET. AL., for example, evaluated the quality of temporal bone imaging by rating the appearance of different anatomic structures within VCT and MSCT images [MTB$^+$09]. In contrast to the first publication, no differences between both modalities were found especially when full heads were scanned.

The reason for such diverging results in the literature can be explained by the different criterions that are used to assess the image modality. Having no explicit improvements in terms of image quality (such as contrast, noise, etc.) does not imply that the localization of a target structure is performed with the same accuracy in both image modalities. In fact, providing an increased resolution capability allows for a reconstruction of given structures with higher accuracy. This aspect is important especially with respect to the localization of landmarks. As a consequence, VCT imaging needs to be evaluated particularly with respect to the chosen types of landmarks. Section 3.5 will present more details as well as quantitative results for various combinations of landmarks and image modalities.

It can be stated that the quality of an image modality can only be evaluated with respect to the properties of the target structure and the intended medical application. Secondary effects such as an increased radiation exposure need to be considered in order to valuate the use of certain imaging technologies. In most cases, a trade-off between images of high quality on the one hand and limited radiation exposure of the patient on the other hand must be found.

### 3.3.2 Performance of Manual Segmentation Methods

Segmentation plays an important role in the workflow of an mCIS. Generally an accepted truth model of the given structure is necessary to quantify the quality of segmentation results. Two different types exist in this context. On the one hand, segmentation results can be validated by using artificial phantoms with a known size and surface structure. The use of such phantoms allows to analyze the image acquisition process but has the drawback that the properties of the target tissue cannot be reproduced. That is why evaluations of this kind are often not representative. On the other hand, segmentation results can be validated against manual segmentations performed by experts. Since single manual segmentations do not necessarily provide an accurate and true segmentation, a calculated mean out of multiple segmentations can also be used as an accepted truth.

Nevertheless, manual segmentation is still regarded to be the most accurate and reliable method to delineate temporal bone structures in CT images. However, the quality of manual segmentation results often suffers due to the voxel structure of the image data and the subsequent partial volume effects. Reconstructed surface models of segmented image data usually show a 3D polyhedra structure which appears facetted. Figure 3.4 illustrates this aspect in a simple 2D example. The true border of a structure, depicted as a dotted white line is approximated by the dashed black line separating each pixel to be part of the object or not. The segmentation result appears facetted due

to the given pixel structure of the image.
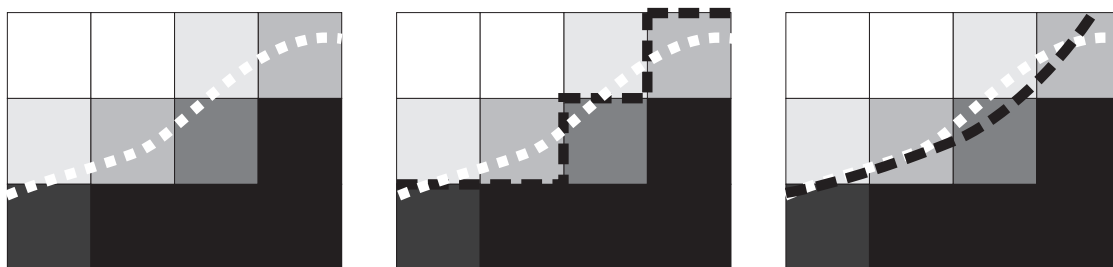


**Figure 3.4:** Example to illustrate the partial volume effect and a corresponding filtering. Left figure: Imaging of a structure with the original border marked as dotted white line. Central figure: Segmentation of the structure is marked as a dashed black line. Right figure: By using low pass filtering (indicated as a dashed black line) the original border of the structure can be approximated.

Although the true shape of anatomic structures such as the facial nerve or the chorda tympani nerve are not known, it can be assumed that their true surface is rather tubular than facetted. Hence, image processing methods such as low pass filtering can be applied to the segmentation results in order to smooth the facetted surface and thus approach the true geometry. However, a drawback of this filter in case of convex structures is a shrinkage effect and need to be avoided. In this case a low pass filter with a windowed sinc function interpolation kernel can be used so that the level of shrinkage is minimized during filtering [TZG96]. A 3D representation of a facial nerve and its filtered version is depicted in Figure 3.5. It can be seen, that the filtered structure appears less facetted and thus might approximate the true shape of the structure in a better way. Nevertheless, it needs to be verified, that the filtered surface does not significantly differ from the facetted original.

**Evaluation Metrics**

The filtered results of temporal bone structures can be evaluated by their grade of approximation to the original structure. A useful metric in this context is the mean absolute surface distance $\bar{D}_S(A,B)$, defined by

$$\bar{D}_S(A,B) = \frac{\sum_{a \in A} \min_{b \in B} d(a,b) + \sum_{b \in B} \min_{a \in A} d(b,a)}{|A| + |B|}. \qquad (3.10)$$

It denotes the mean distance $d$ between every point from segmentation $A$ to the nearest point of segmentation $B$ and vice versa [Han09].

In addition to that, it needs to be verified that the filtered surface does not significantly differ from the original at any point on the surface. This aspect is evaluated by calculating the Hausdorff
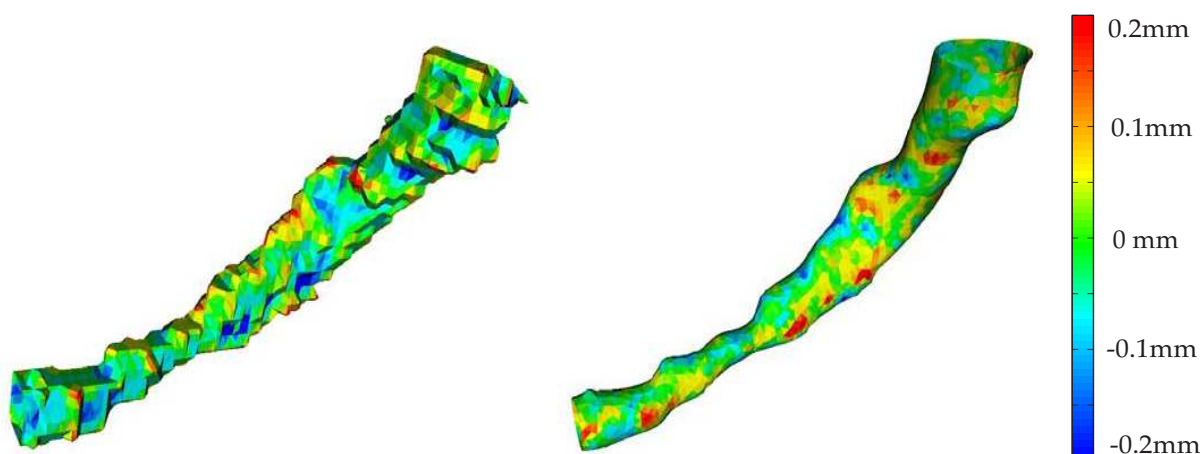
**Figure 3.5:** Manually segmented representation of the facial nerve (left) and filtered version (right). The surface distances are marked in terms of color. Red color means that the corresponding point lies 0.2 mm outside of the structure, whereas blue color denotes a corresponding point which is 0.2 mm inside the structure. An identical segmentation is marked by green color.

distance $H(A,B)$. It is defined by

$$H(A,B) = \max\{h(A,B), h(B,A)\} \quad \text{with}$$

$$h(A,B) = \max_{a \in A}\left\{\min_{b \in B} d(a,b)\right\} \tag{3.11}$$

and represents a worst case analysis of the segmentation [Han09]. Instead of calculating the mean of surface distances, its maximum is taken. Figure 3.6 depicts the calculation of the Hausdorff distance in a simple 2D example.
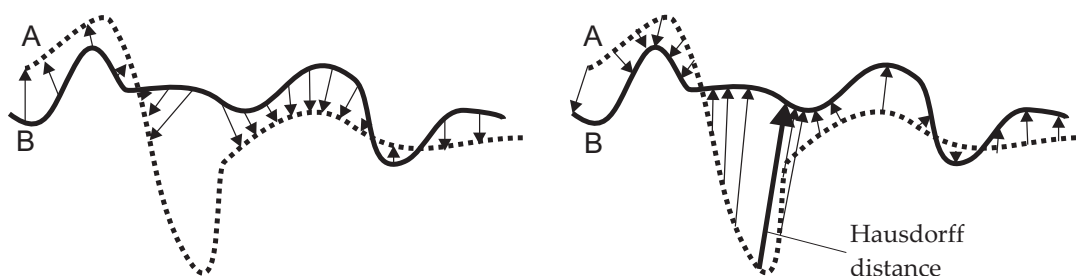


**Figure 3.6:** Differences between mean absolute surface distance and Hausdorff-distance. The mean absolute surface distance includes all absolute distances from surface $A$ to surface $B$ (left) and vice versa (right). It indicates the level of approximation of both structures. In contrast to this, the Hausdorff distance (marked in the right figure) is a worst case analysis of the segmentation.

**Results of Segmentation Evaluations**

15 temporal bones were scanned with a VCT unit. The isotropic resolution of the image data varied between 0.19 $mm^3$ and 0.25 $mm^3$ depending on the size of the temporal bone specimens. The facial nerve as well as the chorda tympani nerve were segmented manually. Smoothing was applied and, afterwards, the mean absolute surface distance was calculated. The results are summarized in Table 3.1. The mean absolute surface distance of all facial nerve segmentations varies between 0.078 mm and 0.103 mm with an average of 0.092 mm. In case of the chorda tympani nerve, the mean absolute surface distance varies between 0.045 mm and 0.060 mm with an average of 0.054 mm. Based on these results, it can be stated that only small changes were applied to each of the structures by the filtering.

In a next step, Hausdorff distances were also calculated for the given structures. As a criterion of acceptance, a maximum Hausdorff distance, which corresponds to the diagonal size of one voxel is defined. Smoothed surface structures will only be regarded as useful, if this criterion is fulfilled. The results can be taken from Table 3.1. The Hausdorff distance ranges from 0.223 mm to 0.359 mm for the facial nerve and from 0.103 mm to 0.163 mm for the chorda tympani nerve, respectively [Wei10]. For all 15 temporal bone specimens, the Hausdorff distance is lower than the maximum accepted value. As a result, smoothing of these structures is accepted for the given anatomical structures. Figure 3.5 exemplarily depicts the results for the facial nerve, where each surface triangle is colored according to the distances between the corresponding segmentation. Furthermore, Figure 3.7 depicts the original CT image, superimposed by a manual and a smoothed manual segmentation of the facial nerve.
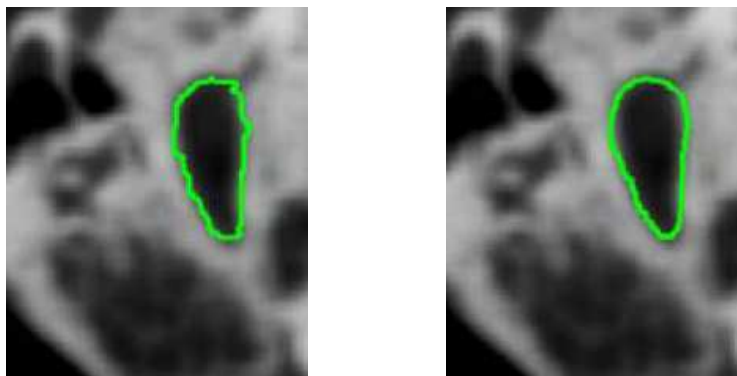


**Figure 3.7:** CT images superimposed by manual (left) and smoothed manual (right) segmentations of the facial nerve. The smoothed version of the segmentation was regarded as useful.

### 3.3.3 Performance of Auto Segmentation Methods

Automatic segmentation methods are of great interest, since manual segmentation is very time consuming especially when using high resolution imaging. Segmentation algorithms have been

**Table 3.1:** Mean absolute surface distance and Hausdorff distance of manual and filtered manual segmentation results

| Temporal bone | Anatomic Structure | Mean Absolute Distance [mm] | Hausdorff Distance [mm] | Maximum Accepted Hausdorff Value [mm] |
|---|---|---|---|---|
| TB1 | Facial Nerve | 0.078 | 0.223 | 0.332 |
|  | Chorda Tympani | 0.046 | 0.164 |  |
| TB2 | Facial Nerve | 0.089 | 0.301 | 0.371 |
|  | Chorda Tympani | 0.060 | 0.138 |  |
| TB3 | Facial Nerve | 0.080 | 0.227 | 0.354 |
|  | Chorda Tympani | 0.049 | 0.135 |  |
| TB4 | Facial Nerve | 0.094 | 0.277 | 0.386 |
|  | Chorda Tympani | 0.045 | 0.112 |  |
| TB5 | Facial Nerve | 0.096 | 0.277 | 0.433 |
|  | Chorda Tympani | 0.058 | 0.126 |  |
| TB6 | Facial Nerve | 0.099 | 0.324 | 0.433 |
|  | Chorda Tympani | 0.058 | 0.142 |  |
| TB7 | Facial Nerve | 0.087 | 0.235 | 0.368 |
|  | Chorda Tympani | 0.051 | 0.116 |  |
| TB8 | Facial Nerve | 0.087 | 0.282 | 0.381 |
|  | Chorda Tympani | 0.049 | 0.103 |  |
| TB9 | Facial Nerve | 0.097 | 0.251 | 0.433 |
|  | Chorda Tympani | 0.060 | 0.123 |  |
| TB10 | Facial Nerve | 0.088 | 0.245 | 0.384 |
|  | Chorda Tympani | 0.055 | 0.138 |  |
| TB11 | Facial Nerve | 0.104 | 0.359 | 0.433 |
|  | Chorda Tympani | 0.058 | 0.141 |  |
| TB12 | Facial Nerve | 0.095 | 0.258 | 0.433 |
|  | Chorda Tympani | 0.047 | 0.121 |  |
| TB13 | Facial Nerve | 0.095 | 0.290 | 0.409 |
|  | Chorda Tympani | 0.055 | 0.157 |  |
| TB14 | Facial Nerve | 0.098 | 0.293 | 0.433 |
|  | Chorda Tympani | 0.059 | 0.108 |  |
| TB15 | Facial Nerve | 0.095 | 0.270 | 0.433 |
|  | Chorda Tympani | 0.060 | 0.131 |  |
| Mean | Facial Nerve | 0.092 | 0.274 |  |
|  | Chorda Tympani | 0.054 | 0.127 |  |

recently presented by NOBLE ET. AL. which allow for the automated segmentation of temporal bone structures [NWLD08]. Basically, this approach uses an atlas based segmentation, combined with methods to extract tubular structures within the image data in order to find the facial nerve and the chorda tympani nerve. Studies concerning the accuracy of the segmentation show a mean deviation of less than 0.3 mm for the segmentation of the chorda tympani and the facial nerve [NDWL09]. This means that research in auto-segmentation methods have reached a level, which is sufficient to identify the anatomy of the temporal bone.

Structures of the temporal bone can be segmented in less than 10 minutes with these methods. In contrast to this, manual segmentation takes more than 64 minutes (including segmentations of cochlea, ossicles, chorda tympani nerve, facial nerve and auditory canal) [Hei10]. Although the speed of manual segmentation is highly dependent on the experience of the operator, automatic segmentation will always be much faster. However, since these methods are still in the development phase, results of automatic segmentation algorithms need to be verified by an experienced surgeon.

### 3.3.4 Path Planning

Planning of an mCIS insertion path to the cochlea is challenging, since numerous factors have to be considered by the surgeon. The following list includes the most important ones:

- The drill canal has to be placed in way that none of the adjacent anatomic structures is violated during the drilling process.

- Safety margins between the border of the drill canal and adjacent structures should be maximized to ensure their integrity. The size of the safety margin needs to be chosen with respect to a possible lateral deviation of the drill, which may be caused by navigation errors and drilling forces.

- The drill canal needs to approach the scala tympani of the cochlea from a preferably tangential direction. However, the scala tympani cannot be delineated from the scala media and the scala vestibuli in standard CT imaging. Instead, the round window membrane is usually used as a reference point for the location of the drill canal's entry point.

- The size of the drill canal needs to be large enough so that an insertion tool can be used, which processes the implant to the cochlea. A current approach to such an insertion tool uses a u-shaped-tube with a diameter of 2.3 mm [HRO$^+$09].

- Additional effects such as thermal influences of the drilling process need to be considered.

The common approach to the cochlea is the MPTA (cp. Section 1.2). The spatial arrangement of the cochlea and the adjacent nerves demands to establish the drill canal via the facial recess, otherwise the approach would not be tangential to the basal turn of the cochlea. A 3D representation of the drill canal in relation to the anatomically important structures, which illustrates this aspect is depicted in Figure 3.8.
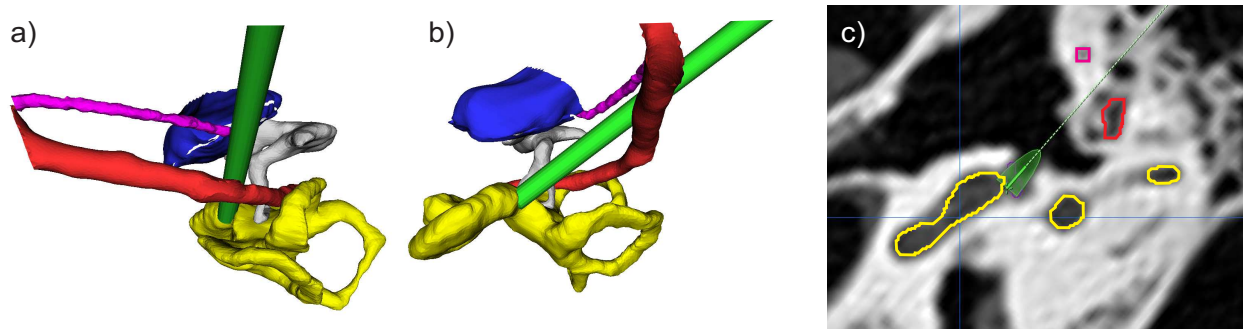
**Figure 3.8:** (a) and (b): View of the drill canal in a 3D representation of temporal bone structures. (c): View of the drill canal within an axial slice image. Colors: cochlea - yellow, ossicles - grey, ear canal - blue, facial nerve - red, chorda tympani nerve - magenta, drill canal - green.

Manual path planning includes that coordinates have to be defined in different slices of the image data followed by a check of the drill canal's position in every slice between entry and target point. This approach is very time consuming and prone to errors. In addition to that, path planning is further complicated by the fact that the drill canal needs to be placed within the facial recess, which has a size of approximately $2.5 - 3.5$ mm. This substantially limits the available space for sufficient safety margins to the facial nerve and chorda tympani nerve. This aspect has been investigated in [Hei10], where a series of 23 different temporal bone specimens were segmented and mCIS drill paths were manually defined in slice images of the temporal bone. Table 3.2 shows the resulting distances between the centerline of drill canal and the adjacent facial nerve and chorda tympani nerve, respectively. A drill radius of 1.1 mm and a safety margin of 0.8 mm was assumed, consequently a safety distance of at least 1.9 mm is required. This safety margin could not be realized for any of the temporal bone specimens. As a consequence the author suggests a radical reduction of the safety margin to 0.2 mm in order to realize the mCIS for at least 26 % of the temporal bone specimens. However, such a low safety margin would require an exceptional high accuracy of the navigation technology, especially if these structures need to be preserved with a high probability. It can be stated that this level of accuracy cannot be guaranteed by actual IGS components, since the inaccuracies of actual tracking system already exceed this limit. Consequently, the radius of the drill canal needs to be additionally reduced to less than 1 mm in order to enable an mCIS with actual tracking technology. Furthermore, an exact knowledge of the surgical accuracy is required in order to establish sufficient safety margins.

### Evaluation of Manually Defined mCIS Drill Paths

Regardless of the actual size of the drill canal as well as the accuracy of the navigation process, the goal of the planning procedure is to find a location for the drill canal, where safety margins are maximized for all of the surrounding structures. This aspect can be used in turn to evaluate the

**Table 3.2:** Distances from the centerline of manually planned mCIS paths to the facial nerve and the chorda tympani nerve (distances taken from [Hei10]). Note that results of an automatic path planning approach are presented in Chapter 5.

| Temporal bone | Distance $d_{fn}$ [mm] to facial nerve | Distance $d_{ct}$ [mm] to chorda tympani nerve | $\alpha[-] = \frac{d_{fn}}{d_{ct}}$ |
|:---:|:---|:---|:---|
| M20 | 1.50 | 1.30 | 1.15 |
| M21 | 1.50 | 1.60 | 0.94 |
| M22 | 1.50 | 1.70 | 0.88 |
| M23 | 0.90 | 0.80 | 1.13 |
| M24 | 1.20 | 1.30 | 0.92 |
| M25 | 1.50 | 1.20 | 1.25 |
| M26 | 1.30 | 0.90 | 1.44 |
| M27 | 1.10 | 1.50 | 0.73 |
| M28 | 1.40 | 1.30 | 1.08 |
| M29 | 1.00 | 1.00 | 1.0 |
| M30 | 1.10 | 1.30 | 0.85 |
| M31 | 0.80 | 0.90 | 0.89 |
| M32 | 1.10 | 1.00 | 1.1 |
| M40 | 1.50 | 1.30 | 1.15 |
| M41 | 1.30 | 1.10 | 1.18 |
| M42 | 1.20 | 1.40 | 0.86 |
| M43 | 1.10 | 1.30 | 0.85 |
| M44 | 1.30 | 1.40 | 0.93 |
| M45 | 1.30 | 1.30 | 1.0 |
| M46 | 1.00 | 1.10 | 0.91 |
| M47 | 0.90 | 1.10 | 0.82 |
| M48 | 0.60 | 0.80 | 0.75 |
| M49 | 1.40 | 1.30 | 1.08 |
| Mean $\pm$ Std. dev. | $1.20 \pm 0.25$ | $1.21 \pm 0.24$ | $0.99 \pm 0.17$ |

actual placement of an mCIS drill path. This is performed for the manually defined drill paths in the following.

As mentioned before, the facial recess marks the main spatial limitation of the drill canal's placement. The facial nerve and the chorda tympani nerve are located on both sides of the drill canal. This leads to the consequence, that an increase of the safety margin of one structure would lead to a decrease of the other's. Moreover, the chosen size of the safety margin for a given structure reflects its level of safety. Hence, structures with high priority are consequently protected with large safety margins. This relationship can also be used vice versa: safety margins which have been planned between the drill and the facial nerve, respectively the chorda tympani nerve embody a priority of these structures. One can conclude that this relation should be constant for a series of temporal bone specimens if priorities are given[1]. The results of manually defined paths from

---

[1]Note that chapter 5 will go into detail, concerning the actual choice of priorities for temporal bone structures.

Table 3.2 can therefore be investigated using the ratio

$$\alpha = \frac{d_{fn}}{d_{ct}} \tag{3.12}$$

of the distances $d_{fn}$ and $d_{ct}$ from the axis of the drill canal to the facial nerve (fn) and the chorda tympani nerve (ct), respectively. For the given 23 drill canals of Table 3.2, $\alpha$ varies between 0.73 and 1.44 having a mean value and standard deviation of $0.99 \pm 0.17$. For this planning process the facial nerve and the chorda tympani nerve have the same priority, which means a target value of $\hat{\alpha} = 1$. The standard deviation of $\alpha$ in the manually performed planning results indicates the inherent variability, resulting from the planning procedure. The difference of the safety margins are up to 0.4 mm (see M26 and M27 in Table 3.2), which means that these distances can be optimized up to a few tenth of a millimeter in order to ensure an optimal distribution of safety margins. An automatic planning algorithm, which addresses this aspect is able to provide considerable benefit and increases the patient's safety during an mCIS intervention (see Chapter 5).

**Insertion Angle**

Apart from optimizing safety margins, other difficulties arise from the manual planning process. For example, the insertion angle $\psi_I$, which denotes the deviation of the insertion direction from an optimal tangential access cannot be measured manually. However, the information about this angle is important for patient individual electrode insertion techniques as presented in [HRO+09]. An automated planning procedure in conjunction with a model of the cochlea might be able to provide an additional benefit for the surgical intervention. Chapter 5 provides more detailed information about this aspect.

## 3.4 Pose Estimation of Coordinate Reference Frames Using Optical Localizers

The central part of IGS is the spatial localization of surgical instruments in relation to the patient's actual pose. Optical localizers are the most commonly used solution in surgical navigation because of their accuracy, tracking dynamic, and versatility. The instrument's tool center point (tcp) is localized with the help of a reference adapter, which is rigidly fixed to the instrument. A set of retro reflective marker spheres mounted on the adapter defines a local coordinate reference frame (CRF) that can be detected by the localizer. However, the accuracy of the localization process can be influenced by various aspects. They are discussed in the following.

### 3.4.1 Marker Localization Accuracy

Assessing the accuracy of optical localizers is subject to much ambiguity. Since there is no standardized rule for the assessment of these systems, manufactures often choose an own protocol for the determination of the localization accuracy. As a consequence, protocols are designed to

emphasize the strength of a manufacturer's own system and to diminish their limitations [WTF04]. Thus, a comparison of different localizers is difficult. For the *NDIPolaris®* localizer, the method to determine an 3D RMS volumetric accuracy includes the Euclidean distance error of a single marker stepped through more than 1200 positions throughout the measurement volume at a temperature of 20 °C. For each position, the mean of 30 measurement samples is used to define the coordinates of that position [Lei96]. The accuracy of the camera, being the final RMS value including all positions was estimated by NDI to less than 0.35 mm.

### 3.4.2 Design Issues for the Construction of Reference Adapters

Most of the commercially available optical localizers are able to determine the pose of individually designed reference adapters. Optimal marker geometries can be defined for a given tracking purpose. For example, it can be shown that the highest accuracy can be achieved when all markers are spherically distributed around the point of interest. This states a solution which is generally not practicable. Nevertheless, a set of rules has to be considered for the design of reference adapters in order to ensure optimal tracking accuracy [Pol04]. The most important ones are listed in the following:

- *Unique geometry:* The marker distribution on the reference adapter needs to have a unique and asymmetric geometry. The localizer uses this geometry to identify each adapter and to distinguish between them.

- *Number of markers:* More markers generally yield to an increased localization accuracy.

- *Distribution of markers:* A widespread distribution of markers increases the rotational accuracy of a CRF.

- *Position of markers in relation to the target:* The highest accuracy can be achieved in the centroid of the marker arrangement. Placing the markers around the target is strongly recommendable since any rotational error will also affect the translational accuracy of a target location, if it is not placed in the centroid of the marker arrangement. If this cannot be realized (e.g. for surgical drills), markers need to be located at least close to the target.

- *Avoidance of merging markers:* The reference adapter needs to be constructed, so that no marker is partly occluded by another during typical usage. This would yield to a merging effect of two markers in the images of the cameras and decreases the localization accuracy of the marker's centroid.

- *Restricted acceptance of marker orientations:* Because of manufacturing reasons, reflective markers are not perfectly spherical. Hence, the position of its centroid will shift in the image space if it is viewed off-axis. This effect becomes larger with an increased off-axis angle. In order to optimize the accuracy, a maximum allowable angle can be defined for the reference adapter in order to accept only measurements, which are taken with a preferred marker orientation.

### 3.4.3 Anisotropic Error Distribution

The spatial behavior of errors in the localization process of a target is of special interest, since the actual determination of its pose is performed on the base of an underlying error model. In this context, errors can either be isotropic or anisotropic distributed. Isotropic error distribution means that the error is equally distributed in the $x$, $y$ and $z$ direction from a statistical point of view. This assumption is valid for most of the statistical models in order to predict the errors of image to image registration methods. However, it does not necessarily hold for optically tracked instruments. In fact, for stereo-optical localizers, errors in the view direction of the cameras (usually indicated as the $z$ axis) are significantly larger than the $x$ and $y$ axis. The reason for this effect can be found in the configuration of optical localizers. This is illustrated in Figure 3.9. A defective identification of the marker's centroid in the image planes of the cameras results in a deviation $\Delta\phi$ of the resulting direction vector used for the triangulation algorithm. Since the
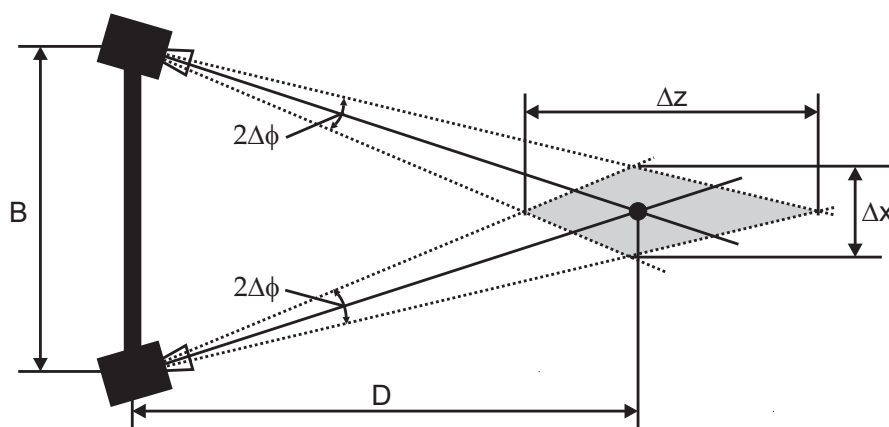


**Figure 3.9:** Illustration of the anisotropic error distribution of optical localizers

displacement $B$ of the two cameras is usually much smaller than the distance $D$ between the cameras and the measured marker, errors in $z$ direction are larger than in $x$ direction. With the given geometric proportions as indicated in Figure 3.9, the anisotropic factor $\gamma$ of the midpoint triangulation can be approximated by

$$\gamma = \frac{\Delta z}{\Delta x} \approx \frac{2D}{B}. \tag{3.13}$$

A typical value for the camera displacement of $B = 0.5m$ and a measurement distance of $D = 1.5m$ leads to an anisotropy factor of $\gamma = 6$. Advanced methods for the triangulation process are able to reduce the error in $z$ direction [RHS97], so that $\gamma$ is approximately $3 - 5$ for current tracking systems [WLFP08]. Furthermore, promising results were achieved by using advanced registration

algorithms such as an iterative Unscented Kalman filter [MA07, BF09]. However, these results are based on simulation data. Moreover, the anisotropic error distribution of a given localizer needs to be well known in order to improve the registration accuracy. As a consequence, these registration algorithms were not used in the context of this thesis.

### 3.4.4 Thermal Effects

Heating has an influence to the accuracy of the localization process. It is strongly recommended to wait until the localizer has reached its operating temperature before starting the tracking application. Otherwise, an offset can be observed in the position values of the targets which yields a bad tracking performance. The operating temperature is particularly affected by the illumination frequency $f_{IL}$ of the internal IR LEDs. Figure 3.10 illustrates the change of a target's determined position due to the frequency of the illumination. It can be seen that the drift in $z-$direction
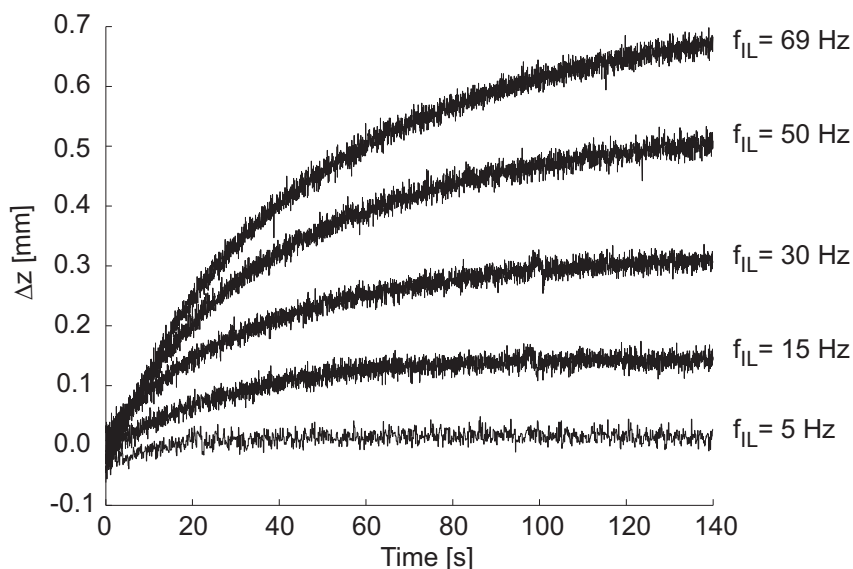


**Figure 3.10:** Change in $z$ position of a spatially fixed marker at different illumination frequencies ($f_{IL}$)

can be greater than 0.5 mm within the first 60 seconds of tracking for illumination frequencies of 69 Hz. After this time, a saturation takes place, indicating that the tracking unit has almost reached the operating temperature. Nevertheless, it can be stated that at least 120 seconds have to be passed before any measurement data can be used.

### 3.4.5 Gaussian Approximation

The localization of an object's pose is affected by a variety of errors that cannot be compensated. As an effect, pose data of targets is interfered by a measurement noise. Its statistical behavior can

be sufficiently approximated by a Gaussian distribution for each spatial direction. Figure 3.11 depicts the measurement noise in $z-$direction of a spatially fixed target as well as its approximation using a Gaussian function. Furthermore, this approach allows to apply statistical methods and to set up a model for the error propagation of the localization process.
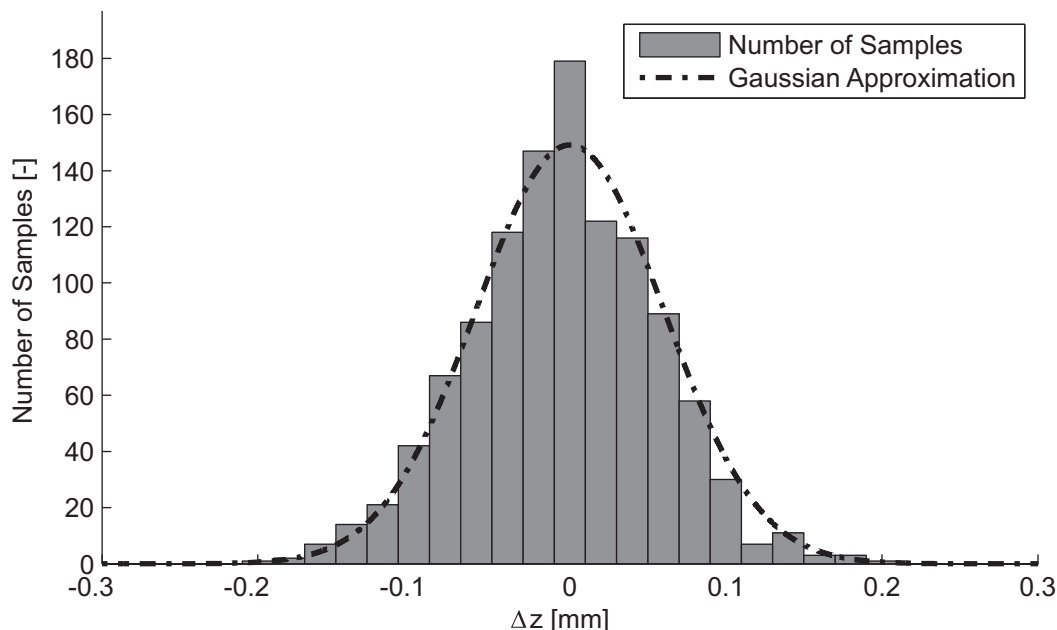


**Figure 3.11:** Measurement noise and Gaussian approximation of a spatially fixed marker in $z-$direction. The standard deviation is 0.06 mm.

## 3.5 Fiducial Landmarks

Fiducial landmarks (or fiducials) are artificial objects that are fixed to the patient in order to provide a well defined point that can be identified in CT image space as well as in the measurement volume of the localizer (fiducial point). They are used to register the image data to the intraoperative situation to enable image guidance. Fiducials play an important role in the registration process, since a localization error directly influences the accuracy of the image guided intervention. As mentioned before, bone implanted artificial landmarks provide higher accuracy compared to anatomic landmarks. They are discussed in the following.

### 3.5.1 Types of Bone Implanted Fiducial Landmarks

Bone implanted fiducials require an invasive surgical procedure consisting of a small skin incision followed by a anchoring hole which has to be drilled into the patient's skull. This procedure is avoided for routinely performed IGS, since requirements on the accuracy of these interventions

are not very high. Therefore, bone implanted fiducials are not state of the art of actual IGS applications. Instead, the use of skin fixed fiducials or stereotactic frames are much more common. Nevertheless, bone implanted fiducials need to be investigated in the context of an mCIS, since they are accepted to provide a significant higher localization accuracy [Fit10].

For research IGS applications at the lateral skull base, the use of mini-osteosynthesis screws with a diameter of 1.5 mm can be found in the literature (e.g. [HML02]). The cross-head screws provide a structure which can be identified easily in the image data and localized in physical space with a sharp pointer.

The definition of the fiducial point in image space, however, is subject to individual error if it has to be done manually. For example, changing the contrast of the CT image yields a different appearance of the screw due to blurring effects [MRB$^+$09]. Since the surgeon defines the fiducial point at the borderline of the screw as viewed in the CT image, this has an impact on the accuracy performance of the registration. Figure 3.12 depicts this effect.
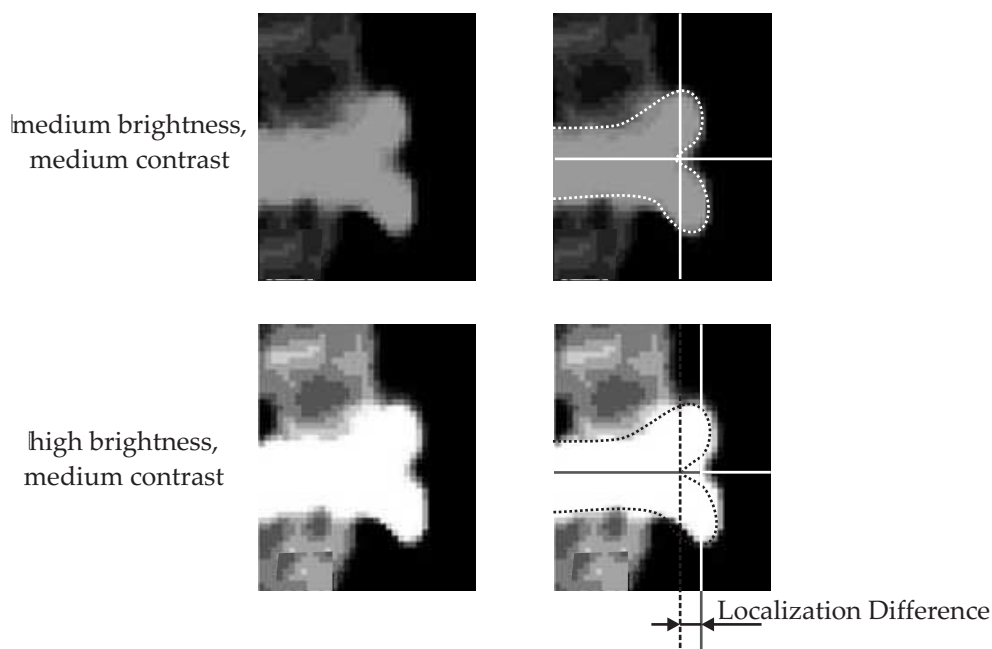


**Figure 3.12:** The manual definition of fiducial coordinates of mini-osteosynthesis screws in image space is affected by the actual adjustment of brightness, contrast and threshold.

Other types of landmarks, such as the markers used for the *ACUSTAR I Advanced Neurosurgical Navigation System*, use a cylindrical shape whereas the fiducial point is defined as the center of the cylinder [MFW$^+$97]. The use of marker with known structures such as cylinders or spheres is a common approach to define a single point in space with high accuracy. For the target application of an mCIS, bone implanted fiducial markers were designed in order to increase the registration accuracy (sphere fiducials, see Figure 3.13). They consist of an anchor containing a bone cutting thread with a diameter of 2 mm on the one side and a thread with a diameter of 1.6 mm on the other side. While the first thread is used to ensure a stable fixation of the anchor within the skull, a

sphere with a diameter 5 mm is attached to the second thread. The anchor as well as the sphere are made of titanium in order to reduce artefacts during CT imaging. The fiducial point is defined as the centroid of the sphere. Due to the spherical shape of the marker, changes applied to the contrast and threshold of CT images do not significantly affect the localization of the sphere's centroid. A further advantage is the simple, but well defined shape of the marker. This allows to compute its centroid with the help of an automatic detection algorithm. Errors resulting from the variability of manual fiducial point definition are avoided and the registration accuracy is increased. A tip has been designed according to the sphere that can be used with a pointing device in order to measure the fiducial point of a sphere with an optically localized instrument (see Figure 3.14). The pointer tip contains a circular cavity of 4.8 mm diameter, which allows the user to apply the tip to the sphere from almost any direction, while it seats ring-shaped and solidly on the surface. The pointer measures the center of the sphere due to the fact that its calibration is also performed on a 5 mm sphere using a pivoting method (see Section 3.6.1).

(a) Fiducial marker.                    (b) CT image of the
                                             fiducial marker.
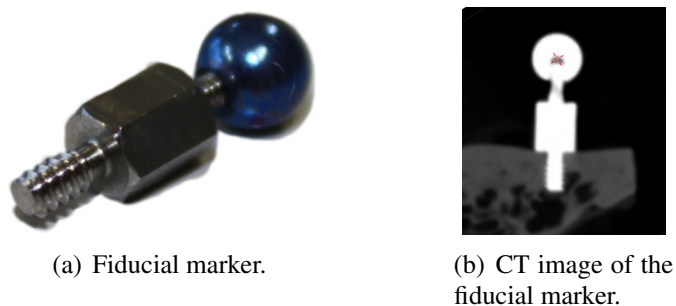
**Figure 3.13:** Fiducial marker for the registration process. The marker consists of an anchor with bone cutting thread of 2 mm and a thread of 1.6 mm used to attach a 5 mm-sphere. Anchor as well as sphere are made of titanium in order to reduce artefacts in CT imaging.

### 3.5.2 FLE in Image Space

Generally, a fiducial point has to be localized in the image space as well as in the physical space. The error of the localization process in the image space is denoted $_{(img)}$FLE. It cannot be measured directly because of the fact that the true location of a fiducial point is not known. Nevertheless, an approximation of $_{(img)}$FLE can be obtained by registering fiducial points of the same object from a number of $M$ different CT scans (cp. Equation 3.7). The object has to be scanned in preferably different orientations and positions in order to reduce the effect of spatially differing characteristics of the image modality. This has the consequence that the subsequent FLE-calculation is independent from the spatial distribution of the fiducials. The groups of fiducial points which are determined in the image data sets have to be registered in pairs and the registration error $_{(img)}$FRE$(m)$ $(m = 1, ..., M)$ has to be calculated for each registration $m$. Finally, $_{(img)}$FLE can be estimated.
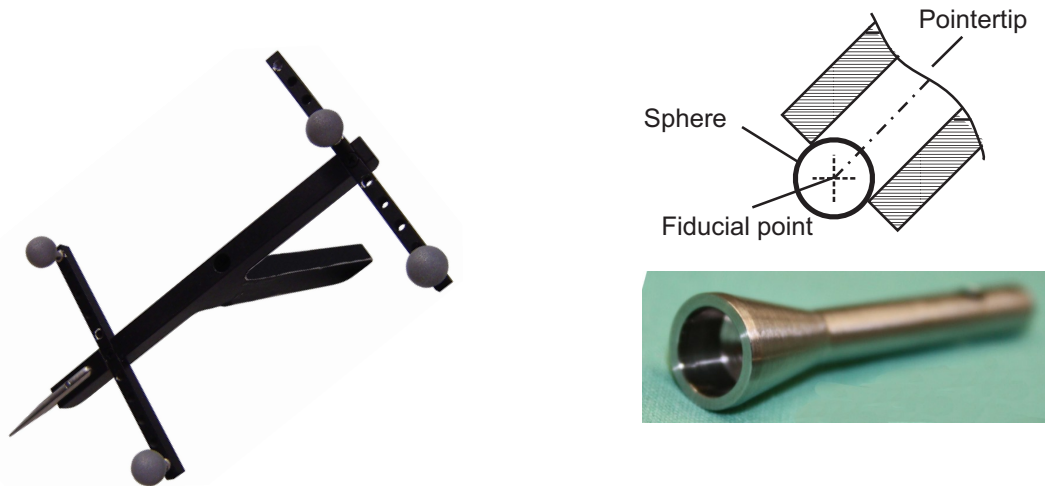
**Figure 3.14:** Pointing device for the localization of screws (left) and adapted pointer tip containing a circular space for the localization of spherical fiducials (right)

Two acrylic phantoms were constructed for the FLE determination of fiducial markers as introduced in Section 3.5.1. The first was equipped with M1.4 screw fiducials while the second phantom was equipped with sphere fiducials. The fiducials were arranged in different orientations in order to avoid parallel alignment of the anchors (see Figure 3.15).
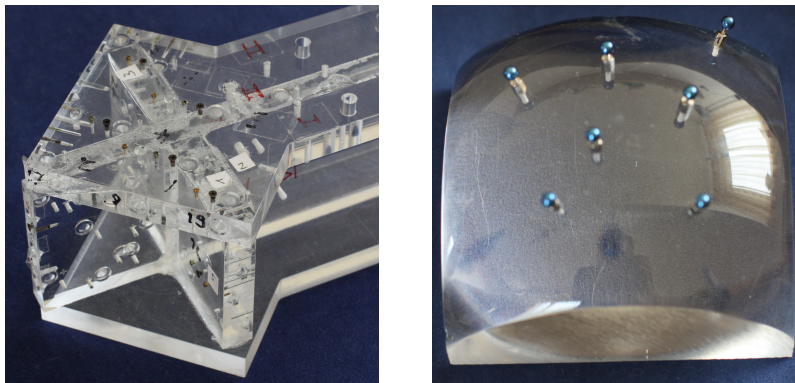


**Figure 3.15:** Left: Measurement phantom with different types of screw fiducials. Right: Measurement phantom with sphere fiducials

### $\left\langle _{(MSCT)}FLE_{Sc}\right\rangle$ of Screws in MSCT Image Data - Manual Determination

In a first step, the expected localization error $\left\langle _{(MSCT)}FLE_{Sc}\right\rangle$ of M1.4 screws was determined in MSCT image data. Therefore, the screw phantom was scanned in six different poses with the resolution of the MSCT data being 0.3125 mm $\times$ 0.3125 mm $\times$ 0.625 mm. Five fiducial

points were manually defined in each data set and afterwards registered to each other. A sum of 15 registrations was performed and the overall $\langle_{(MSCT)}FLE_{Sc}\rangle$ was calculated to 0.268 mm. The results of the $_{(MSCT)}FRE_i$ as well as the $\langle_{(MSCT)}FLE_{Sc}\rangle$ are depicted in Figure 3.16(a).
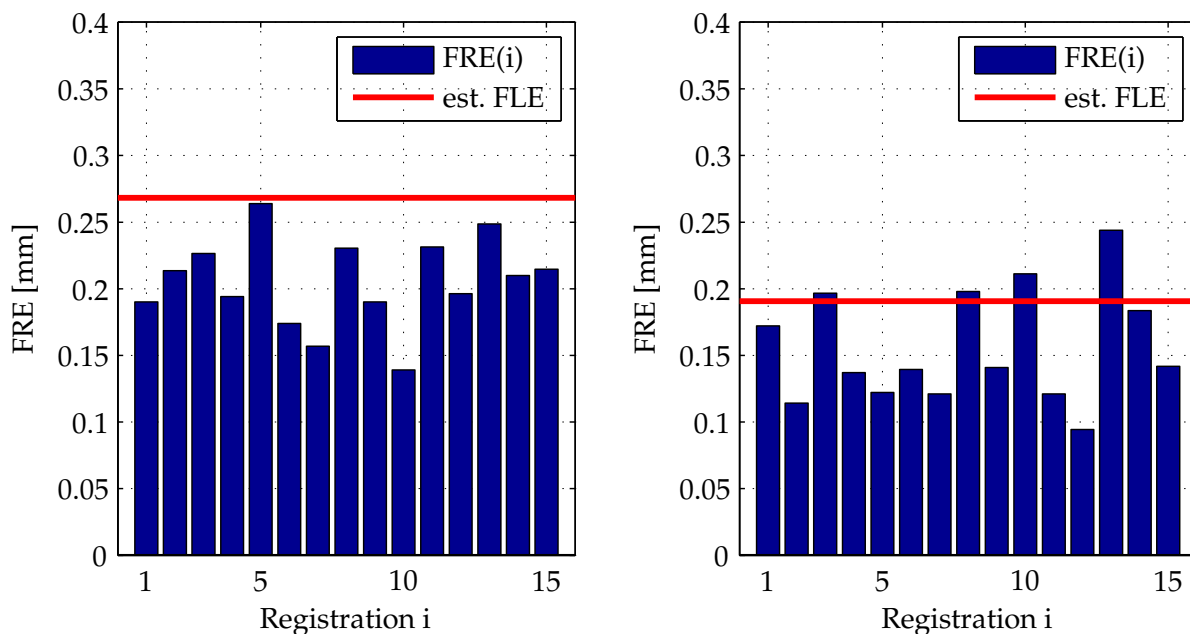


(a) Fiducial registration errors of screw fiducials. The resulting $\langle_{(MSCT)}FLE_{Sc}\rangle$ is 0.268 mm.

(b) Fiducial registration errors of sphere fiducials. The resulting $\langle_{(MSCT)}FLE_{Sp}\rangle$ is 0.191 mm.

**Figure 3.16:** FLE of different types of bone implanted markers. The fiducial coordinates were manually determined.

### $\langle_{(MSCT)}FLE_{Sp}\rangle$ of Sphere Fiducials in MSCT Image Space - Manual Determination

The accuracy of sphere fiducials was investigated, using the same methodology. The phantom containing seven sphere fiducials was scanned in the MSCT unit in six different poses and the fiducial coordinates were manually defined in the resulting image data sets. Afterwards, a sum of 15 registrations were performed for the FLE−determination. The overall $\langle_{(MSCT)}FLE_{Sp}\rangle$ was calculated to 0.191 mm which is 0.077 mm lower compared to the FLE of screw fiducials. The results of the $_{(MSCT)}FRE_i$ as well as $\langle_{(MSCT)}FLE_{Sp}\rangle$ are depicted in Figure 3.16(b).

### $\langle_{(Img)}FLE_{Sp}\rangle$ of Sphere Fiducials in Image Space - Automatic Determination

As mentioned before, an automatic determination of fiducial points might increase the registration accuracy. In order to verify this assumption, fiducial points were automatically calculated with the help of a detection software for spherical anchors (*VU Planner 1.06*, see Figure 3.17), which was kindly provided by the Vanderbilt University of Nashville for this project. The software utilizes a

model of the sphere which is mapped to the CT image data in order to get the fiducial coordinates with sub-pixel accuracy.
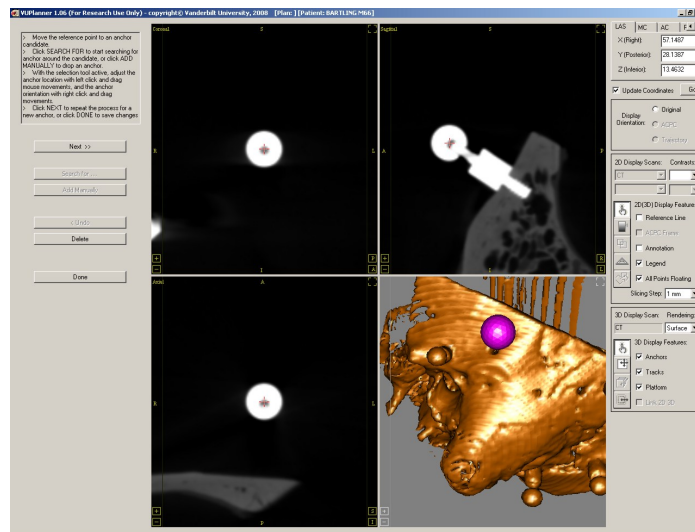


**Figure 3.17:** Software based localization of a 5 mm sphere fiducial in CT images of a temporal bone specimen (*VU Planner 1.06*, University of Nashville TN)

The sphere phantom was scanned in six different poses using a MSCT as well as VCT in order to determine the $\langle_{(Img)}FLE_{Sp}\rangle$ of sphere fiducials in the according image data. The location of each fiducial point was automatically calculated. The results of the FLE-estimation are depicted in Figure 3.18(a) and show that improvements to the fiducial localization accuracy were achieved . The $\langle_{(MSCT)}FLE_{Sp}\rangle$ was estimated to 0.166 mm in MSCT images. This is more than 0.1 mm lower compared to the localization error of screws and 0.025 mm lower compared to a manual determination of sphere fiducials.

The phantom was also scanned using a VCT unit. The isotropic resolution of the resulting image data varied between $0.18^3$ mm$^3$ and $0.25^3$ mm$^3$, based on the reconstruction protocol and the orientation of the phantom within the scanner. The results of the FLE-determination, depicted in Figure 3.18(b), show that the accuracy of the fiducial point localization is more accurate in case of VCT image data. The $\langle_{(VCT)}FLE_{Sp}\rangle$ was estimated to 0.150 mm which is another 10 % reduction of the error compared to MSCT imaging (see Figure 3.18(a)). Nevertheless, it can be stated that the difference of 0.016 mm between VCT and MSCT images does not imply a significant improvement in terms of absolute values.

### 3.5.3 FLE in Physical Space

The acrylic phantoms, which were used for the estimation of the FLE in image space, can also be used to obtain an approximation of the $\langle_{(loc)}FLE\rangle$ which appears in the measurement volume of a spatial localizer (*loc*). In this case, the localization of the fiducial points is performed with
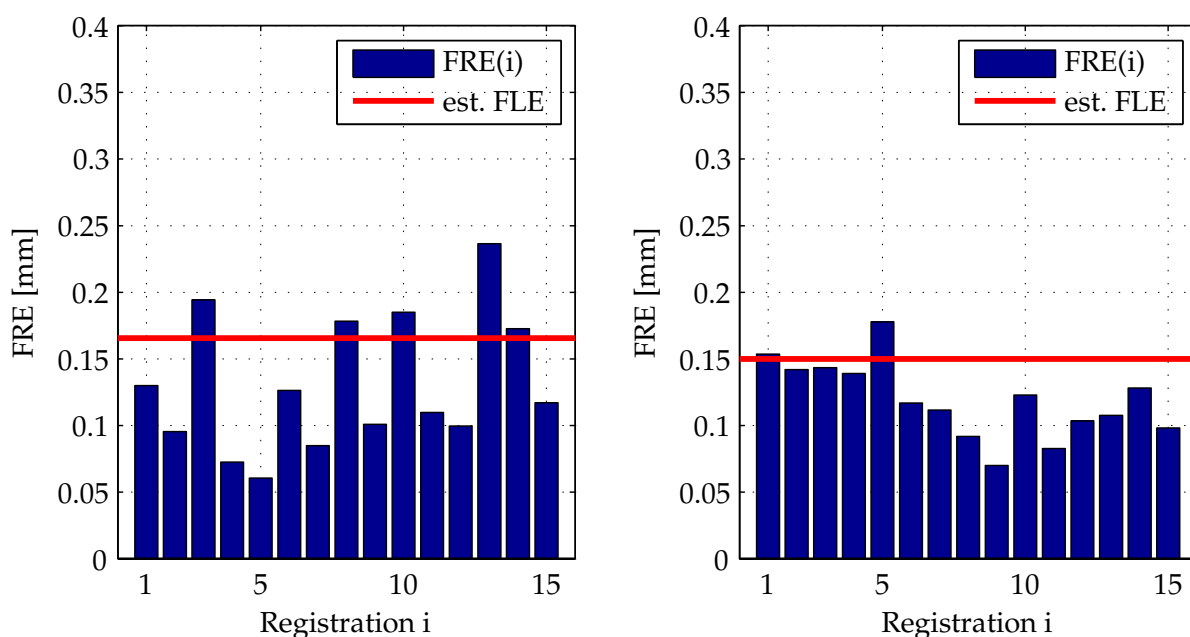
(a) Sphere fiducials in MSCT images. The resulting $\langle_{(\text{MSCT})}\text{FLE}_{\text{Sp}}\rangle$ is 0.166 mm

(b) Sphere fiducials in VCT images. The resulting $\langle_{(\text{VCT})}\text{FLE}_{Sp}\rangle$ is 0.150 mm

**Figure 3.18:** FLE of 5 mm spherical anchors in MSCT and VCT image space. The fiducial coordinates were determined automatically.

a pointer, so that the resulting FLE is assumed to include measurement errors of the localizer as well as errors related to the design and calibration of the pointer. The pointing device was used in combination with different tips in order to be applied to the different shapes of the fiducials (cp. Figure 3.14).

In addition to measuring with an optical localizer, the sphere fiducials were also localized using a portable measurement arm (FARO Gage, FARO Europe GmbH & Co. KG). Since the measurement arm has a calibrated inaccuracy, which is lower than optical tracking systems and given by the manufacturer (see Equation 3.14), it can be used to verify the validity of the FLE determination methodology. The results are presented in the following.

### $\langle_{(\text{loc})}\text{FLE}_{\text{Sc}}\rangle$ of Screw-Fiducials

Figure 3.19 depicts the results of a set of $N = 7$ screws, localized in $M = 9$ different orientations in relation to the optical localizer (*Polaris*[®], Northern Digital Inc.). 36 different registrations were performed. The results were applied to Equation 3.7 leading to an estimated $\langle_{(\text{loc})}\text{FLE}_{\text{Sc}}\rangle$ of 0.319 mm.
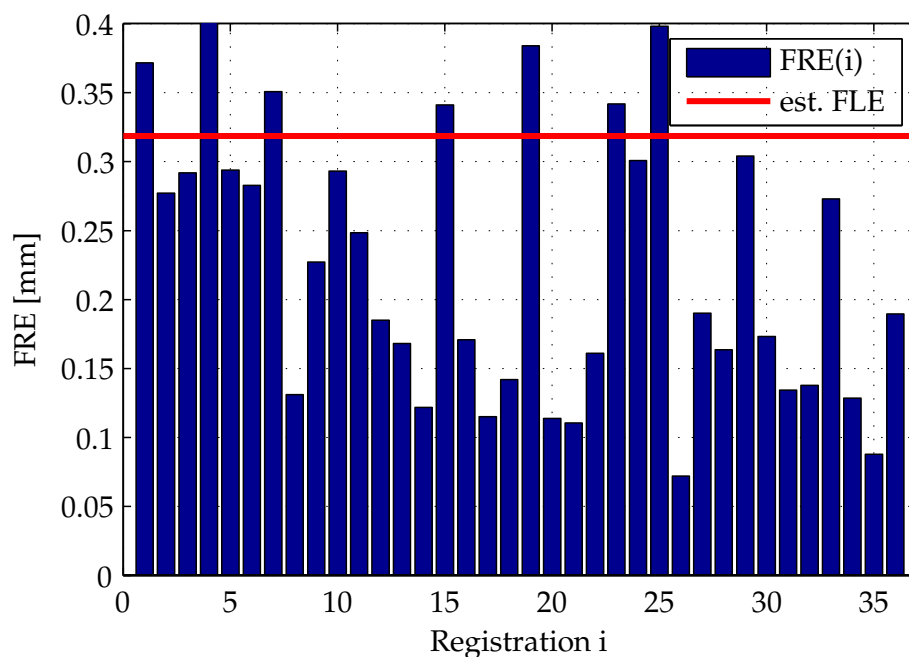
**Figure 3.19:** Fiducial registration error of screws, measured with a pointing device. The resulting $\left\langle _{(loc)}FLE_{Sc} \right\rangle$ is 0.319 mm

## $\left\langle _{(loc)}FLE_{Sp} \right\rangle$ of Sphere-Fiducials

The spheres-fiducials of the sphere phantom were measured in $M = 10$ different orientations. Two optical localizers (*Polaris*®, Northern Digital Inc. and *ARTrack2*, ART GmbH) were available for localization, whereas the same pointer could be used for both systems. As shown in Figure 3.20, no large differences between the FLE of the two localizers could be determined. Based on 15 performed registrations, the FLEs were estimated to 0.227 mm and 0.205 mm for the use of the ART localizer and the NDI localizer, respectively.

## $\left\langle _{(Faro)}FLE_{Sp} \right\rangle$ of Sphere Fiducials Using a FARO Gage Portable Measurement Arm

The fiducial points of the sphere fiducial phantom were measured by a portable measurement arm (FARO Gage, FARO EUROPE GmbH & Co. KG) at six different poses within the measurement volume. The resulting FREs are shown in Figure 3.21(b). $\left\langle _{(Faro)}FLE_{Sp} \right\rangle$ was estimated to 0.013 mm. These results can be compared with the measurement uncertainty $E$ of the Faro Gage measurement arm, which is given by

$$E[\mu m] = 10 + \frac{16L}{1000}, \tag{3.14}$$

where $L$ is the distance between the object and the measurement arm [FAR08]. For the given experiments, $L \approx 300$ mm yields to an uncertainty of $E = 14.8$ $\mu$m $\equiv 0.0148$ mm. Hence, the esti-

(a) Determination of the FLE in ART images. The resulting $\left\langle _{(ART)}FLE_{Sp}\right\rangle$ is 0.227 mm

(b) Determination of the FLE in NDI images. The resulting $\left\langle _{(NDI)}FLE_{Sp}\right\rangle$ is 0.205 mm
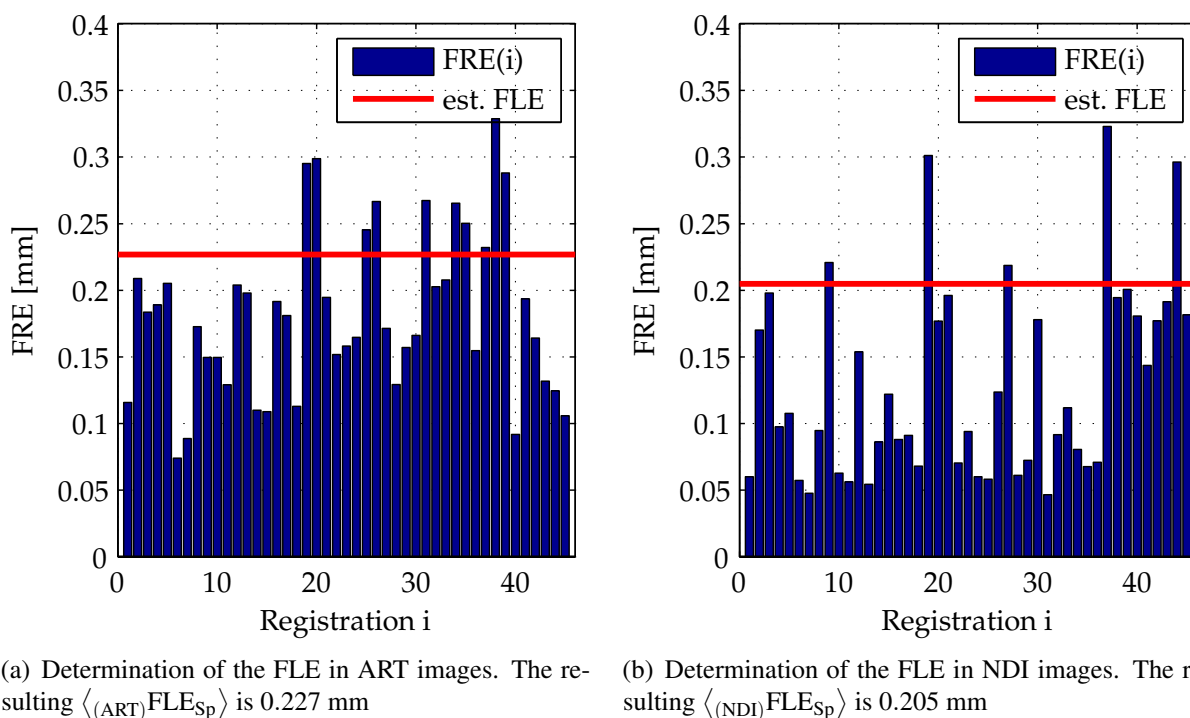
**Figure 3.20:** FLE of 5 mm spherical anchors in physical space

mated $\left\langle _{(Faro)}FLE_{Sp}\right\rangle$ corresponds with the given uncertainty of the measurement arm and proves the validity of the FLE determination methodology.

### 3.5.4 Joint FLE in Physical and Image Space

The FLE of the complete registration process includes errors in the image space as well as errors in the physical space of the localizer. Both have been quantified in the previous sections. Using Equation 3.3, the joint FLE can be calculated by

$$\left\langle _{(VCT+NDI)}FLE_{Sp}\right\rangle = \sqrt{0.150^2 + 0.205^2}\ mm = 0.254\ mm.$$

Since the same set of fiducials was used for the estimation of the $\left\langle _{(VCT)}FLE\right\rangle$ and $\left\langle _{(NDI)}FLE\right\rangle$, respectively an experimental determination of the joint FLE is also possible. By registering the fiducial point sets of the localizer space with the image space a further determination for the joint $\left\langle _{(VCT+NDI)}FLE'_{Sp}\right\rangle$ is available. This allows to compare the experimental results with the theoretical assumptions. The results are depicted in Figure 3.22. $\left\langle _{(VCT+NDI)}FLE'_{Sp}\right\rangle$ was determined to 0.237 mm which is 0.017 mm lower compared to the theoretical estimated joint $\left\langle _{(VCT+NDI)}FLE_{Sp}\right\rangle$. The similarity of these results emphasizes the validity of the chosen assumption of independent error distributions.

(a) FARO Gage portable measurement arm (www.faro.com).
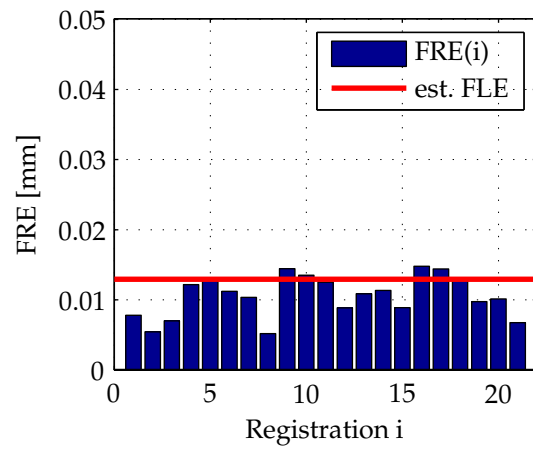
(b) The estimated $\left\langle _{(Faro)}FLE_{Sp}\right\rangle$ is 0.013 mm. The reference value for the measurement uncertainty is 0.0148 mm.

**Figure 3.21:** Determination of the localization accuracy using a portable measurement arm
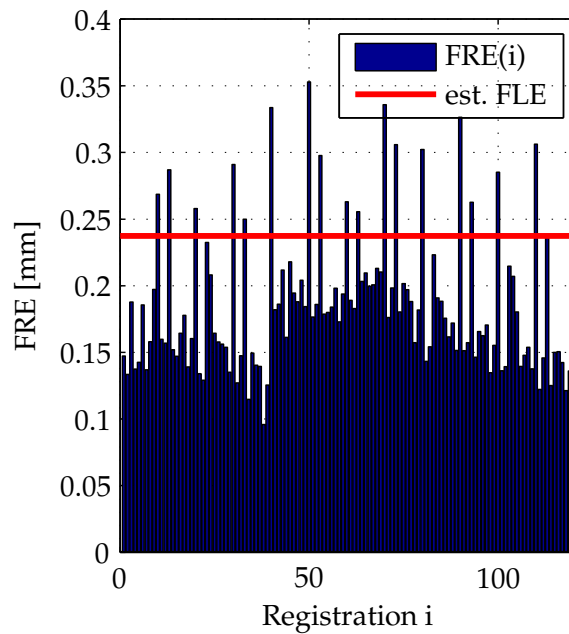


**Figure 3.22:** Joint FLE of VCT to NDI registration. The resulting $\left\langle _{(VCT+NDI)}FLE'\right\rangle$ is 0.237 mm.

### 3.5.5 Summary of FLE Estimations

Fiducial point localization is a process which is affected on the one hand by the chosen measurement system and on the other hand by the shape of the fiducials. The FLE cannot be measured, if the true location of a fiducial is not known. Instead, experiments can be performed in order to get an approximation of the FLE under the assumptions of independence and normality of the spatial error distribution. The measurements using the FARO Gage measurement arm show that this approach results in a good approximation of the measurement uncertainty. The results of FLE-estimates indicate that spheres can be localized significantly more accurately compared to screws. The highest accuracy can be achieved by using sphere fiducials in conjunction with VCT imaging and an automatic determination of the fiducial point coordinates. Table 3.3 summarizes the results of the FLE investigations.

**Table 3.3:** Results of theoretical and experimental FLE estimation

| Measurement space | $\langle \mathbf{FLE_{Sc}} \rangle$ [mm] | $\langle \mathbf{FLE_{Sp}} \rangle$ [mm] |
|---|---|---|
| MSCT (Manual) | 0.268 | 0.191 |
| MSCT (Automatic) | - | 0.166 |
| VCT (Automatic) | - | 0.150 |
| ART | - | 0.227 |
| NDI | 0.319 | 0.205 |
| Faro | - | 0.013 |
| NDI+VCT (theoretical) | - | 0.254 |
| NDI+VCT (experimental) | - | 0.237 |

## 3.6 Calibration of Instruments

In the context of IGS, instrument calibration includes the process of computing the position of an instrument's tool center point (tcp) in relation to the attached coordinate frame of the reference adapter (CRF). This step has to be performed prior to the start of the IGS application. The result of the calibration procedure is a vector $_{(CRF)}\mathbf{x}_{tcp}$ that contains the coordinates of the tcp in relation to the attached CRF. The calibration vector is used by the navigation system in order to measure the actual position of the tcp. As a consequence, any calibration error embedded in this vector substantially decreases the accuracy of the intervention. These errors have to be avoided, which is the reason why the calibration has to be performed with exceptional care.

During an mCIS, two different types of instruments are tracked by the localizer that are of special interest: a pointing device (pt) and a surgical drill. The calibration procedures for both devices are discussed in the following.

### 3.6.1 Pointing Device

The pointing device is used to measure the position of an arbitrary point within the measurement volume of the localizer by moving its tip to this point. It is particularly used during the registration

step of IGS applications, where the locations of fiducials have to be measured by the tracking system.

A common method for the calibration of the pointer is the pivoting method. It consists of rotating the pointer around its tool center point, while measuring the poses $^{\text{loc}}\mathbf{T}_{\text{CRF}}(i)$ of the pointer's CRF in relation to the localizer's coordinate frame during the pivot process. The tip of the pointer is defined as being located at the center of rotation $_{\text{(loc)}}\mathbf{x}_{\text{Pivot}}$. This means that the CRF is moving on a spherical trajectory around this point (see Figure 3.23).
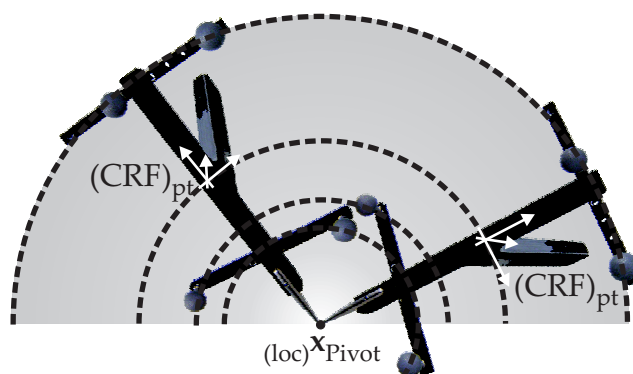


**Figure 3.23:** Calibration of a pointing device using the pivoting method. The tip of the pointer is defined as the center of rotation (pivot point $_{\text{(loc)}}\mathbf{x}_{\text{Pivot}}$).

The pose information of the pointer during pivoting can be mathematically described by

$$_{\text{(loc)}}\mathbf{x}_{\text{Pivot}} = {}^{\text{loc}}\mathbf{T}_{\text{CRF}}(i) \; _{\text{(CRF)}}\mathbf{x}_{\text{pt}} \tag{3.15}$$

where $_{\text{(loc)}}\mathbf{x}_{\text{Pivot}}$ is the unknown pivot point and $_{\text{(CRF)}}\mathbf{x}_{\text{pt}}$ the calibration vector. Since the number of measurements $N$ is large, a highly overdetermined system of equation

$$\begin{pmatrix} {}^{\text{loc}}\mathbf{T}_{\text{CRF}}(1) & -\mathbf{I} \\ {}^{\text{loc}}\mathbf{T}_{\text{CRF}}(2) & -\mathbf{I} \\ \vdots \\ {}^{\text{loc}}\mathbf{T}_{\text{CRF}}(N) & -\mathbf{I} \end{pmatrix} \begin{pmatrix} _{\text{(CRF)}}\mathbf{x}_{\text{pt}} \\ _{\text{(loc)}}\mathbf{x}_{\text{Pivot}} \end{pmatrix} = \mathbf{0} \tag{3.16}$$

can be set up, which can be solved in a least square manner. Further information for the derivation of the pivot method can be taken for example from [Bau07].

**Calibration Error**

The pivot method uses the data of the tracking system, which is not perfectly accurate. Therefore, the result of the calibration is affected by an error

$$\varepsilon_{\text{pt}} = \left\| {}_{(\text{CRF})}\mathbf{x}_{\text{pt}} - {}_{(\text{CRF})}\hat{\mathbf{x}}_{\text{pt}} \right\|_2. \tag{3.17}$$

The assessment of this error is a difficult task, since the true location of the pointer tip $\hat{\mathbf{x}}_{\text{pt}}$ is not known and every single measurement is affected by a number of errors. The remaining error $\varepsilon_{\text{pt}}$ in Equation 3.17 can only be minimized for the given measurement samples but it is generally not zero. Figure 3.24 illustrates this aspect. The deviations $\Delta x$, $\Delta y$ and $\Delta z$ of the pointer's tip from the calculated pivot point ${}_{(\text{loc})}\mathbf{x}_{\text{Pivot}}$ are plotted in this figure. Even after applying a low pass filter to the measurement data in order to reduce the effect of the measurement noise, a range of $r_x = 0.086$ mm, $r_y = 0.109$ mm and $r_z = 0.220$ mm can be observed in the directions $x$, $y$ and $z$ of the localizer.

The reason for the remaining calibration errors are ambiguous. The true location of the instrument's tip could have been moved unintentionally away from the pivot point during the pivoting procedure. This may be caused either by the person which manually guides the instrument but also by the shape of the tip which is usually not exactly pointed. This would yield to a rolling motion of the tip during the pivoting movement thus decreasing the accuracy of the calibration result. The thermal drift effect of the localizer may also have an influence to the calibration results. This, however, shows that the remaining calibration error is ambiguous and its vector cannot be determined by the localizer. Instead, other assumptions have to be taken into account for this purpose.

**Assessment of the Calibration Error Value with Respect to the Pointer Geometry**

Ignoring the presence of anisotropy and assuming that errors are isotropically distributed and that they can be sufficiently described by the statistics of a normal distribution allows for the use of the mathematics as described in Section 3.2. Errors within the measurement data of the pointing device can be broken down into two main components: the first is a tracking error of the pointer tip which is caused by a defective localization of the pointer's reference frame and can be described by a $\text{TRE}_{\text{pt}}$. The second is a calibration error $\varepsilon_{\text{pt}}$ which remains constant during the process of measurement, but has an unknown spatial direction.

An approximation of the expected size of the calibration error $\langle \varepsilon_{\text{pt}} \rangle$ can be obtained by looking at the process of measuring fiducial points with the pointing device. The measurement deviation between an arbitrary fiducial point $\mathbf{x}_i$ and its true location $\hat{\mathbf{x}}_i$ can be described by

$$\left\| \mathbf{x}_i - \hat{\mathbf{x}}_i \right\|_2 = \text{TRE}_{\text{pt}}(i) + \varepsilon_{\text{pt}}. \tag{3.18}$$

In Section 3.5.3, an expected error $\langle {}_{\text{NDI}}\text{FLE} \rangle$ has been estimated for this type of measurement with a pointing device. $\langle {}_{\text{NDI}}\text{FLE} \rangle$ is affected by the calibration error $\varepsilon_{\text{pt}}$, since the orientation of
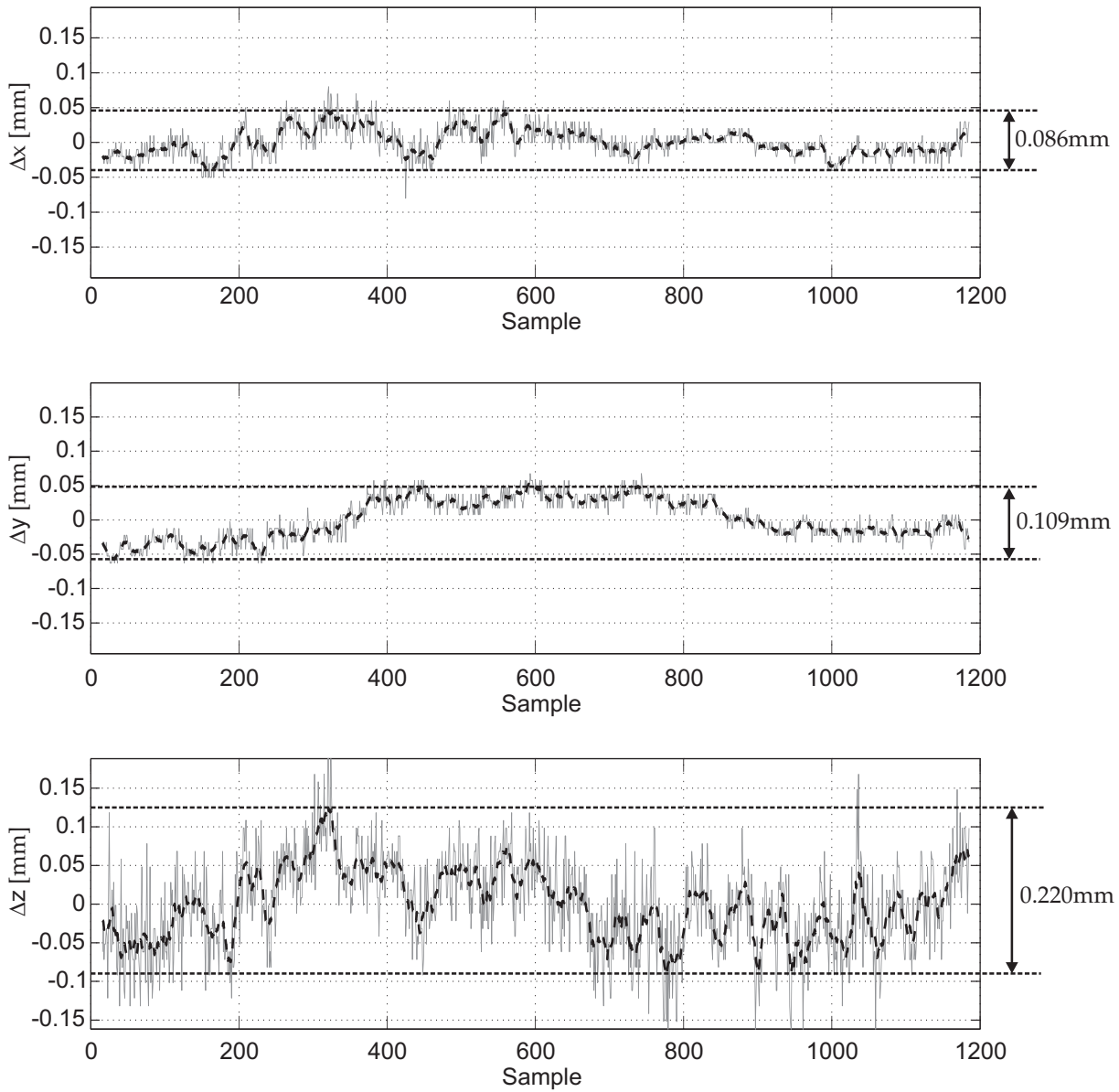
**Figure 3.24:** Displacements between the pointer's actual tip position and the calculated pivot point during the calibration movement

the pointer is changed during the process of different measurements. Thus, the unknown direction of the calibration error changes at each fiducial point. It is therefore modeled as a statistically distributed part of the calibration process and independent of the tracking error $\text{TRE}_{\text{pt}}$ of the pointer tip. This assumption allows to describe the expected value of $\langle_{\text{NDI}}\text{FLE}\rangle$ as

$$\langle_{\text{NDI}}\text{FLE}^2\rangle = \langle_{\text{NDI}}\text{TRE}_{\text{pt}}^2\rangle + \langle\varepsilon_{\text{pt}}^2\rangle. \tag{3.19}$$

This equation can be converted to

$$\langle\varepsilon_{\text{pt}}\rangle = \sqrt{\langle_{\text{NDI}}\text{FLE}^2\rangle - \langle_{\text{NDI}}\text{TRE}_{\text{pt}}^2\rangle} \tag{3.20}$$

in order to estimate $\langle\varepsilon_{\text{pt}}\rangle$ based on estimations of $\langle_{\text{NDI}}\text{FLE}^2\rangle$ as well as $\langle_{\text{NDI}}\text{TRE}_{\text{pt}}^2\rangle$.
$\langle_{\text{NDI}}\text{FLE}\rangle$ was estimated in Section 3.5.3 to 0.205 mm (cp. Figure 3.20(b)). For an approximation of $\langle_{\text{NDI}}\text{TRE}_{\text{pt}}^2\rangle$, the geometrical setup of the pointer in conjunction with the expected localization error of the reflective markers by the NDI camera (denoted as $\langle_{\text{NDI}}\text{MLE}\rangle$) can be used. $\langle_{\text{NDI}}\text{MLE}\rangle$ was estimated in [Lei96] to 0.35 mm for a mean of 30 measurement samples. Nevertheless, the number of samples, which are taken per fiducial can be chosen by the user. Since the target is usually not in motion during registration, a large amount of measurement samples can be taken per fiducial in order to reduce the effect of random errors during the localization process. Furthermore, the relationship between the geometrical marker arrangement and the target point as given in Equation 3.8 can be used to determine $\langle_{\text{NDI}}\text{TRE}_{\text{pt}}^2\rangle$. However, $\langle_{\text{NDI}}\text{MLE}\rangle$ given for a specified number of 30 samples per fiducial point. Therefore, Equation 3.8 needs to be extended by the factor $\frac{30}{S}$ to

$$\langle_{\text{NDI}}\text{TRE}_{\text{pt}}^2\rangle = \frac{30}{S}\left(\frac{1}{N}\left(1 + \frac{1}{3}\sum_{k=1}^{3}\frac{d_k^2}{f_k^2}\right)\langle_{\text{NDI}}\text{MLE}^2\rangle\right), \tag{3.21}$$

in order to cover the case of an arbitrary number $S$ of taken measurement samples per fiducial point. The geometrical parameters of the pointer are given in Table 3.4.

**Table 3.4:** Geometrical setup of the pointer

| Parameter | Value |
|---|---|
| $\langle_{\text{NDI}}\text{MLE}^2\rangle\,(S = 30)$ | $(0.35\text{ mm})^2$ |
| Number of measurement samples $S$ per fiducial | 100 |
| Distances $d_i$ between the pointer's tcp and the principal axes $i$ of the marker configuration | $d_1 \approx 150\text{ mm}$ $d_2 \approx 150\text{ mm}$ $d_3 \approx 0\text{ mm}$ |
| RMS-distances $f_i$ between the markers and the principal axes $i$ of the marker configuration | $f_1 \approx 50\text{ mm}$ $f_2 \approx 80\text{ mm}$ $f_3 \approx 0\text{ mm}$ |
| Resulting $\langle_{\text{NDI}}\text{TRE}_{\text{pt}}^2\rangle$ | $(0.135\text{ mm})^2$ |

Applying the values of Table 3.4 to Equation 3.21 results in a $\langle_{\text{NDI}}\text{TRE}_{\text{pt}}\rangle$ of 0.135 mm. The

calibration error $\langle \varepsilon_{\mathrm{pt}} \rangle$ can finally be calculated with Equation 3.20 to

$$\langle \varepsilon_{\mathrm{pt}} \rangle = 0.156 \text{ mm}.$$

### 3.6.2 Surgical Drill

For the calibration of the surgical drill, the location of the drill's tool center point as well as the orientation of the drill axis are required. Hence, a transformation matrix $^{\mathrm{drill}}\mathbf{T}_{\mathrm{CRF}}$ describing the position and orientation of the drill bit is needed instead of a calibration vector. This is why the pivoting method cannot be used for the calibration process, since it only provides the tool center point. A calibration methodology providing the pose of the drill has been introduced in [BEM$^+$10]. It is described in the following.

Two calibration bits with different lengths are used for the calibration of the drill. Each of them contains a 5 mm sphere at its tip (see Figure 3.25(b)). The bits are inserted subsequently into the drill holder and the locations $_{\mathrm{(CRF)}}\mathbf{x}_{\mathrm{cb1}}$ and $_{\mathrm{(CRF)}}\mathbf{x}_{\mathrm{cb2}}$ of the two spheres in relation to the drill's *CRF* are measured with a pointer tool. The orientation of the drill is defined with the $z$-axis pointing along the bit shaft while the $x$-axis is oriented towards the localizer. The coordinates of the two calibration bits can be used to determine the orientation of the drill. In addition, the given difference in length $\Delta\ell$ of the surgical drill and the longer calibration bit (cb1) is measured with a caliper. It is used in order to determine the position of the drill's tip. $^{\mathrm{drill}}\mathbf{T}_{\mathrm{CRF}}$ is defined by

$$^{\mathrm{drill}}\mathbf{T}_{\mathrm{CRF}} = \begin{bmatrix} \mathbf{e}_x & \mathbf{e}_y & \mathbf{e}_z & _{\mathrm{(CRF)}}\mathbf{x}_{\mathrm{cb1}} + \Delta\ell \; \mathbf{e}_z \\ 0 & 0 & 0 & 1 \end{bmatrix}, \tag{3.22}$$

where

$$\mathbf{e}_z = \frac{_{\mathrm{(CRF)}}\mathbf{x}_{\mathrm{cb2}} - _{\mathrm{(CRF)}}\mathbf{x}_{\mathrm{cb1}}}{\left\| _{\mathrm{(CRF)}}\mathbf{x}_{\mathrm{cb2}} - _{\mathrm{(CRF)}}\mathbf{x}_{\mathrm{cb1}} \right\|_2},$$

$$\mathbf{e}_x = \frac{\mathbf{e}_z \times \begin{bmatrix} 0 & -1 & 0 \end{bmatrix}^T}{\left\| \mathbf{e}_z \times \begin{bmatrix} 0 & -1 & 0 \end{bmatrix}^T \right\|_2}, \text{ and}$$

$$\mathbf{e}_y = \mathbf{e}_z \times \mathbf{e}_x$$

are unit vectors describing the orientation of the drill in relation to its CRF. $\mathbf{e}_z$ is calculated using the coordinates of the calibration bits, while $\mathbf{e}_y$ is defined perpendicular to $\mathbf{e}_z$ and pointing in the direction of the localizer's coordinate frame. Figure 3.25(a) illustrates the definition of the drill's coordinate system.

### Assessment of the Drill Calibration Error

The inaccuracy of the drill's calibration process primarily depends on the measurement uncertainty of each calibration bit's position vector $_{\mathrm{(CRF)}}\mathbf{x}_{\mathrm{cb1}}$ and $_{\mathrm{(CRF)}}\mathbf{x}_{\mathrm{cb2}}$. Besides a position error,

(a) Definition of the drill's coordinate frame.

(b) Lindemann cutting bit, used for mCIS drilling and correspondent calibration bits with 5 mm spheres.
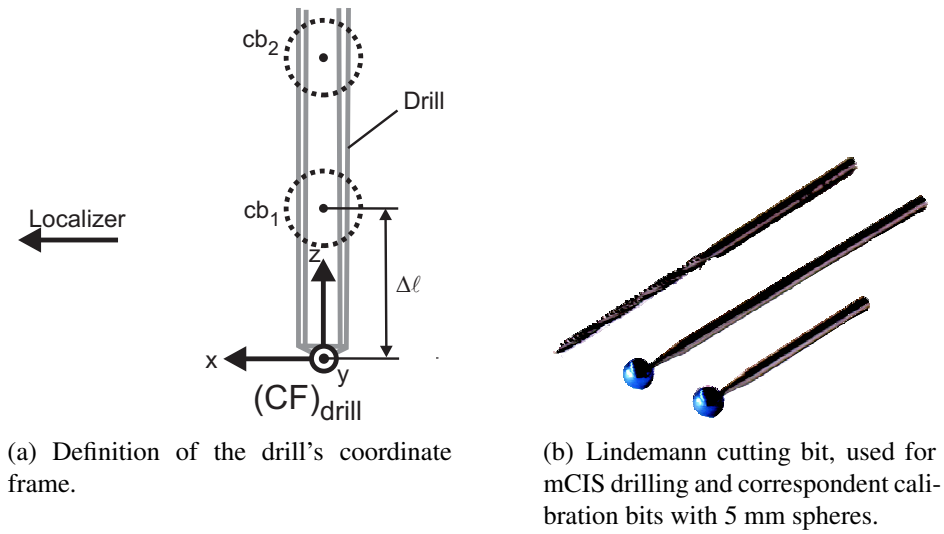
**Figure 3.25:** Calibration of the drill bit

an angular error additionally occurs during the determination of the drill's orientation based on these vectors. Nevertheless, since the difference in the length of the calibration bits is large, it is assumed that the angular error is small. Since the calibration bit 1 and the drill have nearly the same size, deviations caused by angular errors can be neglected for the determination of the calibration error $\varepsilon_{\text{tcp}}$ at the tip of the drill. Therefore, $\varepsilon_{\text{tcp}}$ can be approximated by the localization error of the 5 mm spheres in the measurement space of the localizer. This corresponds with the FLE estimation of sphere fiducials as described in Section 3.5.3 (cp. Figure 3.20(b)) so that the expected calibration error of the drill can be approximated by

$$\langle \varepsilon_{\text{drill}} \rangle \approx \langle _{\text{(NDI)}}\text{FLE}_{\text{Sp}} \rangle = 0.205 \text{ mm}. \tag{3.23}$$

## 3.7 Robotic Guidance

As described in Section 2.5, robots have the advantage of an excellent geometric accuracy compared to humans. The use of robotic assistance allows a stable guidance of the instrument according to the instructions of the navigation system, so that the intervention can be performed as defined in the surgical plan. Therefore, the robot has to be connected to the navigation system in order to receive actual poses of the instrument.

Various error sources have to be taken into account, when assessing the spatial deviation $\Delta_R$ of the robotic guidance. Generally, the absolute positioning accuracy of a robot is affected by inaccuracies of the robot's kinematic model which is used by the internal control to actuate each of its joints, as well as by dynamic errors caused by system latencies. Inaccuracies of the kinematic model and small changes of the robotic structure due to temperature effects usually yield to an insufficient absolute positioning accuracy. These are not acceptable for surgical interventions

at the lateral skull base. However, positioning errors of the robot can be significantly reduced by a suitable feedback control architecture. The actual pose of the instrument's tip is constantly measured by the localizer and fed back to the robot controller in order to adjust its movements. The advantage of this approach is that errors that included in the registration of the robot's base coordinate frame and the instrument are compensated by the controller.

Several approaches exist for this type of feedback control. In order to further increase the system's accuracy, a reduced speed of motion as well as an increased sampling rate of the localizer measurements in conjunction with high speed data transfer and calculations are also included. Furthermore, hardware with realtime capabilities is used in order to ensure a determinism of time delays. A way to cope with these latencies is the use of additional sensors in combination with model predictive filters. Detailed information about such an approach can be taken from [KBE$^+$07, BEM$^+$10].

Even with the use of continuous feedback control, it has to be considered that the capability of the robot to position its end effector is still limited. This means that instruments can only be positioned by the robot with a certain level of accuracy which depends on the joint configuration of the robot and the physical resolution of its internal sensors. This type of error varies over the robot's workspace, which is why it is usually not provided by manufacturers. However, an upper limit of this value may be obtained by taking the repeatability, which is the deviation that occurs, while the robot moves its end effector to the same position from the same initial direction several times. This type of error is also primarily affected by the actual configuration of the robot structure and the resolution of the joint encoders. In addition to that, this value is provided by robot manufacturers. For a *Kuka KR3* robot, which is used for mCIS experiments, the repeatability is given in [KUK] by 0.05 mm. It is taken as an approximation of the robot's expected positioning error

$$\langle \Delta_R \rangle \approx 0.05 \text{ mm}.$$

## 3.8 Theoretical Determination of the TNE

The given approximations of the inaccuracies that occur during the localization and registration process can be used in order to calculate an estimate for the expected TNE of an mCIS setup. According to Equation 3.9, the TNE can be determined particularly from three components, which are

- the expected target registration error $\langle \text{TRE}_{\text{co}} \rangle$ of the cochleostomy point,

- the expected target registration error $\langle \text{TRE}_{\text{drill}} \rangle$ of the drill's tcp and

- the expected positioning error $\langle \Delta_R \rangle$ of the robot.

These are discussed in the following.

### 3.8.1 Target Registration Error of the Cochleostomy Point

For the determination of the $\langle \text{TRE}_{\text{co}} \rangle$ of the cochleostomy point, the combined fiducial localization error $_{(\text{phys+img})}\text{FLE}$ can be used in conjunction with the spatial relationship of the fiducial points and the cochleostomy point. The underlying mathematical approach is described in Equation 3.8. Table 3.5 gives an overview of the geometrical distribution of the fiducial points for a typical experimental mCIS setup.

**Table 3.5:** Typical spatial relationship between fiducial points and the cochleostomy point

| Parameter | Value |
|---|---|
| Number $N_{\text{fp}}$ of fiducial points | 5 |
| Distances $d_i$ between the cochleostomy point and the principal axes $i$ of the fiducial point configuration | $d_1 \approx 30$ mm<br>$d_2 \approx 30$ mm<br>$d_3 \approx 0$ mm |
| RMS-distances $f_i$ between the fiducial points and the principal axes $i$ of their spatial configuration | $f_1 \approx 25$ mm<br>$f_2 \approx 25$ mm<br>$f_3 \approx 25$ mm |

In contrast to the procedure of the FLE estimation as described in Section 3.5.4, fiducial points are measured from almost the same direction during an mCIS. To take this into account, the combined $_{(\text{phys+img})}\text{FLE}$ is broken down into errors occurring in the image space ($_{(\text{img})}\text{FLE}$) as well as in the physical space ($_{(\text{phys})}\text{FLE}$). It is assumed that the fiducial points are measured with a pointer as specified in Section 3.6.1 using an *NDI* localizer. Hence, $_{(\text{phys})}\text{FLE}$ corresponds with the target registration error $_{(\text{NDI})}\text{TRE}_{\text{pt}}$ of the pointer in the *NDI* measurement space. By using this relationship, $\langle \text{TRE}_{\text{co}}^2 \rangle$ of the cochleostomy point can be calculated as follows:

$$
\begin{aligned}
\langle \text{TRE}_{\text{co}}^2 \rangle &\approx \frac{1}{N_{\text{fp}}} \left( 1 + \frac{1}{3} \sum_{k=1}^{3} \frac{d_k^2}{f_k^2} \right) \langle {}_{(\text{phys+img})}\text{FLE}^2 \rangle \\
&\approx \frac{1}{N_{\text{fp}}} \left( 1 + \frac{1}{3} \sum_{k=1}^{3} \frac{d_k^2}{f_k^2} \right) \left( \langle {}_{(\text{img})}\text{FLE}^2 \rangle + \langle {}_{(\text{phys})}\text{FLE}^2 \rangle \right) \qquad (3.24) \\
&\approx \frac{1}{N_{\text{fp}}} \left( 1 + \frac{1}{3} \sum_{k=1}^{3} \frac{d_k^2}{f_k^2} \right) \left( \langle {}_{(\text{img})}\text{FLE}^2 \rangle + \langle {}_{(\text{NDI})}\text{TRE}_{\text{pt}}^2 \rangle \right).
\end{aligned}
$$

With $\langle {}_{(\text{img})}\text{FLE}^2 \rangle = (0.150 \text{ mm})^2$, $\langle {}_{(\text{NDI})}\text{TRE}_{\text{pt}}^2 \rangle = (0.135 \text{ mm})^2$, and $N_{\text{fp}}$, $d_k$, $f_k$ according to Table 3.5, this yields

$$
\langle \text{TRE}_{\text{co}}^2 \rangle \approx (0.126 \text{ mm})^2. \qquad (3.25)
$$

Equation 3.25, however, does not account for the calibration error of the pointer. This means that the expected calibration error $\langle \varepsilon_{\text{pt}} \rangle$ is a constant vector of unknown direction, which is embedded in each fiducial point measurement. As a consequence, the location of the cochleostomy point is determined with the same offset. This states a systematic error of unknown direction that cannot be treated in the same way as the statistical process of fiducial point localization. Instead, the value

of the effective target registration error $\langle \text{TRE}'_{\text{co}} \rangle$ is assumed to be a sum of the calibration error $\langle \varepsilon_{\text{pt}} \rangle$ and the uncertainty of the cochleostomy point localization $\text{TRE}_{\text{co}}$. For $\langle \varepsilon_{\text{pt}} \rangle$, as estimated in Section 3.6.1 this yields

$$
\begin{aligned}
\langle \text{TRE}'_{\text{co}} \rangle &\approx \langle \text{TRE}_{\text{co}} \rangle + \langle \varepsilon_{\text{pt}} \rangle \\
&\approx 0.126 \text{ mm} + 0.156 \text{ mm} \\
&\approx 0.282 \text{ mm}.
\end{aligned}
\tag{3.26}
$$

### 3.8.2 Target Registration Error of the Drill

For the determination of the $\langle \text{TRE}_{\text{drill}} \rangle$, not only calibration errors but also tracking errors have to be considered. It is shown in Section 3.6.2 that the calibration error $\varepsilon_{\text{drill}}$ can be approximated for the given calibration methodology by the FLE of the sphere fiducials, which is approximately 0.205 mm.

Besides the calibration error, $\text{TRE}_{\text{drill}}$ is also influenced by a stochastically distributed tracking error. It depends on the spatial arrangement of the marker in relation to the tip of the drill and the number of samples, which are taken to calculate its actual pose. With a given spatial setup of the marker, this error can be calculated by using Equation 3.21. Nevertheless, the stochastic tracking error can be reduced by using a large number of measurement samples.

For the given experimental setup of the image guided robot, a control architecture was implemented that considers both a large number of measurement samples from the localizer and joint encoder values of the robot. The measurement noise of the drill's calculated pose is significantly reduced by this approach [BEM$^+$10]. Dynamic errors are further reduced by the fact that the drill is guided by the robot with very low speed during the drilling process. Hence, it is assumed that the measurement noise can be neglected for the control architecture. $\text{TRE}_{\text{drill}}$ can then be approximated by the calibration error of the drill, which was estimated in Section 3.6.2:

$$
\text{TRE}_{\text{drill}} \approx \varepsilon_{\text{drill}} = 0.205 \text{ mm}.
$$

### 3.8.3 Positioning Error $\Delta_R$ of the Robot and TNE Estimation

As discussed in Section 3.7, the expected positioning error of the robot $\langle \Delta_R \rangle$ can be approximated by its repeatability given by $\langle \Delta_R \rangle \approx 0.05$ mm. Taking this into account, the $\langle \text{TNE}^2 \rangle$ can finally be estimated to

$$
\begin{aligned}
\langle \text{TNE}^2 \rangle &= \langle \text{TRE}^2_{\text{co}} \rangle + \langle \text{TRE}^2_{\text{tcp}} \rangle + \langle \Delta^2_R \rangle \\
&= (0.282 \text{ mm})^2 + (0.205 \text{ mm})^2 + (0.05 \text{ mm})^2 \\
&= (0.352 \text{ mm})^2.
\end{aligned}
\tag{3.27}
$$

$\langle \text{TNE}^2 \rangle$ describes the variance of a statistically distributed error during a navigation process. Nevertheless, a more suitable description of the expected accuracy would be a description depending on a confidence region of 95% or even 99.9%. For a Gaussian normal distribution these are given

by $1.96\sigma = 0.690$ mm for the 95% confidence region and $3.29\sigma = 1.158$ mm for the 99.9% confidence region, respectively. Table 3.6 provides a summary of the estimated error values.

**Table 3.6:** Summary of estimated navigation errors in a robot assisted mCIS

| Error type | Value [mm] |
|---|---|
| $\left\langle \mathrm{TRE}_{\mathrm{co}}^{2} \right\rangle$ | 0.282 mm |
| $\left\langle \mathrm{TRE}_{\mathrm{tcp}}^{2} \right\rangle$ | 0.205 mm |
| $\left\langle \Delta_{R} \right\rangle$ | 0.050 mm |
| $\left\langle \mathrm{TNE} \right\rangle$ | 0.352 mm |
| 95% confidence region | 0.690 mm |
| 99.9% confidence region | 1.158 mm |

**Discussion**

A theoretical determination of the expected TNE of a given confidence region allows to predict the accuracy of the navigation process. Nevertheless, it has to be pointed out that this value is based on various assumptions, such as an isotropic behavior of errors and a statistical description of errors using normal distribution. Furthermore, effects such as a deformation of components due to the applied forces during the drilling process are not taken into account. That is why empirical evaluations of the TNE also have to be performed in order to provide meaningful information about the expected error of a robot assisted mCIS. They are described in chapter 4.

## 3.9 Conclusions for further mCIS Experiments

In this chapter each step of an image guided and robotic assisted intervention has been analyzed and the following improvements can be suggested to optimize the accuracy for the given setup of a robot assisted mCIS application.

- The use of a high resolutive image modality such as VCT improves the accuracy of the marker identification and registration.

- In contrast to manual segmentation, automatic methods used for the delineation of the anatomic structures in CT images reduce drastically the expenditure of time for the surgeon. However, the performance of automatic segmentation methods is addicted to the quality of the images. Results of these algorithms need to be verified in order to avoid errors in the location process of these structures. Manual segmentation is still the most reliable method and thus recommendable for interventions with high demands on accuracy.

- The facial nerve and the chorda tympani nerve are tubular structures. Filtering may be applied to the results of manual segmentation in order to smooth the facetted topology of the segmented structures. The results are assumed to be a suitable approximation of the true surface.

- Defining the coordinates of the mCIS is a challenging task, if done manually. The use of computer assisted planning algorithms allows to establish individual safety distances to adjacent structures such as the facial nerve and the chorda tympani nerve. Since this enhances the safety of the intervention, it is highly recommendable.

- Before starting an IGS application, it has to be ensured that the localizer has reached its operating temperature. Otherwise, thermal drift effects affect the tracking accuracy.

- The calibration of instruments being tracked is a sensitive process and can be affected by various types of errors. For safety reasons, it recommended to verify the calibration results and, if necessary, redo the calibration before starting a new series of experiments.

- The use of spherical fiducial markers results in a registration performance, which is more accurate compared to titanium screws.

- Drilling the canal of an mCIS requires a slow and steady movement of the drill towards the target. The use of a robot with an appropriate control architecture for the navigation of the instrument reduces lateral errors.

- An estimate of the expected TNE of a robot assisted mCIS can be determined based on various theoretical assumptions. It is determined to 1.158 mm for a 99.9% confidence region. Nevertheless, empirical evaluations of the TNE need to be performed in order to verify this value.

# 4 Empirical Evaluation of the Target Navigation Error

In the previous chapter, an expected TNE of the intended robot assisted mCIS setup has been calculated based on an error analysis of the included components. Nevertheless, this value model based including assumptions such as an isotropic error distribution. Therefore, it is necessary to additionally evaluate the TNE on the basis of experimental measurements in order to verify the applicability of these assumptions.

This chapter provides results of experimental TNE observations, which were acquired by using two different types of artificial phantoms. Both phantoms were designed to reproduce typical errors of the mCIS setup and include the possibility to measure the TNE. Section 4.1 provides information about the general setup of these experiments. The results are presented in the subsequent Sections 4.2 (phantom I) and 4.3 (phantom II), respectively. Finally, conclusions are drawn and consequences for further experiments on temporal bone specimens are discussed in Section 4.4.

## 4.1 Experimental Setup

The setup of the TNE experiments was chosen to reproduce the conditions of the mCIS drilling experiments including four main components: a localizer, a robot, a control computer, and a target device. The experimental setup also included methodologies to calibrate optically tracked instruments as described in Chapter 3. A closed loop control was established for the robotic assisted guidance of the instrument according to a defined path. Figure 4.1 depicts the principle of the experimental setup.

### Localizer

Two different optical localizers (Polaris®, Northern Digital Inc., Waterloo, Ontario, Canada and *ARTrack*2, Advanced Realtime Tracking GmbH, Weilheim, Germany) were used for the tracking of objects. Although they are from different manufacturers, it can be shown, that their measurement principle as well as the behavior of their measurement errors are very similar. The localizers were separately connected to the control computer in order to acquire pose information about reflective marker frames with a frequency of up to 60 Hz. The pose information of each component was used as a feedback signal inside the control architecture to control the robot's movements.

### Robot

Instead of retrofitting a medical robot device, an industrial robot (KUKA KR3, KUKA Roboter GmbH, Augsburg, Germany) was used for the experiments. Besides high stiffness and a repeatability of 0.05 mm, it provides a maximum workspace radius of 650 mm and maximum payload of
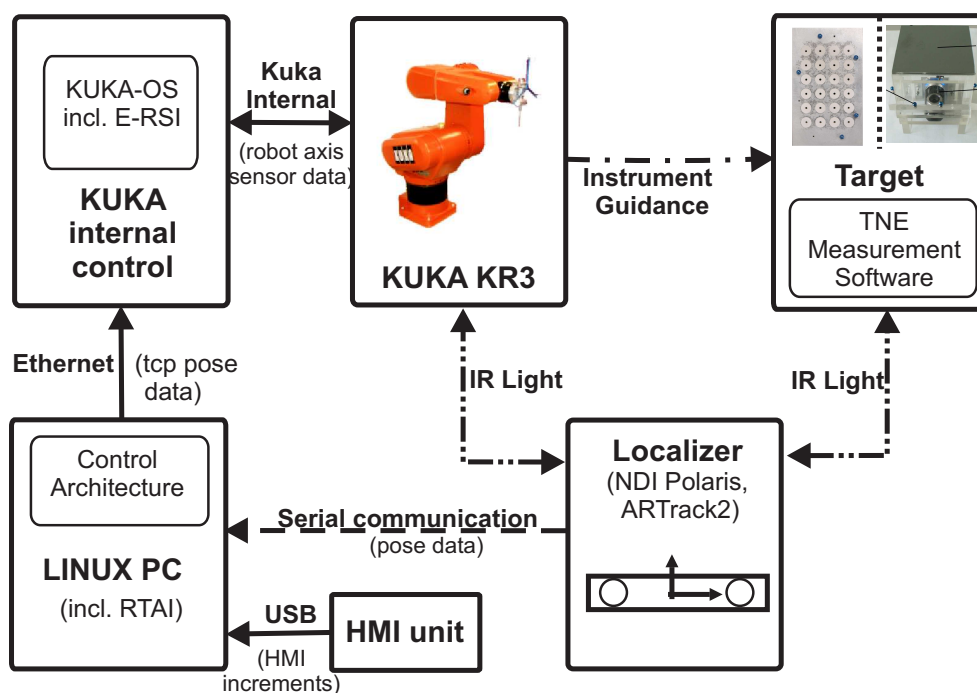
**Figure 4.1:** Communication setup of empirical TNE studies. Abbreviations: E-RSI: Ethernet Remote Sensor Interface; RTAI: Realtime Application Interface; HMI: Human-Machine-Interface.

3 kg. The control software of the KR3 was upgraded with an Ethernet Remote Sensor Interface (Kuka.Ethernet KRL XML), which enables data exchange with an external control computer via ethernet in a 12 ms cycle. Two different types of instruments were chosen for the experiments and separately attached to the end-effector of the robot: a surgical drill (see Section 4.2) and a laser pointer (see Section 4.3).

**Control Computer**

A computer with a real time operating system (Linux, extended with realtime application interface RTAI) was used to process pose information of the localizer and to send moving instructions to the robot. The rate of drill advancement along its desired trajectory was set manually by the operator using a human-machine-interface (HMI) which was also connected to the control computer. A closed loop control was established using the graphical environment of the rapid control prototyping system MATLAB/Simulink® (MathWorks Inc., Natick, Massachusetts). The data communication with the robot, the HMI, and the localizer were integrated in the source code using custom made software components. To run the control software on the computer, executable code was generated using the Real-Time Workshop (RTW) of Matlab. More detailed information about the control architecture can be found in [BEM+10].

**Target**

Instead of using biological specimens, artificial phantoms were employed to serve as target objects in this stage of the experiments. They were designed to provide a well defined target point, as well as reference structures which can be used to measure the TNE. They were additionally equipped with fiducials for registration purposes. The arrangement of the fiducials was chosen in a way to reproduce the typical setup for temporal bone specimen including the following characteristics:

- Number of fiducial points for registration: 4-6.

- Planar arrangement of fiducial points.

- Distance between fiducials and target point: $30 - 40$ mm.

Further information about the target objects are given in the following sections.

## 4.2 TNE Measurements Using Phantom I

The first series of TNE experiments consisted of drilling bore holes into a plaster filled aluminium phantom. After the drilling was completed, the TNE was determined by a coordinate measuring machine (CMM) which measured the position of the drilled bore holes as well as reference structures.

### 4.2.1 Design of TNE Phantom I

Two identical phantoms were manufactured. The design of each phantom was chosen to reproduce the main influencing factors of the localization, the registration process, and the drilling distance of an mCIS scenario. Each phantom consists of an aluminium block ($125 \times 75 \times 35$ *mm*$^3$) which was fabricated by using a highly accurate computerized numerical control (CNC) milling machine. Thus accurate reference structures in terms of geometrical structures were provided. A local coordinate frame was defined to be located at the upper left edge with the *x* and *y* axis pointing along the flanges of the aluminium block (see Figure 4.2). Each phantom was equipped with a grid pattern of 24 holes with a diameter of 10 mm, which were filled with plaster and body filler, respectively. For registration purposes, five M1.6 threaded holes were added to the phantom to mount 5 mm sphere fiducials. The exact positions of the spheres in relation to the local coordinate frame were determined by using a calliper with a resolution of 0.01 mm. A sum of 48 drill canals were defined along the centers of the prefabricated bore holes. The entry coordinates of the drill path were defined to be at the top side of the phantom, whereas the target coordinates were placed 2 mm below the bottom side to ensure that the drill reaches the bottom of the phantom and the bore holes can be measured by the CMM.
During drilling, the phantom was placed in a fixture with a reflective marker frame for the optical localization. A milling tool (Lindemann burr NS1808.036, KOMET MEDICAL, Lemgo, Germany) was used for the drilling. The calibration was performed according to Section 3.6.2
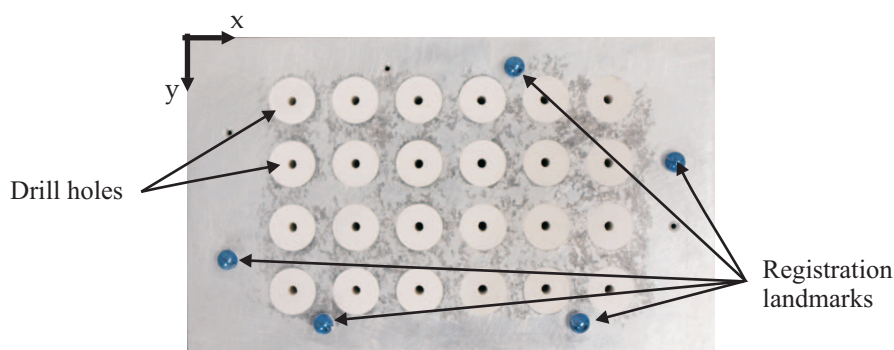
**Figure 4.2:** CNC fabricated device with plaster filled holes used for experimental TNE determination

with the help of two calibration bits. The milling tool was replaced and a new calibration was performed before starting the second series of drilling experiments on the second phantom. For all experiments, a constant rotational speed of $10,000$ rpm was used for the drill, while its feed rate along the defined path was controlled by the user with an HMI device. For every single drill hole, a new registration was performed. In addition to that, the phantom was repositioned several times within the measurement volume of the localizer. In particular, the following types of errors were included in the measured value of the TNE:

- Registration errors in context with the given fiducials.

- Calibration errors of the pointing device and the drill.

- Inaccurate pose estimation of reflective marker frames by the localizer.

- Limited spatial control of the robot's end effector.

- Errors due to forces that are applied to the instrument during drilling.

No imaging was done in order to define the drilling coordinates. Thus, errors resulting from that step of the workflow are not included in the measured TNE. Figure 4.3 depicts the experimental setup of the drilling process.

### 4.2.2 Results

A CMM (Zeiss ZMC 530, Carl Zeiss IMT GmbH, Oberkochen, Germany) was used to determine the position of each hole in relation to the phantom's local coordinate frame. The CMM has an accuracy of approximately $1\,\mu$m which allows for an accurate determination of the lateral TNE at the top and bottom side of the phantom. Table 4.2 summarizes the result of the accuracy experiments including a statistical analysis. The mean and standard deviation of the error at the top side of both phantoms was $-0.168 \pm 0.099$ mm in $x$ and $-0.031 \pm 0.193$ mm in $y$ direction. On the bottom side, a deviation of $-0.123 \pm 0.127$ mm in $x$ and $-0.097 \pm 0.307$ mm in $y$ was measured.
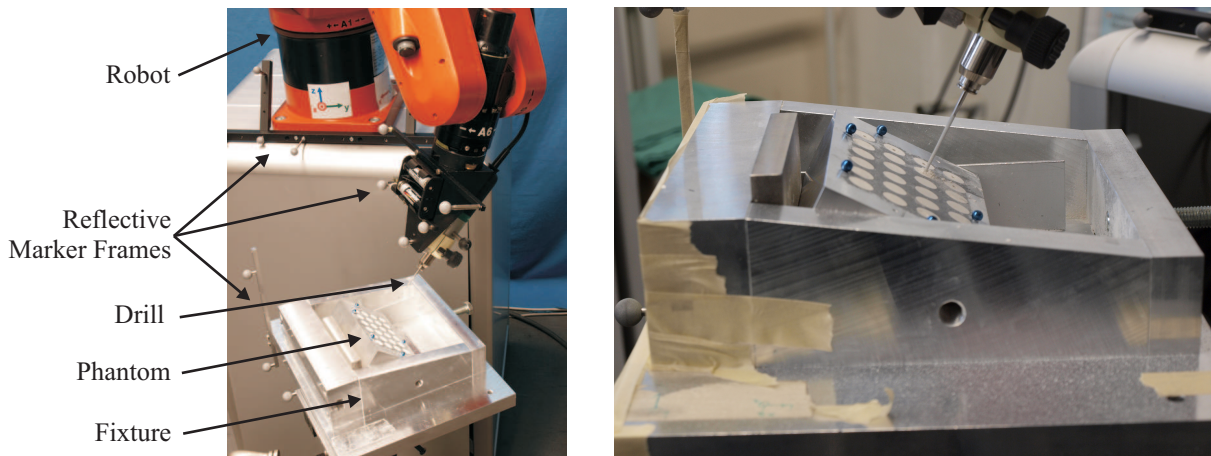
**Figure 4.3:** Drilling experiments using accuracy assessment phantom I

The result of a $\chi^2$-Goodness-of-Fit test shows that the hypothesis of a normal distribution of errors in $x$ and $y$ can not be rejected at a 5% significance level (p>0.05). Subsequently, a principal component analysis was performed and the direction of the largest error was determined. Assuming a two dimensional normal distribution allows to specify a 99.9% confidence region of the error in its largest direction. A worst case error can then be calculated by adding the norm of the mean error to the confidence region. It results in 0.819 mm for the top side and 1.167 mm for the bottom side, respectively.

**Table 4.1:** Lateral TNE [*mm*] of the preliminary accuracy tests

| | Mean value [mm] | | Standard deviation [mm] | | | | 99.9% confidence region [mm] | Mean (Norm) + confidence region |
|---|---|---|---|---|---|---|---|---|
| Experiment | $\Delta x$ | $\Delta y$ | $\Delta x$ | $\Delta y$ | Major axis | Minor axis | Major axis | Major axis [mm] |
| Top Side | -0.168 | -0.031 | 0.099 | 0.193 | 0.197 | 0.092 | 0.648 | 0.819 |
| Bottom Side | -0.123 | -0.097 | 0.127 | 0.307 | 0.307 | 0.127 | 1.011 | 1.167 |

Figure 4.4(a) and 4.4(b) depict the measured deviations of the drilled bore holes on the top and bottom side of the accuracy phantom. In addition to that, histograms and the corresponding Gaussian distribution are given for the $x$ and $y$ direction. Furthermore, the two dimensional 99.9% confidence region is plotted in the figures. As it can be seen the major axis of the error distribution almost corresponds with the $y$ direction of the phantom. This direction corresponds with the $z$ axis of the localizer, which is the direction with the highest error in localization.

(a) Top side.                            (b) Bottom side.
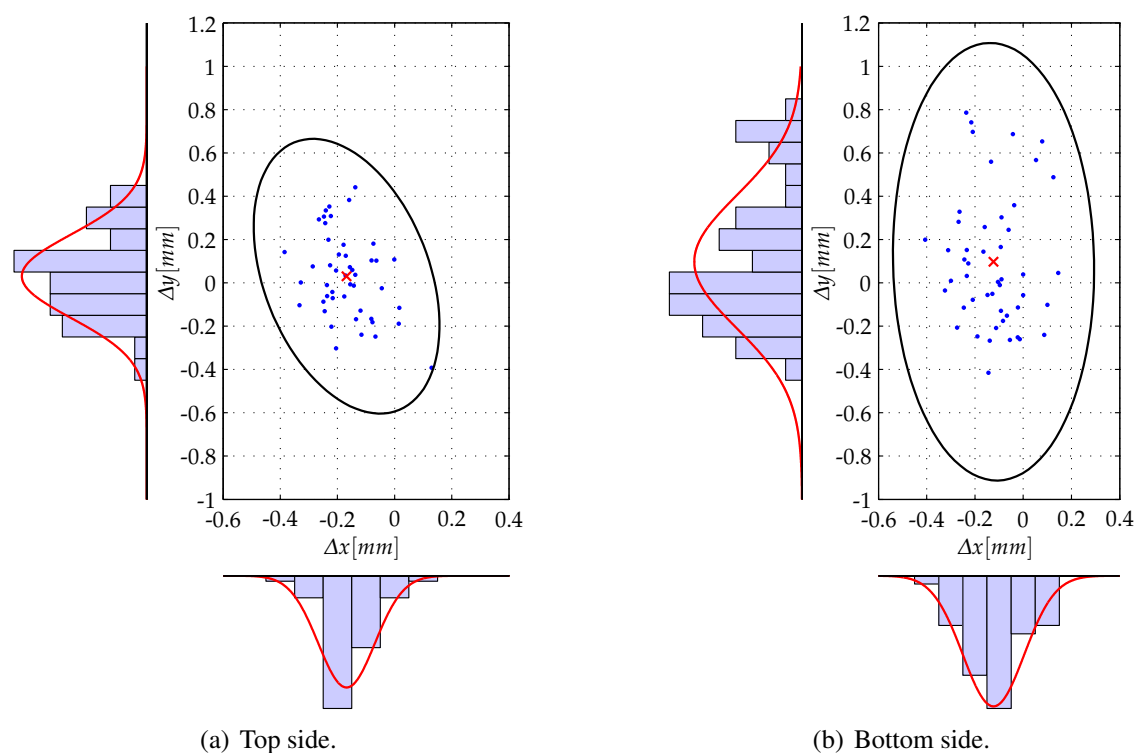
**Figure 4.4:** Measured deviations of the bore holes of accuracy phantom I and results of the statistical analysis including a 99.9% confidence region

## 4.3 TNE Measurements Using Phantom II

A second series of TNE experiments was performed using phantom II, which was made of poly methyl methacrylate (PMMA). Due to the use of PMMA, CT images of the phantom could be acquired so that coordinates of the target and fiducial points could be specified within the CT image space. Furthermore, a laser pointer was used instead of a drill in order to implement a methodology for the measurement of the TNE, which is nondestructive and repeatable (see Figure 4.5). The laser was guided by the robot with the beam pointing towards the phantom device. A camera measured the beam's projection on a semi transparent plane so that the lateral TNE of the instrument guidance was determined.

### 4.3.1 Design of the TNE Measurement Device

The TNE device consists of a cubic body with a size of $90 \times 90 \times 120 \ mm^3$. A reference adapter for optical localization and a camera with a two megapixel CMOS-sensor (Optia AF, Creative Technology Ltd.) were attached to the device. In order to compensate for lens distortion, the intrinsic parameters of the camera were calibrated using the camera calibration toolbox for Matlab® [Bou07]. To measure the TNE of the laser instrument, a semi transparent foil was affixed to the phantom on the top side which states the measurement plane of the device. The laser, which was
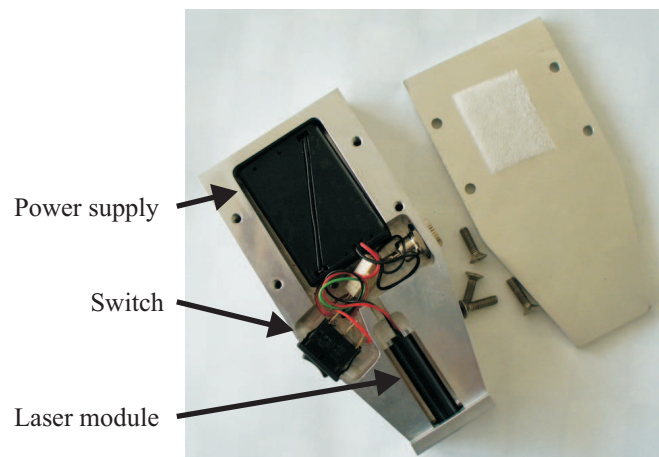
**Figure 4.5:** Laser module, replacing the drill and used for TNE measurements on phantom II

guided by the robot, produced a visible dot on the plane that was detected in the images of the camera unit. Figure 4.6 depicts the design of the phantom device.

Two types of registration landmarks were employed for the registration of CT images of phantom II to the physical space. These were on the one hand drilled countersinks and on the other hand 5 mm sphere fiducials. They were placed on each side of the TNE device at a distance of 40 mm below the measurement plane. The phantom was scanned in a MSCT unit and coordinates of the fiducial points were defined in the image space using a medical image processing software (*VUPlanner 1.06*, University of Nashville). Figure 4.7(a) depicts a screenshot of the software, showing a 5 mm sphere fiducial.

To provide a reference structure for the identification of target coordinates, four holes with a diameter of 1 mm were drilled into the measurement plane in a grid of $20 \times 20$ mm using a high precision CNC milling machine. These holes served as a calibration grid and were used to define a local coordinate frame $CF_{\mathrm{Plane}}$ for the measurement device. They were filled with colored plasticine so that the location of $CF_{\mathrm{Plane}}$ could be identified in CT images as well as in the images of the camera (see Figure 4.7(b)).

A software was developed which receives image data from the camera and calculates the TNE by determining the center of the laser dot in relation to the calibration grid. The values of the lateral TNE were stored to disc so that they could be used for the subsequent analysis. With the given setup, the following sources of errors were reproduced by the chosen experimental setup:

- Errors due to limitations in CT image quality.

- Registration errors in context with the given fiducials.

- Insufficient calibration of the pointing device and the laser pointer.

- Inaccurate pose estimation of reflective marker frames by the localizer.
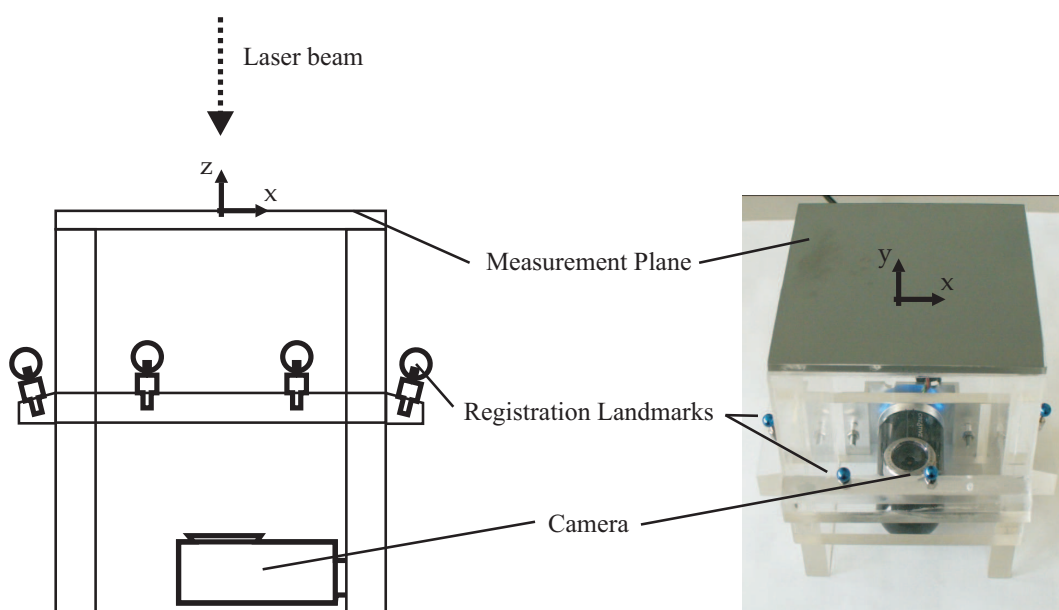
**Figure 4.6:** Design of the TNE measurement device II. Note that the reference adapter for an optical localization of the device is not shown in this picture.

- Limited spatial control of the robot's end effector.

Errors due to drilling forces are not included in the determined TNE, since no milling tool was used during these experiments.

### 4.3.2 Results

Two series of TNE measurements were taken into consideration in order to evaluate the effect of the amount of landmarks as well as the repeatability of the experimental setup.

**Accuracy Due to the Amount of Landmarks**

The TNE device was located at six different positions within the measurement volume of the localizer and different amounts of fiducials were used for registration. The origin of the coordinate frame $CF_{\text{Plane}}$ of the measurement plane was chosen to be the target point for each experiment. The laser pointer was positioned by the robot at a distance of 200 mm above the measurement plane while the laser beam was orientated towards the target coordinates. The lateral TNE was measured by the image processing software. Table 4.2 summarizes the measured deviations of the laser dot. While the lateral TNE was $0.286 \pm 0.124$ mm for a registration with seven sphere fiducials, it increased to $0.368 \pm 0.131$ mm when only four sphere fiducials were used. This corresponds with the statement that the use of more fiducials for registration usually increases the accuracy. When looking at the FRE, a larger value can be observed for seven fiducials (FRE=0.188 mm) than for
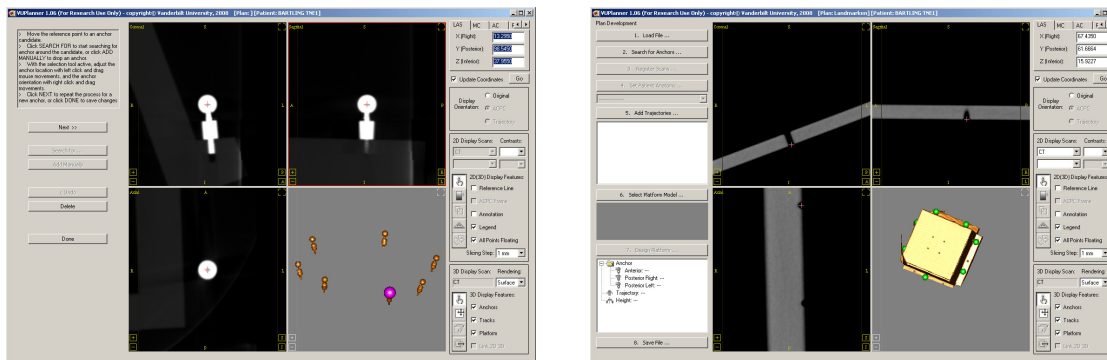
(a) Fiducial points for registration.

(b) Calibration points for the coordinate system of the measurement plane.

**Figure 4.7:** Definition of registration and calibration points (software: *VUPlanner 1.06*, University of Nashville)

four fiducials (FRE=0.177 mm). This observation emphasizes the statement that the FRE is not an appropriate value for an assessment of the navigation accuracy.

**Table 4.2:** Lateral TNE [*mm*] of the preliminary accuracy tests at a distance of 200 mm using a number of seven and four fiducial points for registration

| Position | Lateral TNE [mm] using seven registration landmarks | Lateral TNE [mm] using four registration landmarks |
|---|---|---|
| 1 | 0.061 | 0.137 |
| 2 | 0.247 | 0.328 |
| 3 | 0.296 | 0.424 |
| 4 | 0.353 | 0.398 |
| 5 | 0.412 | 0.530 |
| 6 | 0.349 | 0.389 |
| Average | $0.286 \pm 0.124$ | $0.368 \pm 0.131$ |
| FRE | 0.188 | 0.177 |

**Repeatability**

Experiments were performed to evaluate the repeatability of the mCIS setup. They included that the laser pointer was moved by the robot to the target point based on image guidance. The TNE was measured and this step was repeated several times without changing the registration transformation and the location of phantom II. The standard deviation of the TNE results was calculated before the TNE device was moved to another location.

Table 4.3 summarizes the results of 10 different locations of the TNE device and a various number of repetitions. The mean TNE of all 10 locations of the measurement device was 0.39 mm with a standard deviation of 0.19 mm. It has to be noted that countersinks were used as fiducial points

for the registration in this series of experiments. They are the reason for the higher value of the TNE compared to the results of the previously described experiments.

**Table 4.3:** Lateral TNE [*mm*] of the preliminary accuracy tests at a distance of 100 mm [EBO$^{+}$09]

| Position | Repetitions | Lateral TNE [mm] | Standard deviation |
|----------|-------------|------------------|--------------------|
| 1 | 4 | 0.09 | 0.035 |
| 2 | 4 | 0.26 | 0.034 |
| 3 | 6 | 0.36 | 0.024 |
| 4 | 6 | 0.62 | 0.030 |
| 5 | 5 | 0.60 | 0.036 |
| 6 | 4 | 0.45 | 0.041 |
| 7 | 6 | 0.43 | 0.032 |
| 8 | 8 | 0.63 | 0.038 |
| 9 | 6 | 0.13 | 0.015 |
| 10 | 5 | 0.37 | 0.023 |
| Average | | $0.39 \pm 0.19$ | 0.031 |

The repeatability of the experimental setup was calculated by the standard deviation of the measured TNEs at one location. It varied between 0.015 mm and 0.041 mm with an average value of 0.031 mm. This value lies the range of the robot's positioning capability $\Delta_R$ and thus indicates that the influence of the localizer's measurement noise during the experiment was significantly decreased by the control architecture. These experiments also show that the remaining reasons for the existence of a TNE can be found in calibration and registration errors of the IGS components. Table 4.4 summarizes the result of the laser based accuracy experiments on the basis of a statistical analysis. The mean and standard deviation of the error was $0.077 \pm 0.277$ mm in $x$ and $0.237 \pm 0.214$ mm in $y$ direction. Adding the mean error to a 99.9% confidence value for the error in its largest direction, a maximum error is given by 1.161 mm for the TNE of the laser. The results are depicted in Figure 4.8.

**Table 4.4:** Lateral TNE [*mm*] of the preliminary accuracy tests using a laser pointer

| Mean value [mm] | | Standard deviation [mm] | | | | 99.9% confidence region [mm] | Mean (norm) + confidence region |
|---|---|---|---|---|---|---|---|
| $\overline{\Delta x}$ | $\overline{\Delta y}$ | $\sigma_{\Delta x}$ | $\Delta y$ | $\sigma_{\text{Major axis}}$ | $\sigma_{\text{Minor axis}}$ | Major axis | Major axis [mm] |
| 0.077 | 0.237 | 0.277 | 0.214 | 0.279 | 0.211 | 0.918 | 1.161 |

## 4.4 Conclusions

The two performed series of experiments showed similar results for the lateral TNE. For the experiments on phantom I, the proposed 99.9% confidence region was $\leq 1.167$ mm, whereas measurements performed with a laser pointer on phantom II resulted in a 99.9% confidence region of $\leq 1.161$ mm. In addition to that, a high repeatability was observed for the given experimental setup.
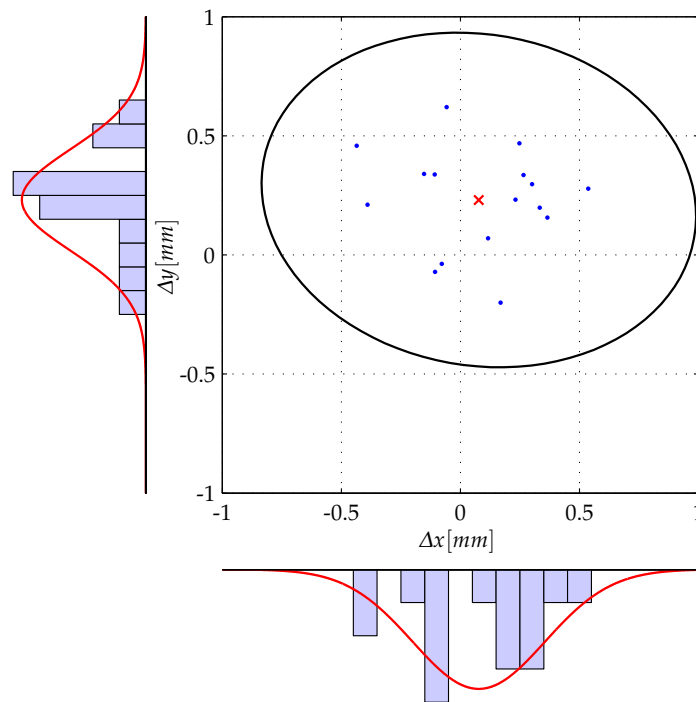
**Figure 4.8:** Determined deviations of the laser dot and results of the statistical analysis including a 99.9% confidence region

The given experimental results of the TNE correspond to the theoretically proposed TNE, which was determined in Chapter 3 to 1.158 mm for a 99.9% confidence boundary. Table 4.5 gives an overview of the results of the TNE estimations.

**Table 4.5:** Summary of accuracy measurements

| Method | Mean | Standard deviation | 99.9% confidence boundary |
|---|---|---|---|
| Theoretical | 0 mm | 0.352 mm | 1.158 mm |
| Exp. Drill | 0.156 mm | 0.307 mm | 1.167 mm |
| Exp. Laser | 0.288 mm | 0.279 mm | 1.161 mm |

The following conclusions can be drawn from these results:

- The chosen control architecture allows a precise guidance of the instrument by the robot according to the desired path.

- Since only lateral *TNEs* were acquired by the experimental setup, the TNE for a three dimensional case must be expected to be even larger. Nevertheless, as drilling is performed into the hollow structure of the cochlea, errors in the direction of the drill are less important. The measured value represents the relevant error of the mCIS drilling process.

- The main reasons for *TNEs* can be found in the imaging of the target, the calibration and registration process, as well as the arrangement of reference adapters in the measurement volume of the localizer.

Further conclusions can be drawn from these results. In particular the size of the expected TNE requires that planning of an mCIS approach needs to be very accurate in order to establish sufficient safety margins in the limited space of the temporal bone. The following chapter will present an automatic method to calculate mCIS drill paths on the basis of CT images, while safety margins between the outer wall of the drill channel and important anatomic structures are maximized. The path planning was performed on a series of temporal bone specimens and the correspondent mCIS canals were drilled by the IGS guided robot. The results of these experiments are described in chapter 6.

# 5 Optimization of mCIS Drill Path Coordinates

Numerous aspects have to be considered when defining coordinates of an mCIS. The planning of a safe access to the cochlea is complicated by the fact that the available space for the intended drill canal is substantially restricted by valuable anatomic structures that have to be preserved. The drill canal has to pass these structures at a very low distance due to the spatial arrangement of these structures. Due to the fact that the drilling process is not perfectly accurate, sufficient safety margins have also to be maintained in order to protect structures. Hence, coordinates of an optimal drill path have to be determined with exceptional care, which is a highly difficult task and states a source of risk for the patient's safety, when performed manually (cp. Section 3.3.4).

This chapter provides a method for the optimization of coordinates for a drill path that runs from the surface of the skull to the basal turn of the cochlea. The optimization includes safety margins that are maximized with respect to the medical relevance of nearby anatomic structures. In addition to that, further aspects of modern insertion strategies in terms of geometrical constraints are considered during the optimization. Section 5.1 gives an overview of these constraints and defines individual priorities for the adjacent anatomic structures. These are used to define an optimization criterion for the planning process. A software was developed in order to implement the optimization of the drill path coordinates, so that the given optimization criterion is maximized. The structure of the software as well as relevant optimization steps are described in Section 5.2. Section 5.3 finally presents obtained results of mCIS drill path calculations.

## 5.1 Criteria of mCIS Insertion Strategies

The most important aspect of the planning process is to find a suitable drill path, which provides sufficient safety margins to nearby structures. Inaccuracies of the drilling process were investigated in Chapters 3 and 4 and a TNE of more than 1.1 mm was propagated based on a worst case analysis and a statistical 99.9% confidence region. Considering this range of possible deviations as a safety margin for all anatomic structures of the temporal bone drastically restricts the available space to find a safe drill path towards the cochlea. The following example emphasizes this aspect: the facial recess provides a space of $2.5 - 3.5$ mm for the drill canal. Applying a safety margin of 1.1 mm to the facial nerve and the chorda tympani yields a space of $0.3 - 1.3$ mm which remains for the insertion of the implant. But the use of an insertion tool, which advances a cochlear implant of 0.8 mm through the drilled canal requires more space. In fact, the first research prototype of an insertion tool was designed with a diameter of 2.3 mm [HRE$^+$08, HRO$^+$09].

Besides the implementation of sufficient safety margins, a further difficulty arises from the requirements of improved insertion strategies such as combined electrical and acoustic stimulation (EAS). For EAS, the knowledge of the drill canal's spatial orientation in relation to the cochlea

is important [RHL$^+$07, RHL$^+$09]. However, this would require a geometrical description of the cochlea, which is why it is traditionally not available and thus not taken into account by surgeons. To face these challenges, the automatic path planning of an mCIS implements the following two approaches:

- *Individual safety margins*: Since anatomic structures do not have the same priority of preservation, their subjective medical relevance is used to adjust safety margins. For example, a violation of the chorda tympani nerve is accepted in exceptional cases to ensure a minimum safety level for the facial nerve. This has the effect that the safety margin of the facial nerve needs to be larger in order to optimize the position of the drill canal. Figure 5.1 illustrates this approach.

- *Calculation of the insertion angel $\psi_I$*: A three dimensional mathematical description of the electrode carrier in its desired end pose is used to calculate the insertion angel $\psi_I$ of the drill path. A maximum allowable insertion angle is integrated into the optimization process as a constraint in order to ensure a preferably tangential opening of the cochlea.



(a) Equal safety margins were chosen for each structure. The remaining space is not sufficient for a valid mCIS drill canal.

(b) A smaller safety margin was chosen for the chorda tympani nerve. A valid mCIS path can be determined.
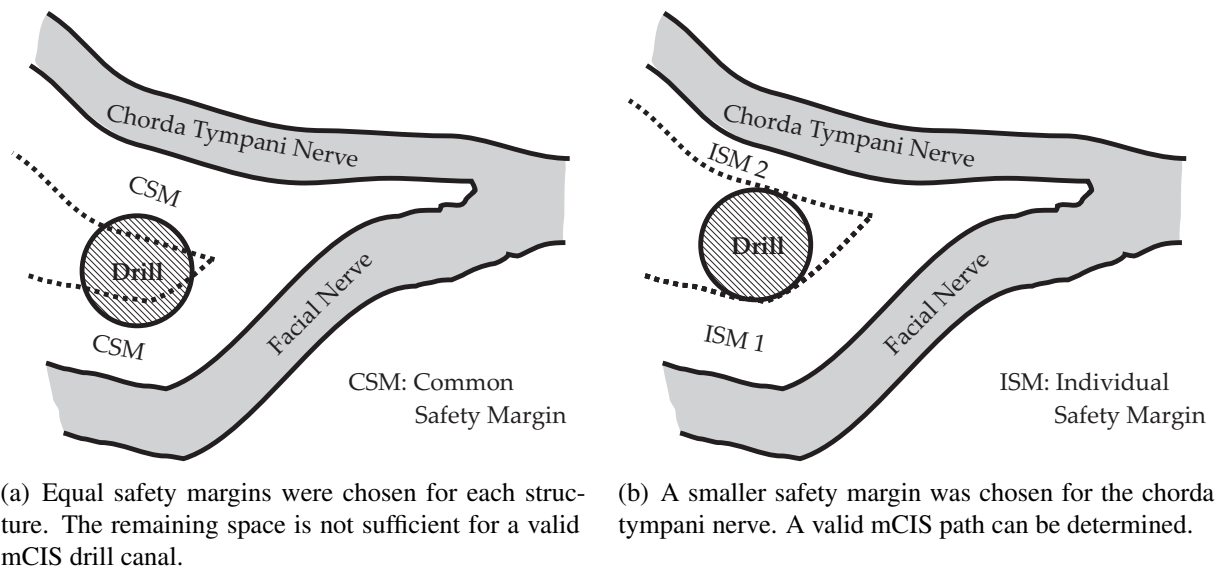
**Figure 5.1:** Relevance of individual safety margins for the mCIS planning process

### 5.1.1 Individual Preservation Priorities of Temporal Bone Structures

The relevant anatomic structures, which are located in direct proximity to the mCIS drill path include the facial nerve, the chorda tympani nerve, the ossicles, and the auditory canal. Their preservation priority can be chosen due to their subjective medical relevance as well as in the context of the insertion strategy. The facial nerve, for example, needs to be rated with the highest priority since it includes the control of the facial expression, which is why it is the most delicate of

these structures (cp. Section 1.2.3). The second highest preservation priority has to be provided for the auditory canal. It is important to keep it undamaged to avoid a breech in sterility, which could yield to future infections. The ossicles play an important role in the context of EAS strategies and therefore need to preserved. However, their medical relevance is less compared to the facial nerve and the auditory canal. The chorda tympani nerve is a structure with a lower priority compared to the others. A violation of the chorda tympani nerve would lead to a limitation of the taste sense. A sacrifice is accepted by surgeons during a posterior tympanotomy in case of a narrow facial recess in order to ensure the safety of the facial nerve.

In order to provide a quantitative value for these properties, intended probabilities for a preservation were defined for each structure. They are given in Table 5.1 while the temporal bone structures are sorted in order of their priority.

**Table 5.1:** Priority and intended preservation probabilities of temporal bone structures

| Structure | Priority | Preservation probability |
|---|---|---|
| Facial nerve | Very high | 99.9% |
| Auditory canal | High | 99.0% |
| Ossicles | High | 98.0% |
| Chorda tympani nerve | Medium | 90.0% |

### 5.1.2 Model Based Description of the Electrode Carrier in its Desired End Pose

The exact spatial orientation of the drill path in relation to the basal turn of the cochlea is an important information which is used in modern insertion strategies such as atraumatic insertion [HRE$^+$08]. The most important parameter for the description of this relationship is the spatial angle $\psi_I$ between the drill path and the desired end pose of the electrode carrier within the scala tympani (see Figure 5.2). Therefore, a mathematical description of the scala tympani's curvature in the three dimensional space is required. However, this complicates a manual determination of $\psi_I$ based on two dimensional slice views of the CT image data.

An approach for this purpose is presented in [EHB$^+$07]. The scala tympani is identified based on a number of measurement points. The spatial curvature is defined as a spiral function, which is defined by the radius $r(\theta)$ and the height $h(\theta)$. They are given by

$$r(\theta) = p_1 \frac{c}{\theta + p_2}, \quad \text{with} \quad c = p_2 \frac{p_2 + \pi}{2p_2 + \pi}$$
$$h(\theta) = p_3 e^{p_4\theta} - p_3 \tag{5.1}$$

Note that $\theta$ denotes an angular variable of the spiral function whereas $p_1...p_4$ are parameters, which are used to adapt the form of the spiral to the given layout of the cochlea. Once, the spiral function is given for a cochlea, a number of additional options for the path planning procedure is available. Besides a calculation of the insertion angle $\psi_I$, it can be used to define rotational movements of the implant about its main axis during the insertion process in order to

avoid intracochlear damage.  Furthermore, it allows to compare the shape and size of cochleae from different patients.  Investigations on a series of human cochleae resulted in mean values of $p_1 = 6.6, p_2 = 1.5, p_3 = 0.7, p_4 = 0.1$ [HRO$^+$09]. However, these values also showed large standard deviations meaning that the geometrical layout of the cochlea and its major dimensions show great interindividual variability.  Therefore, an individual parametrization of the spiral function is necessary for each patient.

The spiral function can be used as a mathematical description of the intended final pose of the electrode carrier within the scala tympani after the insertion process has been completed.  This information can be incorporated to determine two important parameters: on the one hand, a set of points can be defined within the first section of the scala tympani, which mark feasible start coordinates of the insertion process. Thus, they can also be used as target points for the planning of the drill path. On the other hand, the insertion angle $\psi_I$ can be calculated. It is defined as the angle between the drill path and the tangent of the spiral at the target coordinates $\mathbf{x}_t$. Figure 5.2 illustrates the three-dimensional model of a human cochlea in semi transparent volume view together with the spiral formed pose of the electrode carrier and illustrates the insertion angle $\psi_I$.
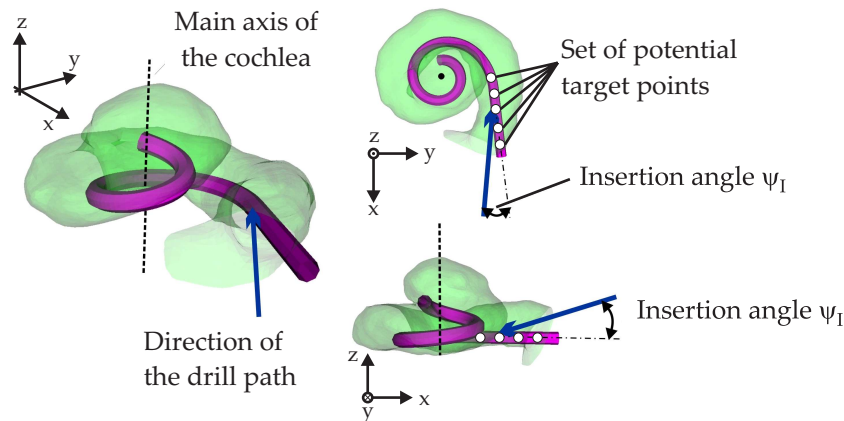


**Figure 5.2:** Three-dimensional model of a human cochlea in semi-transparent mode, including the intended final pose of the electrode carrier after completion of the insertion

## 5.2  Optimization Steps for the Calculation of mCIS Path Coordinates

Automatic path planning was implemented with a custom made software, which was written in C++ using the open source class library of VTK (Visualization Toolkit) [SML06]. VTK provides an extensive number of functions for visualization of and interaction with three dimensional data as well as a variety of algorithms that can be used for geometric calculations. The core components of the path planning software can be divided into four parts, which are described in the following.

### 5.2.1 Initial Information

The calculation of drill paths requires some initial information. It is necessary that the essential temporal bone structures are available as 3D representations from segmented CT images. They can be loaded by the software and rendered in a display window. Furthermore, a model of the electrode carrier (cp. Section 5.1.2) in its intended final pose is supposed to exist. The spiral function is used to define a number $N_t$ of potential target points $\mathbf{x}_{t,1...N_t}$ and can be displayed in the render window superimposed to the anatomic structures (see Figure 5.3(a)).

In order to reduce the amount of calculations, which have to be performed to find the optimal coordinates, a circular search space for the entry point has to be defined by the user. This is done manually while the temporal bone is visualized in a transparent mode, so that it can be examined together with its internal structures as 3D objects in the render window. The user selects a point on the rendered object via mouse interaction and defines a radius $s_e$ for the circular area. The entry point search space is used to determine a set of equally distributed entry point candidates $\mathbf{x}_{e,1...N_e}$ based on a grid spacing parameter $g_1$. It can be chosen by the user and is initially set to $g_1$=0.5 mm. Each combination of entry and target point results in a number of $N_p = N_e \cdot N_t$ potential drill paths $p_{1...N_p}$. Figure 5.3(b) illustrates the 3D temporal bone structures together with the entry point search space (green circular area) and the possible drill paths as black lines.

Before starting the optimization algorithm, the user has to confirm the following set of parameters, which are relevant for the optimization process.

- *Priority indices $k_j$ for each anatomic structure j*: The unit-less priority index varies between 1.0 *(very important)* and 0.0 *(unimportant)* and is chosen for each structure individually. The actual choice of $k_j$ is explained in Section 5.2.3.

- *Minimum safety distances $d_{j,min}$ for each anatomic structure j*: Regardless of the priority, minimum safety distances can be defined individually for each anatomic structure. A drill path will only be valid if these distances are maintained.

- *Maximum allowable insertion angle $\psi_{I,max}$*: Drill paths with an insertion angle greater than $\psi_{I,max}$ can be excluded in order to account for a rather tangential insertion of the electrode carrier.

- *Radius $r_{drill}$ of the drill burr*: For the determination of the drill canal's dimension the radius $r_{drill}$ of the drill burr is necessary.

### 5.2.2 Calculation of Distances between Drill Paths and Vital Anatomy

As a first step, an intersection test is performed for the given set of drill paths in order to exclude every path, colliding with the surface of any rated structure. After this test, the distance
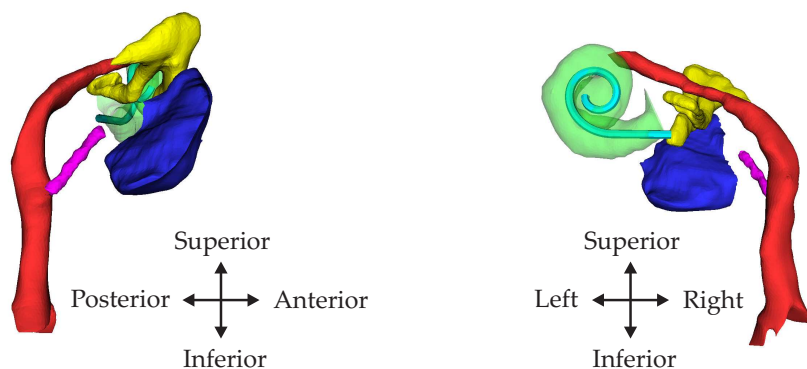
(a) Stage 1: the anatomic structures as well the spiral of the cochlea are visualized.
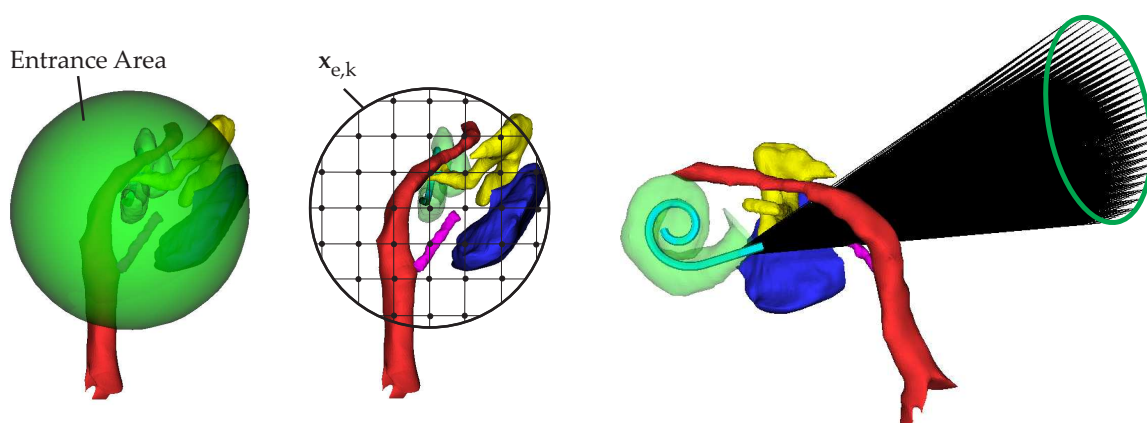


(b) Stage 2: the entrance area is chosen by the user and visualized as a green sphere (left). The entrance area is divided into a grid of possible entry points. Each investigated drill path is illustrated as a black line (right).

**Figure 5.3:** Initialization steps of the path planning procedure. Illustrated structures: cochlea (green), ossicles (yellow), auditory canal (blue), facial nerve (red), chorda tympani nerve (magenta), intended end pose of the electrode carrier (cyan).

$d\left(p_i, S_j\right)$ between each remaining drill path $p_i$ and the adjacent anatomic structures $S_j$ are determined. Therefore, the direction of $p_i$ is described using the vector

$$\mathbf{p}_i = \mathbf{x}_{\mathrm{t},j} - \mathbf{x}_{\mathrm{e},k} \quad \text{with } j = 1...N_t \text{ and } k = 1...N_e. \tag{5.2}$$

Thus, any point $\mathbf{y}$ on $p_i$ can be represented as

$$\mathbf{y} = \mathbf{x}_{\mathrm{e},k} + m\frac{\mathbf{p}_i}{\|\mathbf{p}_i\|_2}, \tag{5.3}$$

where $m$ is a scalar, which is bounded by

$$0 \leq m \leq \|\mathbf{p}_i\|_2 . \tag{5.4}$$

The anatomic structures $S_{1...j}$ are given as triangulated surfaces while each triangle is composed of a set of three vertices. For the calculation of the distance $d(p_i, S_j)$ between $p_i$ and $S_j$, the closest vertex $v_{\text{closest},j}$ of $S_j$ is determined. Although the closest point on $S_j$ can generally be any point on the triangulated surface, it is assumed that the number of vertices is large so that $S_j$ is sufficiently represented by them. $v_{\text{closest},j}$ is determined by using a function that locates the closest point on $S_j$ (see [MSL05] for detailed class reference of the implemented function). The distance $d(p_i, S_j)$ is afterwards calculated by

$$d(p_i, S_j) = \frac{\left\| (\mathbf{p}_i) \times \left( \mathbf{v}_{\text{closest},j} - \mathbf{x}_{\text{e},k} \right) \right\|_2}{\|\mathbf{p}_i\|_2} - r_{\text{drill}}, \tag{5.5}$$

while $r_{\text{drill}}$ denotes the radius of the drill.

### 5.2.3 Optimization Criterion

In order to find the optimal path, a two step scale space approach in combination with Wald's maximin rule [Wal45] is used. It is a pessimistic decision rule in order to maximize the minimum possible gain of a problem. In the context of planning a drill path with optimized distances to the adjacent structures, gain is represented by an optimization criterion $J$, which includes the weighted distance between $p_i$ and a structure $S_j$ according to its priority. It is defined by

$$J(p_i, S_j) = \frac{1}{k_j} d(p_i, S_j), \tag{5.6}$$

while $k_j$ denotes the priority index of the structure $S_j$. It is used in order to express the size of the confidence boundaries of each structure in relation to the facial nerve. This means, $k$ is set to 1.0 for the facial nerve, while the other structures are rated by the quotient $\frac{b_j}{b_{\text{FN}}}$ of its individual confidence boundary $b_j$ and the confidence boundary $b_{\text{FN}}$ of the facial nerve. Table 5.2 summarizes the priority indices of the relevant temporal bone structures.

**Table 5.2:** Priority indices of temporal bone structures

| Structure $S_j$ | Intended preservation probability | Confidence boundaries $b_j$ for a normal distribution [$\sigma$] | Priority index $k_j = \frac{b_j}{b_{\text{FN}}}$ (rounded) |
|---|---|---|---|
| Facial nerve | 99.9% | $\pm$ 3.2905 | 1.0 |
| Auditory canal | 99.0% | $\pm$ 2.5758 | 0.8 |
| Ossicles | 98.0% | $\pm$ 2.2363 | 0.7 |
| Chorda tympani nerve | 90.0% | $\pm$ 1.6449 | 0.5 |

The most qualified path $p_{\text{opt},1}$ of the first optimization stage is finally determined by using the

maximin rule in order to find the best combination of entrance and target coordinates, while the side conditions of a maximal allowable insertion angle $\psi_{\text{I,max}}$ as well as the defined minimum distances to the structures have to be fulfilled:

$$p_{\text{opt},1} := \left\{ \arg \max_{i=1...N_p} \left( \min_{j=1...N_S} \left( J\left( p_i, S_j \right) \right) \right), \quad \psi_{\text{I}}(p_i) \leq \psi_{\text{I,max}}, \quad d(p_i, S_j) \geq d_{j,\text{min}} \right\}. \quad (5.7)$$

In this equation, $N_p$ denotes the amount of investigated paths and $N_S$ describes the number of considered structures.

The minimum of the weighted distances between a path $p_i$ and the relevant structures has a maximum value for the considered set of paths. In this context, the use of weighted distances as an optimization criterion (Equation 5.6) has a simple effect. Instead of equal distances to adjacent structures, the optimal path is placed farther from structures with high priority at the expense of the distances to structures with low priority. As a consequence, the relation of the distances corresponds to the relation of the priority indices.

After the first stage, a second optimization step is performed in order to improve the entry point of the drill path. Therefore, the entry point coordinates of the resulting drill path $p_{\text{opt},1}$ are used to specify a smaller entry point search space with a higher resolution (spacing parameter $g_2$ initially set to 0.1 mm). The optimization is restarted so that an improved drill path $p_{\text{opt},2}$ is calculated, that further optimizes the safety margins.

### 5.2.4 Specification of Drilling Coordinates

The calculated target point of the final drill path $\mathbf{x}_t(p_{\text{opt},2})$ is located within the cavity of the scala tympani, because of its geometrical definition on the mathematical spiral. Hence, the drill burr can be stopped at an earlier location where the outer wall of the scala tympani is reached. In order to define a more appropriate target point for the drilling process, the intersection point $\mathbf{x}_I$ of $p_{\text{opt},2}$ and the scala tympani is determined. The final target coordinates $\mathbf{x}_t(p_{\text{opt},2})$ for the mCIS is defined at a distance of 1 mm below the surface in order to ensure that the scala tympani is opened by the drill burr. Figure 5.4 illustrates the temporal bone structures together with a model of the drill according to the optimized drill coordinates. In addition to that, a flow chart of the optimization process is depicted in Figure 5.5.

## 5.3 Results

The path planning was performed on a set of 37 segmented temporal bone specimens. Each specimen as well as its embedded anatomic structures of the facial nerve, the chorda tympani nerve, the auditory canal, as well as the ossicles were available as triangulated surface structures. The radius of the mCIS drill canal was chosen to be 0.5 mm while the radius of the entry point search space was set to 8.0 mm. As a requirement for a smooth electrode insertion, drill paths were only accepted with an insertion angle of $\psi_{\text{I,max}} = 20.0°$. Additionally, minimum distances have
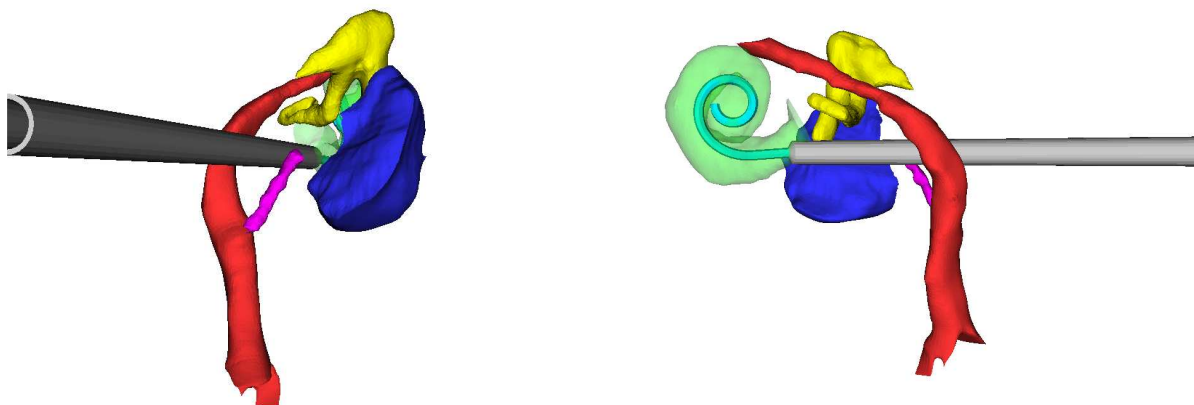
**Figure 5.4:** Path optimization stage 3. The drill is illustrated with the optimal combination of entry and target point. Structures: cochlea (green), ossicles (yellow), auditory canal (blue), facial nerve (red), chorda tympani nerve (magenta), drill (grey).

been chosen for each structure. They are summarized in Table 5.3 together with the remaining parameters of the optimization process.

**Table 5.3:** Chosen parameter set for the optimization

| Parameter | Value |
|---|---|
| Drill radius $r_{\text{drill}}$ | 0.5 mm |
| Search space radius $s_e$ | 8 mm |
| Maximum insertion angle $\psi_{\text{I,max}}$ | 20.0° |
| Minimum distance to facial nerve $d_{\text{fn,min}}$ | 1.16 mm |
| Minimum distance to chorda tympani nerve $d_{\text{ct,min}}$ | 0.55 mm |
| Minimum distance to ossicles $d_{\text{os,min}}$ | 0.77 mm |
| Minimum distance to auditory canal $d_{\text{ac,min}}$ | 0.88 mm |

Figure 5.6 illustrates the distribution of the optimization criterion $\min_{j=1...N_S} \left( J\left(p_i, S_j\right) \right)$ in the entry point search space for an exemplary temporal bone specimen. The result for each path is plotted according to its entry point in the circular search space. It can be seen, that the optimization criterion has a maximum in the area, which is bounded by the facial nerve, the chorda tympani nerve, the ossicles and the auditory nerve at different levels of the insertion depth. The drill path, which is determined by the optimization algorithm to maximize the minimum distance, is generally located in this area. This also corresponds to the area, where a surgeon would manually place the drill path.

The results of the automated path planning are summarized in Table 5.4. In this table bold numbers are used to indicate that the minimum distance criterion failed for at least one of the rated structures. Besides distances to the anatomic structures, Table 5.4 also provides the insertion angle $\psi_I$, the two structures with the smallest weighted distance to the drill canal as well as the factor $\alpha$ indicating the ratio between the safety distances (cp. Section 3.3.4) and its desired value.
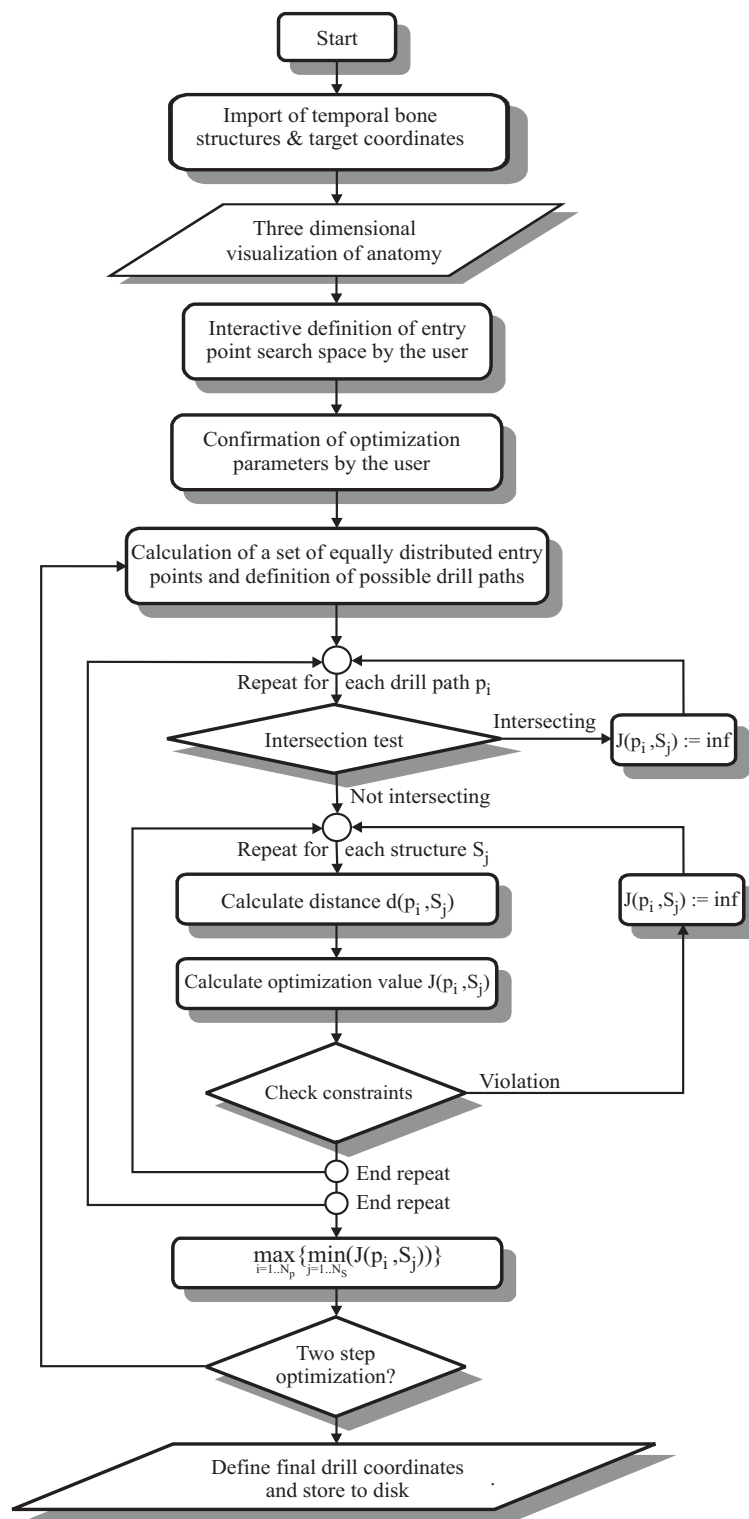
**Figure 5.5:** Flow chart of the optimization process
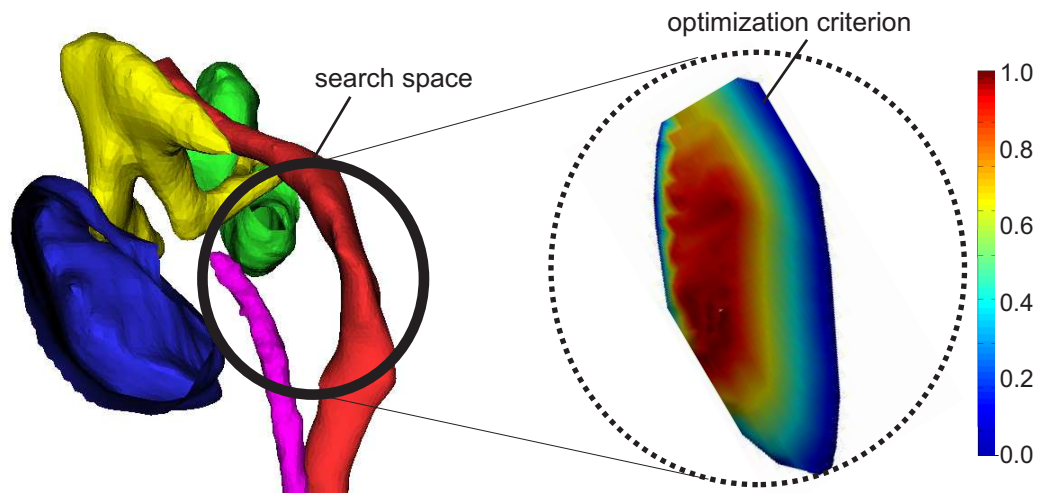
**Figure 5.6:** Location of the entry point search space and corresponding plot of the optimization criterion for each investigated path according to its entry point within the search space

The results of the planning trials can be summarized as follows:

- The mean distance between the drill canal's wall and the adjacent structures is $1.05 \pm 0.27$ mm for the facial nerve, $0.66 \pm 0.26$ mm for the chorda tympani nerve, $1.36 \pm 0.58$ mm for the auditory canal and $0.85 \pm 0.21$ mm for the ossicles.

- The mean insertion angle is $16.1 \pm 3.1$ °.

- For each calculated drill canal, $\alpha$ is very close to the intended relation of the limiting structure's priorities (this value is given in brackets). In one case (TB26), a larger deviation of $\alpha$ from its desired value can be observed. The reason is, that the maximum insertion angle was reached, so that a further optimization of the drill path location was not possible.

- The position of the drill path is mostly limited by the facial nerve and the chorda tympani nerve. This is the case for 26 temporal bones (70.3 %).

- In 14 out of 37 temporal bone specimens (37.8 %), a path could be determined which meets all the given side conditions.

In 62.2% of the cases, drill canals could not be planned with sufficient safety margins as defined in Table 5.3. Hence, an mCIS might not be recommended for these patients. Additionally, it has to be noted that the drill canal was planned with a diameter of 1.0 mm, which states a high demand on the miniaturization of the insertion process through this canal. In order to maintain larger diameters for the drill canal while the minimum preservation rates keep the same, the drilling process needs to be more accurate so that the TNE is reduced.

Nevertheless, all generated drill canals appear to be reasonable at visual inspection. The results suggest that the optimization software is effective and robust for this application. In addition to that, planning parameters can be easily adjusted to a different setup of the IGS system.

**Table 5.4:** Distances between the outer wall of determined mCIS drill canals and the facial nerve respectively the chorda tympani nerve. Bold numbers indicate that the distance failed to meet the minimum distance criterion. Abbreviations: fn - facial nerve; ct - chorda tympani nerve; ac - auditory canal; os - ossicles.

| Temporal bone | Requirements met (yes/no) | Distance $d_{fn}$ [mm] to facial nerve | Distance $d_{ct}$ [mm] to chorda tympani nerve | Distance $d_{ac}$ [mm] to auditory canal | Distance $d_{os}$ [mm] to ossicles | Limiting structures | Relation $\alpha$[−] of limited structures (desired value) | Insertion angle $\psi_I$ |
|---|---|---|---|---|---|---|---|---|
| TB01 | no | **1.04** | 0.70 | **0.80** | **0.72** | fn - os | 1.44 (1.43) | 19.27 |
| TB02 | no | **1.13** | 1.36 | **0.88** | **0.76** | ac - os | 1.16 (1.14) | 19.88 |
| TB03 | yes | 1.30 | 1.31 | 1.03 | 0.98 | fn - ac | 1.26 (1.25) | 19.13 |
| TB04 | no | **0.68** | **0.36** | **0.65** | **0.48** | fn - os | 1.42 (1.43) | 7.38 |
| TB05 | no | **0.98** | **0.50** | 1.22 | **0.76** | fn - ct | 1.96 (2.00) | 11.15 |
| TB06 | yes | 1.42 | 0.72 | 1.15 | 0.98 | fn - os | 1.45 (1.43) | 15.88 |
| TB07 | no | **0.58** | 0.68 | **0.47** | 0.81 | fn - ac | 1.23 (1.25) | 11.84 |
| TB08 | no | **0.88** | 0.59 | **0.70** | **0.62** | fn - ac | 1.26 (1.25) | 14.48 |
| TB09 | no | **1.02** | **0.57** | **0.86** | **0.71** | fn - os | 1.44 (1.43) | 16.17 |
| TB10 | no | **0.87** | **0.43** | **0.68** | 1.43 | fn - ct | 2.02 (2.00) | 19.31 |
| TB11 | yes | 1.18 | 0.59 | 0.94 | 1.04 | fn - ct | 2.00 (2.00) | 12.60 |
| TB12 | no | **0.57** | **0.29** | **0.59** | **0.42** | fn - ct | 1.97 (2.00) | 15.84 |
| TB13 | no | **0.73** | **0.38** | 1.48 | **0.52** | fn - os | 1.40 (1.43) | 18.50 |
| TB14 | no | **1.04** | 0.63 | **0.81** | **0.75** | fn - ac | 1.28 (1.25) | 19.44 |
| TB15 | no | **0.97** | **0.49** | 1.12 | 0.82 | fn - ct | 1.98 (2.00) | 18.10 |
| TB16 | yes | 1.23 | 0.61 | 1.74 | 0.88 | fn - ct | 2.02 (2.00) | 12.49 |
| TB17 | no | **0.88** | **0.44** | 1.61 | **0.61** | fn - ct | 2.00 (2.00) | 10.14 |
| TB18 | no | **1.05** | **0.55** | **0.82** | 1.09 | fn - ac | 1.28 (1.25) | 19.11 |
| TB19 | no | **1.10** | **0.55** | 0.98 | 0.78 | fn - ct | 2.00 (2.00) | 14.89 |
| TB20 | no | **0.94** | **0.47** | 0.91 | 0.90 | fn - ct | 2.00 (2.00) | 14.40 |
| TB21 | no | **0.83** | **0.41** | 1.11 | **0.74** | fn - ct | 2.02 (2.00) | 14.88 |
| TB22 | no | **0.46** | **0.23** | 1.90 | **0.76** | fn - ct | 2.00 (2.00) | 18.52 |
| TB23 | no | **0.95** | **0.48** | 0.91 | 0.93 | fn - ct | 1.98 (2.00) | 15.62 |
| TB24 | yes | 1.23 | 0.61 | 1.79 | 0.86 | fn - ct | 2.02 (2.00) | 14.29 |
| TB25 | no | 1.17 | **0.56** | 1.44 | 0.81 | fn - os | 1.44 (1.43) | 17.53 |
| TB26 | yes | 1.16 | 0.66 | 1.59 | 0.96 | fn - ct | **1.76** (2.00) | 19.92 |
| TB27 | no | **0.92** | **0.48** | 1.46 | 0.99 | fn - ct | 1.92 (2.00) | 19.17 |
| TB28 | yes | 1.49 | 0.75 | 1.75 | 1.39 | fn - ct | 1.99 (2.00) | 15.03 |
| TB29 | yes | 1.46 | 0.73 | 2.40 | 1.01 | fn - ct | 2.00 (2.00) | 15.10 |
| TB30 | no | **1.02** | **0.51** | 2.50 | 0.81 | fn - ct | 2.00 (2.00) | 17.12 |
| TB31 | yes | 1.34 | 0.67 | 2.43 | 0.94 | fn - ct | 2.00 (2.00) | 18.11 |
| TB32 | yes | 1.39 | 0.68 | 2.14 | 0.96 | os - ct | 1.41 (1.40) | 19.25 |
| TB33 | yes | 1.29 | 0.64 | 1.60 | 0.93 | fn - ct | 2.02 (2.00) | 17.89 |
| TB34 | yes | 1.17 | 0.58 | 2.23 | 0.82 | fn - ct | 2.02 (2.00) | 16.24 |
| TB35 | yes | 1.42 | 0.71 | 1.77 | 1.00 | fn - ct | 2.00 (2.00) | 19.37 |
| TB36 | yes | 1.38 | 0.87 | 1.88 | 0.95 | fn - os | 1.45 (1.43) | 19.95 |
| TB37 | no | **0.72** | **0.36** | 2.12 | **0.50** | fn - ct | 2.00 (2.00) | 14.94 |
| | | $1.05 \pm 0.27$ | $0.60 \pm 0.23$ | $1.36 \pm 0.58$ | $0.85 \pm 0.21$ | | | $16.3 \pm 3.1$ |

# 6 Experimental Studies on Temporal Bone Specimens

The expected inaccuracies of the mCIS approach have been evaluated in Chapters 3 and 4 based on an error model as well as on preliminary TNE studies. However, the results of these investigations can only be used as an indicator of the expected accuracy in a real setup. In order to assess the feasibility of this approach, it is crucial that the accuracy is also investigated in a setup which particularly includes the use of preferably human temporal bone specimens. mCIS experiments were therefore conducted on an number of cadaveric specimens. For reasons of practicability, a drill with a conical diameter ranging from 1.3 mm to 1.8 mm was used instead of a drill with 1.0 mm as proposed in Chapter 5. After the experiments, the drilled canals were analyzed for each temporal bone on the basis of post-experimental CT images.

The performed experiments can be divided into three studies according to the choice of segmentation techniques and types of fiducial landmarks:

- *Experimental study 1:* Manual segmentation + screw fiducials; experiments performed on 10 temporal bones

- *Experimental study 2:* Automatic segmentation + screw fiducials; experiments performed on 6 temporal bones

- *Experimental study 3:* Combination of manual and automatic segmentation + sphere fiducials; experiments performed on 10 temporal bones

This chapter presents the results of these studies. In Section 6.1, pre-experimentally performed steps of the mCIS experiments are described. They include the preparation of the temporal bone specimens, the image acquisition, and the planning of the mCIS coordinates. The registration results as well as controller deviations measured in the intra-experimental stage of the experiments are presented in the subsequent Section 6.2. Furthermore, the outcome of the experiments is analyzed in Section 6.3 in two ways: on the one hand, post-experimental CT image data is inspected in order to detect any violation of important anatomical structures as well as to evaluate the location of the cochleostomy. On the other hand, a registration of these images with the planning data is performed. Thus, deviations of the drill canal in relation to its intended location can be calculated. Section 6.4 finally concludes this chapter with a discussion of the experimental results.

## 6.1 Pre-Experimental Steps

Pre-experimental steps were necessary, before the robot assisted drilling experiments could be performed on the temporal bone specimens. They are described in the following.

### 6.1.1 Preparation of Temporal Bone Specimens

A total of 26 temporal bone specimens from human body donors were used for the experimental studies. In a first step, soft tissue was removed from each specimen, followed by an implantation of five to six registration markers to the outer surface of the mastoid. Figure 6.1 shows a picture of a temporal bone specimen containing five sphere fiducials.
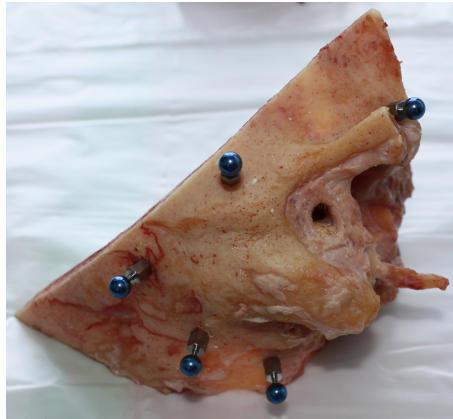


**Figure 6.1:** Temporal bone specimen with five sphere fiducials

Two types of fiducials were used for the experiments. For the first two studies, M1.4 cross head screws were taken, whereas sphere fiducials as described in Section 3.5 were used in the last study. The fiducials were placed around the assumed entry point of the drill in order to minimize the registration error. In addition to that, a plaster bed with a cast of the specimen was prepared for each temporal bone. It was used as a base frame for a stable fixation of the specimen, which is necessary to prevent any dislocation under the intra-experimentally applied drilling loads.

### 6.1.2 Imaging and Segmentation

In the second step, images were acquired for each temporal bone using a VCT unit. A set of slice images was reconstructed in each case and exported to the DICOM format with a size of $512 \times 512$ pixels per image. The resolution of the image data set varied according to the size of the specimen between $(0.129 \times 0.129 \times 0.129)$ mm$^3$ and $(0.250 \times 0.250 \times 0.250)$ mm$^3$. The shapes of the following structures were segmented in the image data: cochlea, facial nerve, chorda tympani nerve, ossicles, auditory canal, and fiducial points. Different segmentation techniques were used for this purpose:

**Segmentation Technique in Study 1**

For the first study, the segmentation of the anatomic structures was done manually with the help of the surgical planning software *iPlan 2.6 (BrainLAB AG, Feldkirchen, Germany)*. The resulting

anatomic structures were exported to 3D data objects in STL format via the VVLink Interface of the software.

**Segmentation Technique in Study 2**

For the second study, automatic segmentation methods as presented by NOBLE ET. AL. [NDWL09] were used (cp. Section 3.3.3). Within less than 10 minutes, the planning software generated 3D data objects of the temporal bone structures that were used for the subsequent planning process.

**Segmentation Technique in Study 3**

Automatic segmentation methods were also applied to the data sets of the third study. However, it was found that the results were not satisfying. A comparison of the exported 3D structures with corresponding manual segmentation results showed significant deviations of the surface structure. This was particularly observed in the case of the facial nerve and the chorda tympani nerve. An analysis of these structures, according to the methodology presented in Section 3.3.2, showed Hausdorff distances ranging from 0.7 mm to 1.5 mm for the facial nerve. This is exemplarily depicted in Figure 6.2. It shows an automatic segmentation result of a facial nerve, which is colored according to its surface distance to the corresponding manual segmentation result (shown in transparent grey). Regarding the manual segmentation as a gold standard, the automatic generated facial nerve was segmented with errors. The surface differs from the manual segmentation result with deviations of up to 1.5 mm.
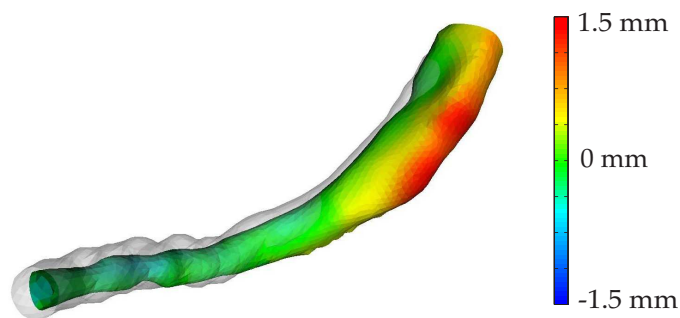


**Figure 6.2:** Surface distances between results of manual and auto-segmentation result of the facial nerve

As a consequence, automatic and manual segmentation results were combined in the experiments of study 3. For the facial nerve and the chorda tympani nerve, manual segmentation results were chosen whereas automatic segmentation results were used to represent the remaining structures.

### 6.1.3 Planning of the mCIS

The coordinates of the mCIS drill canals were defined using the developed planning software, described in Chapter 5. The priority indices of the given structures were chosen according to Table 5.2 and the insertion angle was restricted to a maximum value of $20°$. A conical drilling tool (Lindemann burr NS1808.036, KOMET MEDICAL, Lemgo, Germany) with a diameter ranging from 1.3 mm to 1.8 mm was used for the experiments. Therefore, the software parameter of the drill radius was adapted according to the size of the resulting drill hole that the tool creates at the most sensitive location, i.e. the facial recess. It was determined by the radius of the drill shaft at a distance of 8 mm above the tool tip. This distance corresponds to the mean distance between the cochleostomy point and the plane of the facial recess. The diameter was measured at this point to 1.5 mm.

The results of the planning process in terms of remaining safety margins between the drill canal and the surrounding anatomic structures are summarized for all three studies in Table 6.1. It has to be noted that the safety margins are smaller compared to the results of Chapter 5. This is due to the fact that the drill diameter for the planning process increased from 1.0 mm to 1.5 mm. The distance to the facial nerve ranges from 0.323 mm (EXP1-8) to 1.36 mm (EXP2-4). Furthermore, a violation of the chorda tympani nerve was intentionally accepted in two cases (EXP1-7 and EXP2-4) in order to maintain a minimum distance to the facial nerve.

## 6.2 Intra-experimental Stage

The specimens were fixed to a custom made temporal bone holder by using the prepared plaster bed in combination with a mechanical clamping device. A reference adapter was attached to the temporal bone holder to measure the location of the specimen with the optical localizer unit. The temporal bone holder allowed a change of the new specimen without the need of attaching a new reference adapter directly to the specimen. Apart from the target object, the remaining components of the experimental setup (KUKA KR3 robot, control computer, localizer) were the same as described in the TNE studies (see Section 4.1). After the registration of the temporal bone, the tool was driven with a rotational speed of $10,000$ rpm while the robot's movement along the drill path was controlled by the IGS system. Furthermore, the feed rate of the drilling process was set manually using an input device that was connected to the control unit computer. The fixation and registration of each specimen required approximately 20 minutes, whereas drilling was performed within 5 minutes. Figure 6.3 illustrates the setup and shows a picture of the drilling phase.

### 6.2.1 Intraoperative Registration Results

Before drilling could be started, a registration of the specimen's location in the physical space and the image space of the corresponding planning data was performed. A pointing device was used to measure the fiducial points inside the measurement volume of the localizer. The registration was

**Table 6.1:** Distances between the outer wall of the calculated mCIS drill canal and the segmented anatomic structures

| Temporal bone | Distance $d_{fn}$ [mm] to facial nerve | Distance $d_{ct}$ [mm] to chorda tympani nerve | Distance $d_{ac}$ [mm] to auditory canal | Distance $d_{os}$ [mm] to ossicles |
|---|---|---|---|---|
| EXP1-1 | 0.839 | 0.153 | 0.465 | 0.940 |
| EXP1-2 | 0.660 | 0.303 | 0.961 | 0.305 |
| EXP1-3 | 0.692 | 0.310 | 0.929 | 0.278 |
| EXP1-4 | 0.391 | 0.303 | 1.439 | 1.271 |
| EXP1-5 | 0.742 | 0.316 | 1.029 | 0.826 |
| EXP1-6 | 0.807 | 0.262 | 0.537 | 0.352 |
| EXP1-7 | 0.346 | violation | 1.031 | 0.251 |
| EXP1-8 | 0.323 | 0.200 | 1.576 | 0.586 |
| EXP1-9 | 0.449 | 0.309 | 1.340 | 0.598 |
| EXP1-10 | 0.816 | 0.419 | 0.529 | 0.355 |
| Mean + SD | $0.61 \pm 0.21$ | $0.25 \pm 0.13$ | $0.98 \pm 0.39$ | $0.58 \pm 0.34$ |
| EXP2-1 | 0.911 | 0.408 | 1.501 | 0.680 |
| EXP2-2 | 0.531 | 0.021 | 1.148 | 0.502 |
| EXP2-3 | 0.615 | 0.407 | 1.793 | 0.607 |
| EXP2-4 | 1.360 | violation | 0.947 | 1.598 |
| EXP2-5 | 0.510 | 0.403 | 1.522 | 0.443 |
| EXP2-6 | 0.804 | 0.308 | 1.006 | 0.623 |
| Mean + SD | $0.84 \pm 0.33$ | $0.38 \pm 0.05$ | $1.35 \pm 0.36$ | $0.79 \pm 0.46$ |
| EXP3-1 | 0.877 | 0.500 | 1.650 | 0.674 |
| EXP3-2 | 0.726 | 0.428 | 1.696 | 0.574 |
| EXP3-3 | 0.833 | 0.478 | 1.436 | 0.700 |
| EXP3-4 | 1.148 | 0.604 | 1.654 | 0.872 |
| EXP3-5 | 1.093 | 0.581 | 2.247 | 0.755 |
| EXP3-6 | 0.982 | 0.558 | 2.274 | 0.688 |
| EXP3-7 | 1.014 | 0.578 | 2.022 | 0.702 |
| EXP3-8 | 0.880 | 0.500 | 1.331 | 0.673 |
| EXP3-9 | 1.072 | 0.569 | 1.613 | 0.726 |
| EXP3-10 | 1.106 | 0.589 | 1.625 | 0.763 |
| Mean + SD | $0.97 \pm 0.14$ | $0.54 \pm 0.06$ | $1.75 \pm 0.32$ | $0.71 \pm 0.08$ |

performed with the standard algorithm based on singular value decomposition (see Section 2.4.3). The result of the registration step was verified for safety reasons by commanding the robot to guide a laser pointer to one of the fiducial landmarks. Figure 6.4 illustrates this step.

The *FREs* of the intra-operative registration are summarized in Table 6.2. In case of the first two studies, where screw fiducials were used as landmarks, an almost identical mean value of FRE $\approx 0.18$ mm was observed. In study 3, a lower mean FRE value of 0.162 mm was observed.

(a) Experimental setup.                         (b) Picture of the drilling process.
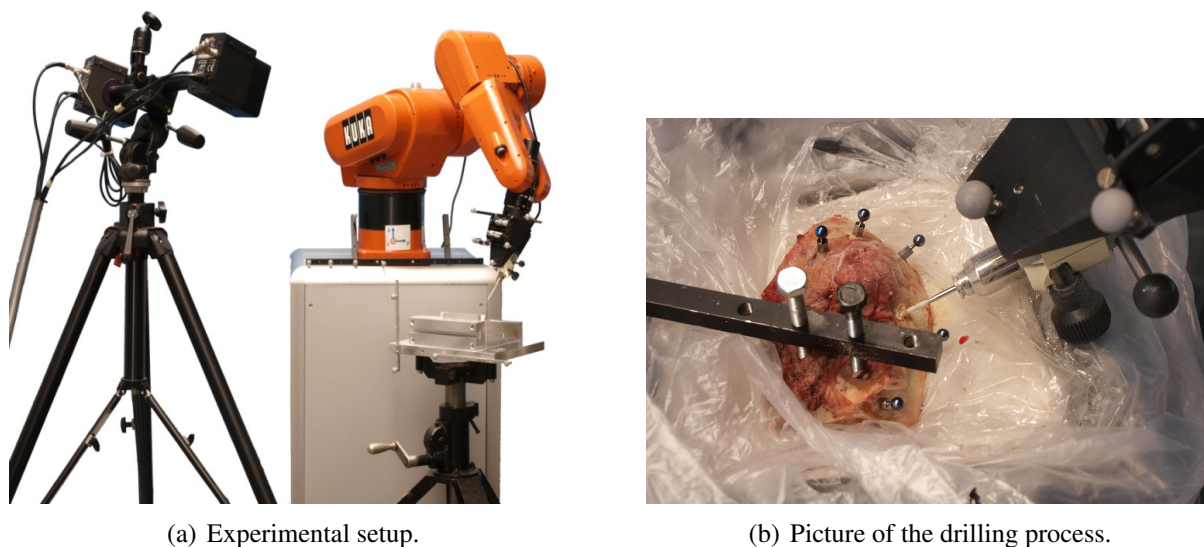
**Figure 6.3:** Experimental setup of the drilling experiments

Sphere fiducials were used as landmarks in this case.

**Table 6.2:** Intra-operative registration results [mm]

| Study 1 | FRE | Study 2 | FRE | Study 3 | FRE |
|---|---|---|---|---|---|
| EXP1-1 | 0.175 | EXP2-1 | 0.215 | EXP3-1 | 0.171 |
| EXP1-2 | 0.170 | EXP2-2 | 0.149 | EXP3-2 | 0.124 |
| EXP1-3 | 0.162 | EXP2-3 | 0.180 | EXP3-3 | 0.168 |
| EXP1-4 | 0.149 | EXP2-4 | 0.200 | EXP3-4 | 0.123 |
| EXP1-5 | 0.146 | EXP2-5 | 0.165 | EXP3-5 | 0.234 |
| EXP1-6 | 0.205 | EXP2-6 | 0.149 | EXP3-6 | 0.240 |
| EXP1-7 | 0.204 | | | EXP3-7 | 0.164 |
| EXP1-8 | 0.276 | | | EXP3-8 | 0.127 |
| EXP1-9 | 0.183 | | | EXP3-9 | 0.161 |
| EXP1-10 | 0.202 | | | EXP3-10 | 0.113 |
| Mean+SD Study 1 | $0.19 \pm 0.04$ | Mean+SD Study 2 | $0.18 \pm 0.03$ | Mean+SD Study 3 | $0.16 \pm 0.04$ |
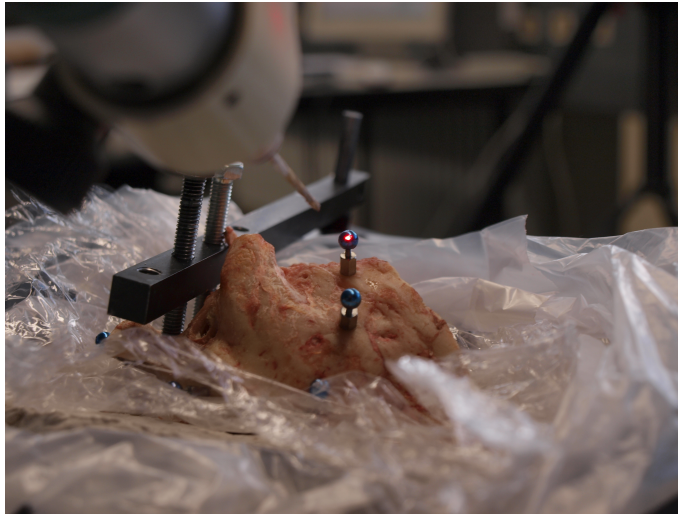
**Figure 6.4:** Cross-check of the registration result. The robot was commanded to orientate a laser pointer towards the center of a sphere fiducial. The laser dot can be seen on the surface of the landmark.

**Comparison of FRE with Predicted Values**

The observed *FREs* can be compared to expected values that are calculated on the basis of the FLE estimations by

$$
\begin{aligned}
\langle \text{FRE}^2 \rangle &\approx \left(1 - \frac{2}{N}\right) \langle \text{FLE}^2 \rangle \\
&\approx \left(1 - \frac{2}{N}\right) \left( \langle _{\text{(img)}}\text{FLE}^2 \rangle + \langle _{\text{(phys)}}\text{FLE}^2 \rangle \right) \\
&\approx \left(1 - \frac{2}{N}\right) \left( \langle _{\text{(img)}}\text{FLE}^2 \rangle + \langle _{\text{(NDI)}}\text{TRE}_{\text{pt}}^2 \rangle \right).
\end{aligned}
\tag{6.1}
$$

With $N = 5$ and using $_{\text{(img)}}\text{FLE}$ and $_{\text{(NDI)}}\text{TRE}_{\text{pt}}$ as given in Table 3.3 and Table 3.4, this yields a expected FRE of

$$
\langle \text{FRE}_{\text{Study1+2}} \rangle \approx 0.232 \text{ mm}
\tag{6.2}
$$

for the screw fiducials and

$$
\langle \text{FRE}_{\text{Study3}} \rangle \approx 0.156 \text{ mm}
\tag{6.3}
$$

for the sphere fiducials. The observed FRE of study 1 and 2 is therefore lower than expected, while the FRE of the sphere fiducials was accurately predicted by the error model.

### 6.2.2 Controller Deviations

Figure 6.5 depicts the closed loop control which was used to calculate pose commands for the robot. Poses of the robot base $^{\text{loc}}\mathbf{T}_{\text{rob}}$, the drill $^{\text{loc}}\mathbf{T}_{\text{drill}}$ and the specimen $^{\text{loc}}\mathbf{T}_{\text{spec}}$ were measured
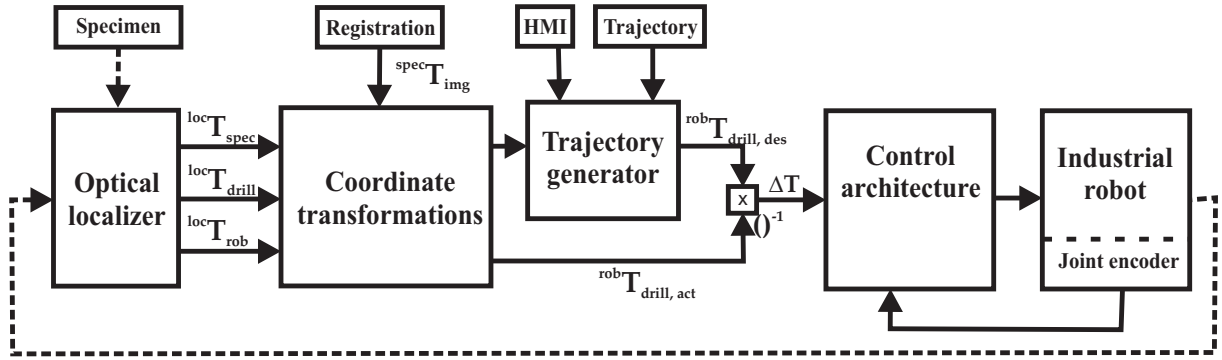


**Figure 6.5:** Control loop as used in the experimental setup

by the localizer. Furthermore, the result of the registration step was given as a transformation $^{\text{spec}}\mathbf{T}_{\text{img}}$. The desired pose $^{\text{rob}}\mathbf{T}_{\text{drill, des}}$ of the drill was calculated by a trajectory generator based on the inputs of the HMI unit as well as the coordinates of the drill path. Since it was originally given in relation to the coordinate frame $CF_{\text{img}}$ of the image data set, a transformation to the coordinate frame $CF_{\text{rob}}$ of the robot was performed by

$$^{\text{rob}}\mathbf{T}_{\text{drill, des}} = \left(^{\text{loc}}\mathbf{T}_{\text{rob}}\right)^{-1} {}^{\text{loc}}\mathbf{T}_{\text{spec}} \, {}^{\text{spec}}\mathbf{T}_{\text{img}} \, {}^{\text{img}}\mathbf{T}_{\text{drill,des}}. \tag{6.4}$$

Furthermore, actual poses $^{\text{rob}}\mathbf{T}_{\text{drill, act}}$ of the drill were calculated by

$$^{\text{rob}}\mathbf{T}_{\text{drill,act}} = \left(^{\text{loc}}\mathbf{T}_{\text{rob}}\right)^{-1} {}^{\text{loc}}\mathbf{T}_{\text{drill,act}}. \tag{6.5}$$

The differential transformation $\Delta \mathbf{T} = {}^{\text{img}}\mathbf{T}_{\text{drill,des}} \left(^{\text{loc}}\mathbf{T}_{\text{drill,act}}\right)^{-1}$ between the actual and the desired pose of the drill were processed by the control architecture and fused with the velocity information calculated from the robot's joint encoders. Separate PI controllers were implemented for the position and the orientation control of the robot. For further information, the interested reader is referred to [BEM+10].

The components of the drill's position error $\mathbf{e}$ are exemplarily depicted for EXP3-5 in Figure 6.6. It can been seen that the translational control deviation is in the range of $\pm 0.1$ mm for all spatial directions. Hence, it can be stated that the controller was able to control the drill according to the desired position commands.
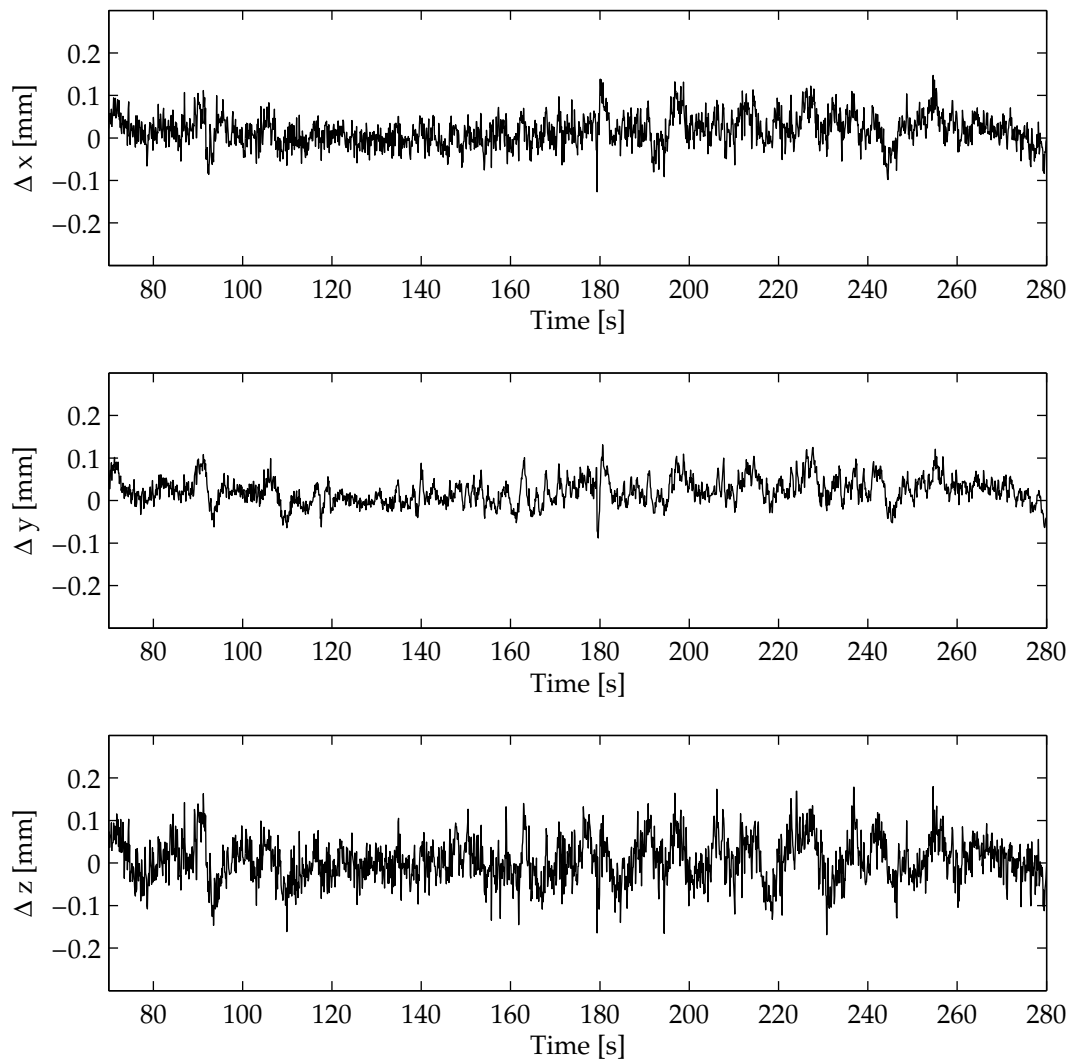
**Figure 6.6:** Translational controller deviation of the drill tip during experiment EXP3-5

## 6.3 Post-experimental Evaluation

The drilling experiments were successfully performed on 25 of 26 temporal bone specimens. However, one temporal bone (EXP2-2) was not properly fixed to the temporal bone holder which resulted in a dislocation of the specimen during drilling. After the experiments, each specimen was scanned and the image data sets containing the drilled mCIS canal were evaluated in two ways:

1. *Evaluation of post-experimental images*: The drilled mCIS canal and the anatomic structures were identified in the post-experimental image data. The integrity of temporal bone

structures was verified and the position of the cochleostomy was evaluated.

2. *Registration with planning data*: The post-experimental image data set was registered to the planning data and the deviation between the drilled canal and its intended location was calculated.

### 6.3.1  Evaluation of Post-Experimental Images

The post-experimental image data sets were loaded into the iPlan 2.6 image processing software and the drill canal was identified. The length of the drill canal between the surface of the mastoid and cochlea varied between 21.3 mm and 32.0 mm. The inspection of the drill canal was done in orthogonal views of the image data set that were aligned to the drill canal. Thus, distances between the edge of the drill canal, the facial nerve, and the chorda tympani nerve, respectively, could be measured. Figure 6.7 illustrates two exemplary views of EXP3-5.



(a)                                                  (b)
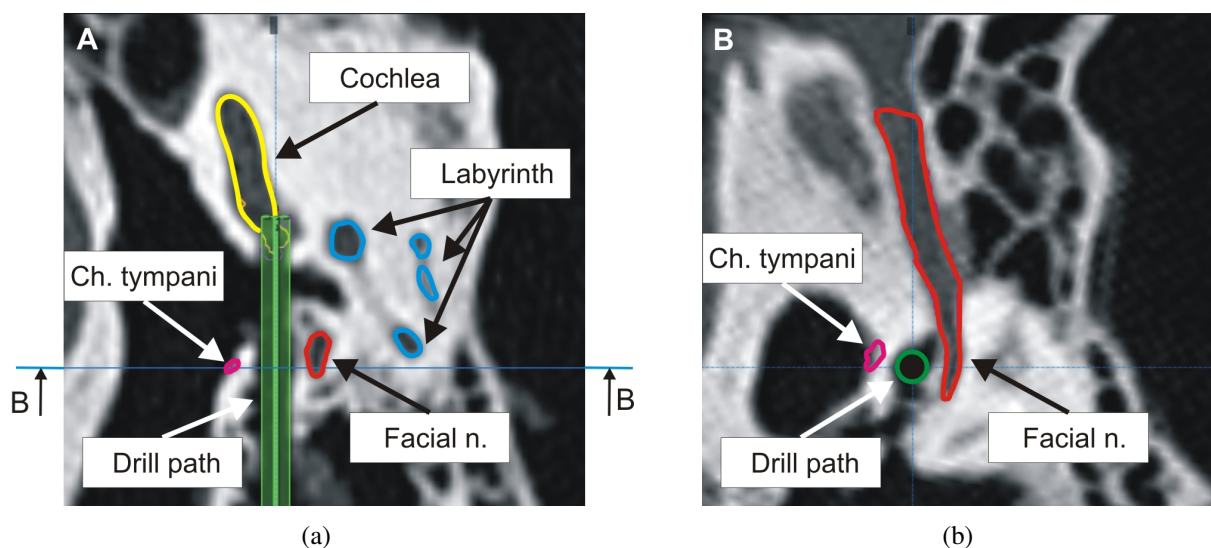
**Figure 6.7:** Post-experimental imaging of temporal bone specimen EXP3-5

The CT scans showed that the drill canal followed the intended path in each of the specimens except for EXP2-2. The improper fixation of this specimen yielded a deviation of the drill from its desired path so that the chorda tympani nerve and the auditory canal were violated. Apart from that, a violation of the chorda tympani nerve was observed in two cases (EXP1-8 and EXP2-4). This happened according to the surgical plan of EXP2-4, while it states an unplanned incident in the case of EXP1-8. Nevertheless, it was expected up to certain extend, since the safety margins of the facial nerve and the chorda tympani nerve were extraordinary small for EXP1-8 (0.2 mm and 0.3 mm).

The facial nerve was not violated in any of the experiments. In one case (EXP1-9) post-experimental images suggested a possible contact between the drill canal and the facial nerve. This specimen

was therefore additionally inspected by using a conventional mastoidectomy. The exploration of the facial nerve revealed that it was not violated [MRB$^+$09]. The results of all three studies are summarized in Table 6.3.

**Table 6.3:** Results of drilled mCIS canals: distances between the outer wall and the facial nerve respectively the chorda tympani nerve as well as integrity of the auditory canal. The outcome was determined using iPlan 2.6 image processing software. Distances are therefore given with one position after decimal point. Abbreviations: viol. - violation; n.viol. - no violation.

| Temporal bone | Distance $d_{fn}$ [mm] to facial nerve | | Distance $d_{ct}$ [mm] to chorda tympani nerve | | Integrity of auditory canal |
|---|---|---|---|---|---|
| | Target | Outcome | Target | Outcome | |
| EXP1-1 | 0.839 | 0.5 | 0.153 | 0.4 | n.viol. |
| EXP1-2 | 0.660 | 0.3 | 0.303 | 0.9 | n.viol. |
| EXP1-3 | 0.692 | 0.2 | 0.310 | 1.2 | n.viol. |
| EXP1-4 | 0.391 | 0.2 | 0.303 | 0.5 | n.viol. |
| EXP1-5 | 0.742 | 0.3 | 0.316 | 0.7 | n.viol. |
| EXP1-6 | 0.807 | 0.2 | 0.262 | 1.6 | n.viol. |
| EXP1-7 | 0.346 | 0.1 | viol. | 0.6 | n.viol. |
| EXP1-8 | 0.323 | 0.4 | 0.200 | **viol.** | n.viol. |
| EXP1-9 | 0.449 | 0.0 | 0.309 | 1.2 | n.viol. |
| EXP1-10 | 0.816 | 0.7 | 0.419 | 0.4 | n.viol. |
| Mean + SD | $0.61 \pm 0.21$ | $0.29 \pm 0.20$ | $0.25 \pm 0.13$ | $0.83 \pm 0.42$ | |
| EXP2-1 | 0.911 | 0.6 | 0.408 | 0.4 | n.viol. |
| EXP2-2 | 0.531 | 1.7 | 0.021 | **viol.** | **viol.** |
| EXP2-3 | 0.615 | 0.6 | 0.407 | 1.4 | n.viol. |
| EXP2-4 | 1.360 | 0.8 | viol. | viol. | n.viol. |
| EXP2-5 | 0.510 | 0.6 | 0.403 | 0.4 | n.viol. |
| EXP2-6 | 0.804 | 0.5 | 0.308 | 0.8 | n.viol. |
| Mean + SD | $0.84 \pm 0.33$ | $0.62 \pm 0.11$ | $0.38 \pm 0.05$ | $0.75 \pm 0.47$ | |
| EXP3-1 | 0.877 | 0.2 | 0.500 | 1.0 | n.viol. |
| EXP3-2 | 0.726 | 0.3 | 0.428 | 0.6 | n.viol. |
| EXP3-3 | 0.833 | 0.2 | 0.478 | 1.1 | n.viol. |
| EXP3-4 | 1.148 | 0.9 | 0.604 | 0.4 | n.viol. |
| EXP3-5 | 1.093 | 0.8 | 0.581 | 0.8 | n.viol. |
| EXP3-6 | 0.982 | 0.8 | 0.558 | 0.6 | n.viol. |
| EXP3-7 | 1.014 | 0.7 | 0.578 | 0.4 | n.viol. |
| EXP3-8 | 0.880 | 0.8 | 0.500 | 0.6 | n.viol. |
| EXP3-9 | 1.072 | 0.9 | 0.569 | 0.7 | n.viol. |
| EXP3-10 | 1.106 | 0.9 | 0.589 | 1.0 | n.viol. |
| Mean + SD | $0.97 \pm 0.14$ | $0.65 \pm 0.30$ | $0.54 \pm 0.06$ | $0.72 \pm 0.25$ | |

**Assessment of the Cochleostomy Point**

The image data was further evaluated with respect to the location of the cochleostomy point. For each specimen, it was verified if the cochlea was successfully opened at the basal turn. In addition to that, the position of the cochleostomy was reviewed with respect to its location within the scala

tympani. The location of the drill canal was determined as being peripheral if the cochleostomy point was assumed to be too close to the scala vestibuli ([MRB$^+$09]).

The results are summarized in Table 6.4. Except from EXP2-2, the drill canal successfully reached the basal turn of the cochlea in 25 specimens. The cochleostomy, however, was not successfully completed in some cases. Two types of incomplete cochleostomies were observed:

1. The drill stopped shortly before opening the cochlea (EXP1-8 and EXP 1-10). Nevertheless, the cochleostomy point would have been at the intended location of the basal turn if drilling would have been proceeded. This is illustrated in Figure 6.8(a).

2. The drill partly missed the basal turn so that the resulting cochleostomy is too small. This is illustrated in Figure 6.8(b).
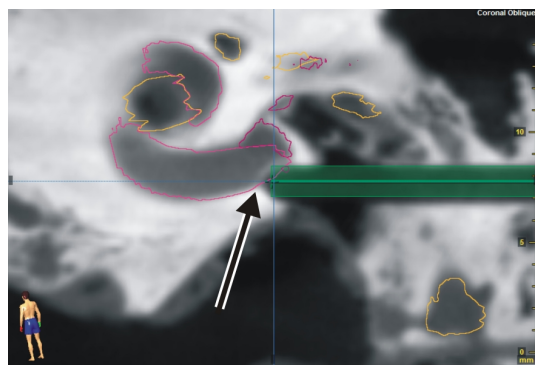


(a) EXP1-8: A small bony overhang is remaining between drill canal (green) and basal turn of the cochlea (red).
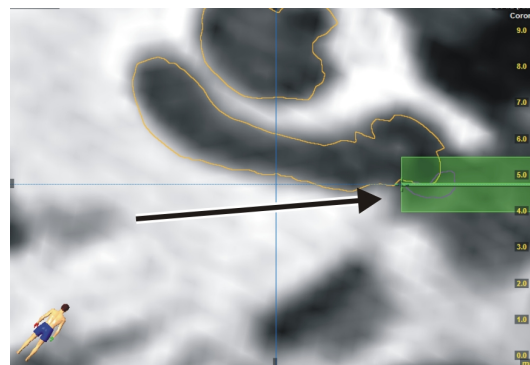
(b) EXP3-2: The tip of the drill partly opened the scala tympani. The cochleostomy is too small for an insertion of the implant.

**Figure 6.8:** Types of incomplete cochleostomies that were observed in experimental studies

### 6.3.2 Registration with Planning Data

The experimental results were further evaluated with respect to the planned coordinates of the mCIS path. Therefore, post-experimental images were registered to the pre-experimental planning data set and the deviations between the identified and the planned drill paths were calculated. This was done in particular at two important locations: at the cochleostomy point and at the level of the facial recess. These state the most sensitive areas of the drill path. Additionally, the angular error was determined. Note that EXP2-2 was not considered for the calculation of mean values in study 2 because of the fact that the deviation was caused by an improper fixation of the temporal bone specimen and not by an error of the IGS system.

Since image registration is never performed perfectly it has to be noted that the results given in Table 6.5 are also affected by inaccuracies. However, the level of inaccuracy can be theoretically determined in this case by calculating the $\langle TRE \rangle$ of the image-to-image registration at the

**Table 6.4:** Position of the cochleostomy

| Temporal bone | Cochleostomy | | |
|---|---|---|---|
| | complete/n.complete | Entering cochlea at: | Location within Scala tympani (central/peripheral) |
| EXP1-1 | complete | Basal turn | Central |
| EXP1-2 | complete | Basal turn | Central |
| EXP1-3 | complete | Basal turn | Central |
| EXP1-4 | complete | Basal turn | Peripheral |
| EXP1-5 | complete | Basal turn | Peripheral |
| EXP1-6 | complete | Basal turn | Central |
| EXP1-7 | complete | Basal turn | Central |
| EXP1-8 | n. complete | Basal turn | Central |
| EXP1-9 | complete | Basal turn | Peripheral |
| EXP1-10 | n. complete | Basal turn | Central |
| EXP2-1 | complete | Basal turn | Peripheral |
| EXP2-2 | n. complete | - | - |
| EXP2-3 | complete | Basal turn | Central |
| EXP2-4 | complete | Basal turn | Central |
| EXP2-5 | complete | Basal turn | Central |
| EXP2-6 | complete | Basal turn | Peripheral |
| EXP3-1 | complete | Basal turn | Central |
| EXP3-2 | n. complete | Basal turn | Central |
| EXP3-3 | complete | Basal turn | Peripheral |
| EXP3-4 | complete | Basal turn | Peripheral |
| EXP3-5 | n. complete | Basal turn | Central |
| EXP3-6 | n. complete | Basal turn | Central |
| EXP3-7 | complete | Basal turn | Central |
| EXP3-8 | complete | Basal turn | Peripheral |
| EXP3-9 | complete | Basal turn | Central |
| EXP3-10 | complete | Basal turn | Peripheral |

cochleostomy point. Using Equation 3.8 together with given values for the FLE (see Table 3.3) as well as the setup of the cochleostomy point (see Table 3.5), this yields a $\left\langle \text{TRE}_{\text{Study1+2}} \right\rangle =$ 0.237 mm for study 1 and 2 and a $\left\langle \text{TRE}_{\text{Study3}} \right\rangle = 0.14$ mm for study 3.

Based on the number of experiments that were performed as well as the statistical behavior of the errors, it is assumed that the mean values of each study sufficiently describe the outcome of the experiments. It can be summarized as follows:

- *Registration accuracy:* The registration was performed with a mean FRE of $(0.22 \pm 0.04)$ mm in study 1, $(0.26 \pm 0.07)$ mm in study 2, and $(0.14 \pm 0.03)$ mm in study 3. The lower FRE value that is observed in study 3 corresponds to the fact that sphere fiducials were used for registration.

- *Deviation at cochleostomy depth:* The deviation at the level of the cochleostomy varies between 0.106 mm (EXP3-2) and 1.559 mm (EXP2-6). The mean deviations of study 1 and study 2 are comparable, with a larger standard deviation observed in study 2 (study 1:

(a) Position of the cochleostomy - Series 1.

| Temporal bone | FRE of the pre- and postoperative image data registration | Deviation from desired position at cochleostomy depth [mm] | Deviation from desired position at level of facial recess [mm] | Angular error |
|---|---|---|---|---|
| EXP1-1 | 0.254 | 0.614 | 0.499 | 0.994 |
| EXP1-2 | 0.211 | 0.710 | 0.609 | 1.190 |
| EXP1-3 | 0.211 | 1.261 | 1.149 | 0.956 |
| EXP1-4 | 0.199 | 0.589 | 0.420 | 1.343 |
| EXP1-5 | 0.201 | 0.687 | 0.553 | 1.222 |
| EXP1-6 | 0.252 | 0.677 | 0.648 | 0.421 |
| EXP1-7 | 0.257 | 0.606 | 0.515 | 1.522 |
| EXP1-8 | 0.257 | 0.378 | 0.307 | 0.502 |
| EXP1-9 | 0.138 | 1.236 | 1.099 | 1.327 |
| EXP1-10 | 0.269 | 1.033 | 0.873 | 1.828 |
| Mean + SD | $0.22 \pm 0.04$ | $0.78 \pm 0.30$ | $0.67 \pm 0.28$ | $1.13 \pm 0.43$ |

(b) Position of the cochleostomy - Series 2.

| Temporal bone | FRE of the pre- and postoperative image data registration | Deviation from desired position at cochleostomy depth [mm] | Deviation from desired position at level of facial recess [mm] | Angular error |
|---|---|---|---|---|
| EXP2-1 | 0.246 | 1.205 | 1.042 | 1.439 |
| EXP2-2 | - | - | - | - |
| EXP2-3 | 0.253 | 0.345 | 0.262 | 2.601 |
| EXP2-4 | 0.162 | 0.489 | 0.382 | 1.367 |
| EXP2-5 | 0.359 | 0.346 | 0.228 | 1.000 |
| EXP2-6 | 0.288 | 1.549 | 1.225 | 3.264 |
| Mean + SD | $0.26 \pm 0.07$ | $0.79 \pm 0.56$ | $0.63 \pm 0.47$ | $1.93 \pm 0.96$ |

(c) Position of the cochleostomy - Series 3.

| Temporal bone | FRE of the pre- and postoperative image data registration | Deviation from desired position at cochleostomy depth [mm] | Deviation from desired position at level of facial recess [mm] | Angular error |
|---|---|---|---|---|
| EXP3-1 | 0.181 | 1.025 | 0.861 | 1.240 |
| EXP3-2 | 0.113 | 0.106 | 0.145 | 0.633 |
| EXP3-3 | 0.104 | 0.743 | 0.623 | 0.940 |
| EXP3-4 | 0.135 | 0.889 | 0.716 | 1.287 |
| EXP3-5 | 0.156 | 0.269 | 0.232 | 0.599 |
| EXP3-6 | 0.144 | 0.351 | 0.199 | 1.147 |
| EXP3-7 | 0.165 | 0.157 | 0.105 | 0.469 |
| EXP3-8 | 0.122 | 0.823 | 0.683 | 1.043 |
| EXP3-9 | 0.077 | 0.712 | 0.557 | 1.225 |
| EXP3-10 | 0.154 | 0.840 | 0.708 | 1.005 |
| Mean + SD | $0.14 \pm 0.03$ | $0.59 \pm 0.34$ | $0.48 \pm 0.28$ | $0.96 \pm 0.29$ |

**Table 6.5:** Results of the post-experimental evaluation

$(0.78 \pm 0.30)$ mm; study 2: $(0.79 \pm 0.56)$ mm). The deviations of study 3 have a mean value of $(0.59 \pm 0.34)$ mm which is approximately 0.2 mm less than the results of the other studies. This confirms that the use of sphere fiducials yields to more accurate results than the use of screw fiducials.

- *Deviation at the level of the facial recess:* The deviation of the drill path at the level of the facial recess is about 0.1 mm less than the deviation at the cochleostomy point. It ranges from 0.105 mm to 1.225 mm.

- *Angular error:* The mean angular error is $(1.13\pm0.43)°$ for study 1, $(1.93\pm0.96)°$ for study 2 and $(0.96\pm0.29)°$ for study 3. According to the position inaccuracies, the most accurate results for the orientation of the drill canal were observed in study 3.

Figure 6.9 and Figure 6.10 illustrate the deviations between the identified and desired drill paths in case of the most accurate (EXP3-2) as well as the most inaccurate case (EXP3-1) of study 3. This is shown in two ways: the drill is visualized as a 3D model within the corresponding planning data and the deviation is plotted in relation to the insertion depth. The results of EXP3-1 show that the deviation increased from approximately 0.4 mm at the level of the entry point to 1.0 mm at the level of the cochleostomy. The deviations of EXP3-2 decreased from approximately 0.4 mm at the level of the entry point to 0.1 mm at the level of the cochleostomy. These examples illustrate that the deviation at the entry point can be compared at least for these two cases. Nevertheless, this effect was also observed in the other experiments. Table 6.6 summarizes the entry point deviations for all studies. The mean error of each study is lower compared to the corresponding error at the cochleostomy depth. The best result was achieved in study 3 with a deviation of $(0.30 \pm 0.11)$ mm.

**Table 6.6:** Deviation [mm] between intended and drilled canal at the entry point

| Study 1 | Deviation | Study 2 | Deviation | Study 3 | Deviation |
|---------|-----------|---------|-----------|---------|-----------|
| EXP1-1 | 0.208 | EXP2-1 | 0.646 | EXP3-1 | 0.407 |
| EXP1-2 | 0.099 | EXP2-2 | - | EXP3-2 | 0.364 |
| EXP1-3 | 0.843 | EXP2-3 | 1.167 | EXP3-3 | 0.384 |
| EXP1-4 | 0.079 | EXP2-4 | 0.446 | EXP3-4 | 0.231 |
| EXP1-5 | 0.144 | EXP2-5 | 0.240 | EXP3-5 | 0.263 |
| EXP1-6 | 0.574 | EXP2-6 | 0.082 | EXP3-6 | 0.161 |
| EXP1-7 | 0.526 | | | EXP3-7 | 0.097 |
| EXP1-8 | 0.115 | | | EXP3-8 | 0.339 |
| EXP1-9 | 0.582 | | | EXP3-9 | 0.272 |
| EXP1-10 | 0.401 | | | EXP3-10 | 0.436 |
| Mean + SD | $0.36 \pm 0.27$ | Mean + SD | $0.52 \pm 0.42$ | Mean + SD | $0.30 \pm 0.11$ |

## 6.4 Discussion

The results of the performed temporal bone studies showed that an image guided and robot assisted mCIS is generally feasible. The mCIS canals were drilled into 26 temporal bone specimens

(a)                                                             (b)
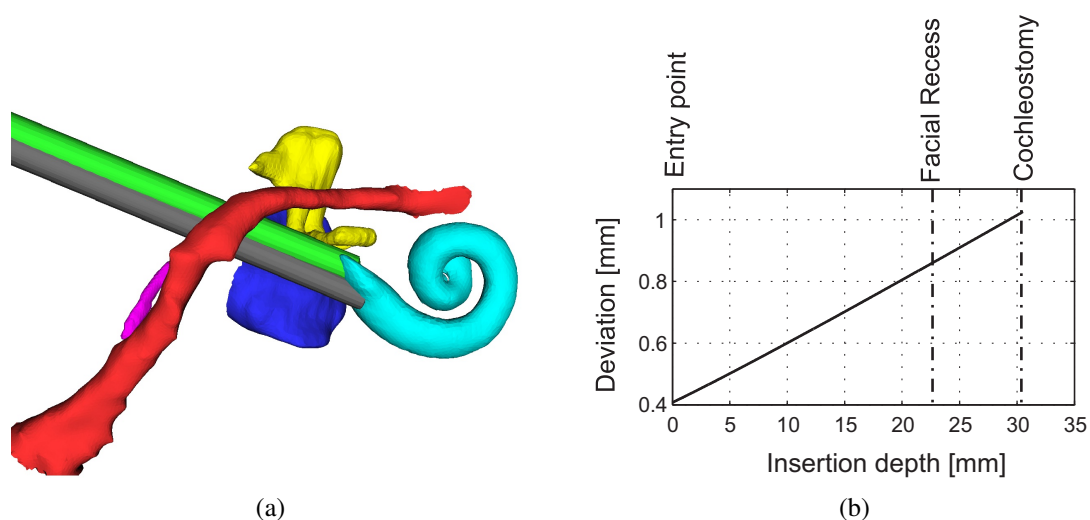
**Figure 6.9:** Location of the drill path, plotted to the planning data of EXP3-1. Color code: facial
nerve - red; chorda tympani nerve - magenta; ossicles - yellow; auditory canal - blue;
scala tympani of the cochlea - cyan; determined drill canal - green; planned drill canal
- grey.



(a)                                                             (b)
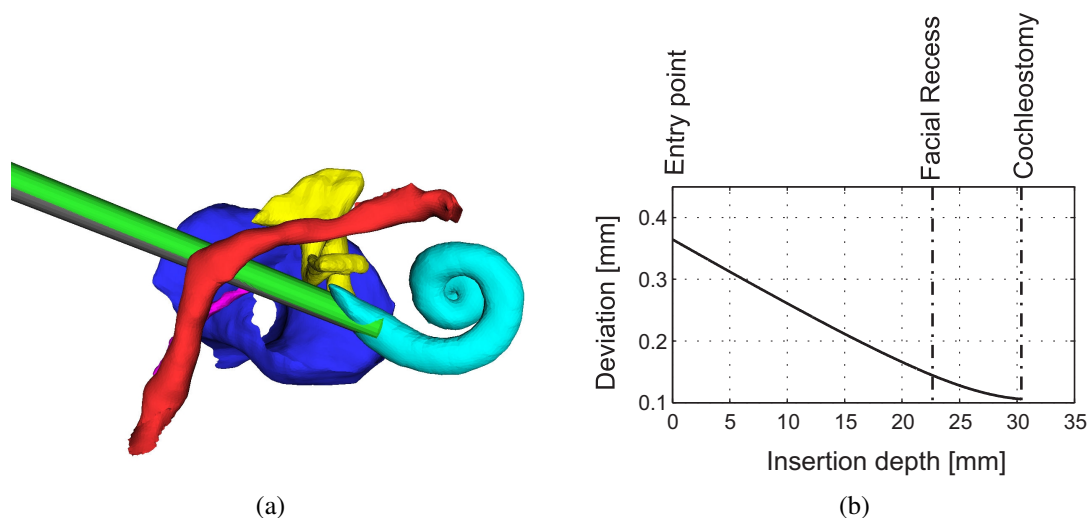
**Figure 6.10:** Location of the drill path, plotted to the planning data of EXP3-2. Color code: facial
nerve - red; chorda tympani nerve - magenta; ossicles - yellow; auditory canal - blue;
scala tympani of the cochlea - cyan; determined drill canal - green; planned drill
canal - grey.

without violating the facial nerve. The deviation of the entry point of the drill at the mastoid
was estimated with the experimental setup of study 3 to $(0.30 \pm 0.11)$ mm. Inaccuracies of this
range would be sufficient for a cochleostomy. However, it was also observed that in 24 out of 26

experiments the deviation increases according to the depth of the drilled canal. Inaccuracies of $(0.59 \pm 0.34)$ mm were measured at the point of the cochleostomy. This effect was expected to a certain degree since the entry point is closer to the fiducial point configuration and thus can be located more accurately by the IGS system than the cochleostomy point. Nevertheless, a calculation of the expected TRE using the error model as presented in Section 3.8 would yield to a TRE of the entry point which is only 0.03 mm less than the TRE of the cochleostomy point (cp. Equation 3.26). As a consequence, the observed increase of the error might be explained by different aspects, such as:

- The fixation of the temporal bone might have been insufficient, yielding to a small change in orientation under the applied external forces of the drilling process. This is not detected by the IGS system, since the reference adapter is mounted to the temporal bone holder.

- The temporal bone specimen might have been deformed due to the applied forces of the drilling process as well as the mechanical fixation. These kinds of deformation cannot be detected by the IGS system.

- The bony structure of the mastoid consists of a porous structure, which is further characterized by a high level of heterogeneity. This causes asymmetric forces that are applied to the tip of the instrument during drilling. This might have an influence on the mounting of the drill in terms of a decreased calibration accuracy.

- The specimens were stored in a frozen condition and defrosted for preparation, imaging and drilling. Thermal expansion could be the reason for a small change of the temporal bone structure after imaging. This cannot be detected by the IGS system.

The presented cadaver studies aim to investigate the feasibility of the mCIS approach. The results show that the accuracy of the drilling process particularly at the depth of the cochleostomy needs further improvement before this approach can be investigated under a clinical point of view. In addition to that, a safety concept needs to be developed. This includes mechanisms that are particularly able to detect a violation of the facial nerve as well as instruments and operating procedures that are designed to handle adverse events (e.g. unexpected bleeding).

# 7 Conclusion and Perspectives

The development of technological assistance systems for surgical applications aims at increasing the accuracy as well as minimizing the trauma of the intervention. Cochlea implant surgery is an exemplary discipline, in which exceptionally high accuracy is demanded because of the sensitive anatomical structures that are located in direct proximity to the operating area. A minimally invasive approach in this field has numerous advantages which is why various groups are working on a concept of such an approach.

In this work, the inaccuracies that are involved in the concept of an image guided and robotic performed minimally invasive drill canal towards the cochlea are examined. This approach has numerous advantages but requires a thorough investigation of the expected deviation from the planning data. Therefore, a theoretical model of the navigational error is introduced. It is based on statistical error distributions of the inaccuracies occurring during target point localization, drill localization and positioning of the instrument, respectively. Consequently, the term *Target Navigation Error (TNE)* is defined in this work to express this error.

The technological components involved in the workflow of the intervention are analyzed and potential sources of errors are identified. Furthermore, optically localized instruments as well as different types of landmarks are investigated and their level of inaccuracy is determined in terms of FLE. In this context, unknown calibration errors of instruments are also considered in the developed theoretical error model. A confidence region is derived for the expected value of the TNE based on a Gaussian error distribution. The theoretical model results in a predicted TNE of the given application of 1.158 mm for a 99.9 % confidence region. The applicability of the error model is confirmed by empirical measurements of the TNE using a setup with artificial targets.

The predicted TNE plays an important role in the planning process of the mCIS. The demand of a tangential approach to the windings of the cochlea and the spatial arrangement of the temporal bone anatomy require that the drill canal is placed within the facial recess. The available space for sufficient safety margins is severely limited by this anatomic constraint. Hence, a 3D model of the patient, containing segmentations of the temporal bone anatomy, is used to determine optimal coordinates of the mCIS drill canal. The expected TNE as well as the individual priority of the anatomic structures are considered as a criterion in the optimization process. Distances between the drill path and important anatomic structures are maximized by this approach which increases the patient's safety. Furthermore, the use of a 3D model instead of a large number of slice images facilitates the planning process for the surgeon.

The feasibility of the mCIS approach is evaluated in experimental studies on a considerable amount of temporal bone specimens. Different types of segmentation techniques and fiducial landmarks are evaluated in these experiments. The results show that the error can be significantly reduced by using the developed type of sphere fiducials instead of screw fiducials. Moreover,

the observed error at the entry point of the mastoid is as predicted by the error model, while a significant increase of the error is observed with an increasing depth of the drill canal. Various potential reasons are suggested that could explain this effect. Nevertheless, the mCIS drill canal successfully reached the basal turn of the cochlea in 25 out of 26 cases with no violation of the most important anatomic structure (facial nerve). An unplanned violation of the chorda tympani nerve was observed in one case but can be explained by an extraordinarily small facial recess of that specimen. Consequently, patients with such an anatomic arrangement need to be excluded from this approach.

The results of the performed experiments show that a minimally invasive approach to the cochlea might be feasible but requires further improvements to the accuracy especially in the presence of drilling forces. Furthermore, new questions are raised by this work. Amongst others, these are related to the accuracy improvement of the system, the safety concept, as well as the reliability of the fixation of reference adapters. One of the central questions that needs to be addressed in the future is related to the danger of violating any of the sensitive anatomical structures. Therefore, future research issues have to particularly include an online measurement of the bone removal process in order to increase the accuracy of the system as well as the safety of the patient.

A possible approach is presented in [EWO⁺09]. A local 3D imaging unit in terms of an optical coherence tomography (OCT) system is suggested to acquire high resolution tomographic image data of the target area during the intervention. Sensitive anatomic areas need to be identified within these online images so that the drilling strategy can be adapted to the actual situation. Furthermore, if the OCT image data can be registered to the planning data, this information might be used to increase the accuracy of the navigation process. The use of OCT further allows the implementation of laser cutting strategies. These have the advantage, that no interaction forces between the patient and the laser occur [BKK⁺09]. In this case, the process of bone removal would be even more accurate.

Besides an improvement of the accuracy of this approach, an appropriate tool needs to be developed that is capable to insert the implant to its desired location via the drill canal. Actual prototypes consist of a u-shaped tube of 4 mm diameter [HRO⁺09]. However, this needs to be significantly miniaturized in order to fit into the drill canal. The tool as well as the accuracy of the navigation process define limiting values for the size of the drill canal, which means that they have an impact on each other. The goals of miniaturization and accuracy improvements therefore need to be commonly defined before a successful implementation of a minimally invasive approach to cochlear implant surgery is possible.

This work provides a mathematical model for an error prediction of image guided and robotic assisted interventions. In addition to the concept of an mCIS which has been the main scope of this work, this model can be adapted to other surgical applications, as well. It states a contribution to the use of mechatronical assistance in the operating theater in order to extend the capabilities of surgeons and to push the development of new surgical techniques.

# Bibliography

[Bau07]  M. A. Bauer. *Tracking Errors in Augmented Reality*. Phd thesis, Technische Universität München, Institut für Informatik, Chair for Computer-Aided Medical Procedures & Augmented Reality, 2007.

[BEM⁺10]  S. Baron, H. Eilers, B. Munske, J. L. Toennies, R. Balachandran, R. F. Labadie, T. Ortmaier, and R. J. Webster. Percutaneous inner-ear access via an image-guided industrial robot system. *Proceedings of the Institution of Mechanical Engineers, Part H: Journal of Engineering in Medicine*, 224:633–649, 2010.

[BF09]  R. Balachandran and J. M. Fitzpatrick. Iterative Solution for Rigid-Body Point-Based Registration with Anisotropic Weighting. In Michael I. Miga and Kenneth H. Wong, editors, *Medical Imaging 2009: Visualization, Image-Guided Procedures, and Modeling*. SPIE, 2009.

[BGNO04]  K. Bhatia, K. P. Gibbin, T. P. Nikolopoulos, and G. M. O'Donoghue. Surgical complications and their management in a series of 300 consecutive pediatric cochlear implantations. *Otol Neurotol*, 25(5):730–739, Sep 2004.

[BHWC08]  W. Birkfellner, J. Hummel, E. Wilson, and K. Cleary. Tracking devices. In *Image-Guided Interventions*, pages 23–44. Springer US, 2008.

[BKK⁺09]  J. Burgner, F. B. Knapp, L. Kahrs, J. Raczkowsky, J. Schipper, H. Wörn, and T. Klenzner. Setup and experimental trial for robot-assisted laser cochleostomy. *International Journal of Computer Assisted Radiology and Surgery*, pages 1864–1865, 2009.

[BLG⁺07]  S. H. Bartling, M. Leinung, J. Graute, T. Rodt, C. Dullin, H. Becker, T. Lenarz, T. Stover, and O. Majdani. Increase of accuracy in intraoperative navigation through high-resolution flat-panel volume computed tomography: experimental comparison with multislice computed tomography-based navigation. *Otol Neurotol*, 28(1):129–134, Jan 2007.

[Blu10]  S. Blume. *The artificial ear: cochlear implants and the culture of deafness*. Rutgers University Press, New Brunswick, New Jersey, and London, 2010. ISBN 978-0-8135-4660-5.

[Bou07]  J.-Y. Bouguet. Camera Calibration Toolbox for Matlab®, Computer Vision Research Group, California Institute of Technology, Pasadena. Available online: http://www.vision.caltech.edu/bouguetj/calib_doc/, 2007.

[BSFS06]  G. R. Barton, P. C. Stacey, H. M. Fortnum, and A. Q. Summerfield.  Hearing-impaired children in the United Kingdom, IV: cost-effectiveness of pediatric cochlear implantation. *Ear Hear*, 27(5):575–588, Oct 2006.

[BTP+07]  P. N. Brett, R. P. Taylor, D. Proops, C. Coulson, A. Reid, and M. V. Griffiths.  A surgical robot for cochleostomy. pages 1229 –1232, Oct 2007.

[CRPB07]  C. J. Coulson, A. P. Reid, D. W. Proops, and P. N. Brett.  ENT challenges at the small scale. *Int J Med Robot*, 3(2):91–96, Jun 2007.

[CSW+09]  M. Caversaccio, C. Stieger, S. Weber, R. Häusler, and L-P. Nolte.  Navigation and robotics of the lateral skull base. *HNO*, 57(10):975–982, Oct 2009.

[CT81]  G. M. Clark and Y. C. Tong.  Multiple-electrode cochlear implant for profound or total hearing loss: a review. *Med J Aust*, 1(8):428–429, Apr 1981.

[Djo53]  A. Djourno.  Induced electric excitation localized at a distance. *C R Hebd Seances Acad Sci*, 236(24):2337–2338, Jun 1953.

[EBO+09]  H. Eilers, S. Baron, T. Ortmaier, B. Heimann, C. Baier, T. S. Rau, M. Leinung, and O. Majdani. Navigated, robot assisted drilling of a minimally invasive cochlear access. In *Proceedings of the 2009 IEEE International Conference on Mechatronics*, Málaga, Spain, April 2009. IEEE.

[EHB+07]  H. Eilers, A. Hussong, S. Baron, B. Heimann, Th. Rau, M. Leinung, Th. Lenarz, and O. Majdani.  Optimierung der Trajektorienplanung für eine minimalinvasive Cochleostomie [Optimization of the Trajectory Planning for minimally invasive Cochleostomy].  In *Tagungsband der 6. Jahrestagung der Deutschen Gesellschaft für Computergestützte Chirurgie (CURAC)*, pages 219–222. Berlin : Pro BUSI-NESS, 2007.

[ELF97]  D.W. Eggert, A. Lorusso, and R.B. Fisher.  Estimating 3D rigid body transformations: a comparison of four major algorithms. In *Machine Vision and Applications*, volume 9, pages 272 – 290. Springer-Verlag 1997, 1997.

[EWO+09]  H. Eilers, M. Wienke, T. Ortmaier, O. Majdani, and M. Leinung. Multimodal Image Registration of VCT and OCT Images: a Step towards High Accuracy in Surgical Navigation. In *Int J CARS*, volume 4 (Suppl 1), pages S124 – S125. Springer, June 2009.

[FAR08]  FARO EUROPE GmbH & Co.KG. FARO Gage & Gage-PLUS product information. www.faro.com, 2008. accessed 07.10.2009.

[FGHP03]  P. A. Federspil, U. W. Geisthoff, D. Henrich, and P. K. Plinkert. Development of the first force-controlled robot for otoneurosurgery. *The Laryngoscope*, 113:465–471, March 2003.

[FHM00]  J. M. Fitzpatrick, D. L. G. Hill, and C. R. Maurer. Image registration. In J. Michael Fitzpatrick and Milan Sonka, editors, *"Handbook of Medical Imaging, Volume 2. Medical Image Processing and Analysis* , pages 449 – 514. SPIE Press, 2000.

[Fit09]  J. M. Fitzpatrick. Fiducial registration error and target registration error are uncorrelated. In Michael I. Miga and Kenneth H. Wong, editors, *Medical Imaging 2009: Visualization, Image-Guided Procedures, and Modeling*, volume 7261. SPIE, 2009.

[Fit10]  J. M. Fitzpatrick. The role of registration in accurate surgical guidance. *Proceedings of the Institution of Mechanical Engineers, Part H: Journal of Engineering in Medicine*, 224(5/2010):607–622, 2010.

[FW01]  J. M. Fitzpatrick and J. B. West. The distribution of target registration error in rigid-body point-based registration. *IEEE Trans Med Imaging*, 20(9):917–927, Sep 2001.

[FWM98]  J. M. Fitzpatrick, J. B. West, and C. R. Maurer. Predicting error in rigid-body point-based registration. *IEEE Trans Med Imaging*, 17(5):694–702, Oct 1998.

[GGS$^+$06]  R. Gupta, M. Grasruck, C. Suess, S. H. Bartling, B. Schmidt, K. Stierstorfer, S. Popescu, T. Brady, and T. Flohr. Ultra-high resolution flat-panel volume CT: fundamental principles, design architecture, and system characterization. *Eur Radiol*, 16(6):1191–1205, Jun 2006.

[GP08]  R. Galloway and T. Peters. Overview and history of image-guided interventions. In *Image-Guided Interventions*, pages 1–21. Springer US, 2008.

[Han09]  H. Handels. *Medizinische Bildverarbeitung*. Wiesbaden : Vieweg + Teubner, 2nd edition, 2009.

[Hei10]  M. Heidel. *Vergleich der manuellen und automatischen Planung einer Bohrtrajektorie als minimal-invasiver Zugang für Cochlea-Implantat-Operationen*. Phd thesis, Department of Otolaryngology, Hannover Medical School, 2010.

[HML02]  R. Heermann, O. Majdani, and T. Lenarz. Computergestützt Navigation im Kopf-Hals-Bereich. In E. Biesinger and H. Iro, editors, *HNO Praxis heute*, volume 22, chapter 7, pages 129–154. Springer-Verlag, 2002.

[Hou73]  G. N. Hounsfield. Computerized transverse axial scanning (tomography). 1. description of system. *Br J Radiol*, 46(552):1016–1022, Dec 1973.

[HRE$^+$08]  A. Hussong, T. S. Rau, H. Eilers, S. Baron, B. Heimann, M. Leinung, T. Lenarz, and O. Majdani. Conception and Design of an Automated Insertion Tool for Cochlear Implants. In *Proc. of the 30th Annual International Conference of the IEEE Engineering in Medicine and Biology Society*, volume 30, pages 5593–5596, Vancouver, Canada, August 2008.

[HRO+09] A. Hussong, T. S. Rau, T. Ortmaier, B. Heimann, T. Lenarz, and O. Majdani. An automated insertion tool for cochlear implants: another step towards atraumatic cochlear implant surgery. *International Journal of Computer Assisted Radiology and Surgery*, 2009. Published online: 13. Juni 2009.

[HRR08] D. Holmes, M. Rettmann, and R. Robb. Visualization in image-guided interventions. In *Image-Guided Interventions*, pages 45–80. Springer US, 2008.

[ISO04] *Statistik - Genauigkeit von Messungen - Ringversuche*, volume 355 of *DIN Taschenbuch*. Beuth Verlag GmbH, Berlin, Wien, Zürich, 2004.

[Kal05] W. A. Kalender. *Computed Tomography - Fundamentals, System Technology, Image Quality, Applications.* Publicis, Erlangen, 2nd edition, 2005.

[KBE+07] J. Kotlarski, S. Baron, H. Eilers, J. Hofschulte, and B. Heimann. Improving the performance of an optical tracking system using data fusion with an inertial measurement unit. In *11th Conference on Mechatronics Technology*, pages 225–230, Ulsan, Korea, November 2007.

[KHN+09] R. Konietschke, U. Hagn, M. Nickl, S. Jorg, A. Tobergte, G. Passig, U. Seibold, L. Le-Tien, B. Kubler, M. Groger, F. Frohlich, C. Rink, A. Albu-Schaffer, M. Grebenstein, T. Ortmaier, and G. Hirzinger. The DLR MiroSurge - A robotic system for surgery. In *Proc. IEEE Int. Conf. Robotics and Automation ICRA '09*, pages 1589–1590, 2009.

[KNK+09] T. Klenzner, C. C. Ngan, F. B. Knapp, H. Knoop, J. Kromeier, A. Aschendorff, E. Papastathopoulos, J. Raczkowsky, H. Wörn, and J. Schipper. New strategies for high precision surgery of the temporal bone using a robotic approach for cochlear implantation. *European Archives of Oto-Rhino-Laryngology*, 266(7):955–960, Juli 2009.

[KUK] KUKA Roboter GmbH - Kuka KR 3: Technical Data. RoMeDBKR3-02.00.02, WM-Nr. 841612-46/D+E/3/08.03. www.kuka.com.

[LBE+07] M. Leinung, S. Baron, H. Eilers, B. Heimann, S. Bartling, R. Heermann, T. Lenarz, and O. Majdani. Robotic-guided minimally-invasive cochleostomy: first results. *In GMS Current Topics in Computer- and Robot-Assisted Surgery (GMS CURAC)*, 2(1):Doc05 (20070510), 2007.

[LC87] W. E. Lorensen and H. E. Cline. Marching cubes: A high resolution 3D surface construction algorithm. *SIGGRAPH '87: Proceedings of the 14th annual conference on Computer graphics and interactive techniques*, 21:163–169, 1987.

[Leh93] E. Lehnhardt. Intracochlear placement of cochlear implant electrodes in soft surgery technique. *HNO*, 41(7):356–359, Jul 1993.

[Lei96]    S. E. Leis. Polaris calibration performance and methodology. Technical Bulletin Rev. 002, Northern Digital Inc., 1996.

[Len06]    T. Lenarz. *Cochlear Implantation. The Hannover Guideline.* Endo-Press, Tuttlingen, 2006.

[Len08]    T. Lenarz. Funktionsersatz des Innenohres. In *Medizintechnik Life Science Engineering*, pages 1401–1417. Springer Berlin Heidelberg, 2008.

[LND+08]   R. F. Labadie, J. H. Noble, B. M. Dawant, R. Balachandran, O. Majdani, and J. M. Fitzpatrick. Clinical validation of percutaneous cochlear implant surgery: Initial report. *The Laryngoscope*, 118:1031–1039, 2008.

[MA07]     M. H. Moghari and P. Abolmaesumi. Point-based rigid-body registration using an unscented Kalman filter. *IEEE Trans Med Imaging*, 26(12):1708–1728, Dec 2007.

[MBL+05]   O. Majdani, S. Bartling, M. Leinung, T. Stöver, S. Baron, H. Eilers, O. Hornung, H. Becker, B. Heimann, and T. Lenarz. The true minimally invasive approach for cochlear implantation. In *Deutsche Gesellschaft für Computer-und Roboter-Assistierte Chirurgie CURAC, CURAC Jahrestagung*, Berlin, Deutschland, 2005.

[MFW+97]   C. R. Maurer, J. M. Fitzpatrick, M. Y. Wang, R. L. Galloway, R. J. Maciunas, and G. S. Allen. Registration of head volume images using implantable fiducial markers. *IEEE Trans Med Imaging*, 16(4):447–462, Aug 1997.

[MMF93]    C. R. Maurer, J. J. McCrory, and J. M. Fitzpatrick. Estimation of accuracy in localizing externally attached markers in multimodal volume head images. volume 1898, pages 43–54. SPIE, 1993.

[MRB+09]   O. Majdani, T. S. Rau, S. Baron, H. Eilers, C. Baier, B. Heimann, T. Ortmaier, S. Bartling, T. Lenarz, and M. Leinung. A robot-guided minimally invasive approach for cochlear implant surgery: preliminary results of a temporal bone study. *International Journal of Computer Assisted Radiology and Surgery*, 2009. published online 13. 07.2009.

[MSCP+07]  M. J. Manrique, J. Savall, F. J. Cervera-Paz, J. Rey, C. Der, M. Echeverria, and M. Ares. Atraumatic surgical approach to the cochlea with a micromanipulator. *Acta Otolaryngol*, 127(2):122–131, Feb 2007.

[MSL05]    K. Martin, W. Schroeder, and B. Lorensen. VTKPointLocator Class Reference. In *VTK 5.0.4 Documentation*. Online: http://www.vtk.org/doc/release/5.0/html/a01870.html, 2005.

[MTB+09]   O. Majdani, K. Thews, S. Bartling, M. Leinung, C. Dalchow, R. Labadie, T. Lenarz, and G. Heidrich. Temporal bone imaging: comparison of flat panel volume CT and multisection CT. *AJNR Am J Neuroradiol*, 30(7):1419–1424, Aug 2009.

[MV98]     J. B. Maintz and M. A. Viergever. A survey of medical image registration. *Med Image Anal*, 2(1):1–36, Mar 1998.

[NDIa]     Northern     Digital     Inc.     NDI     Aurora     Technical     Specifications. http://www.ndigital.com/medical/aurora-techspecs-performance.php.     Accessed 05.09.2011.

[NDIb]     Northern Digital Inc. NDI Optical Measurement Technology Information. http://www.ndigital.com/medical/technology-optical.php. Accessed 05.09.2011.

[NDWL09]   J. H. Noble, B. M. Dawant, F. M. Warren, and R. F. Labadie. Automatic identification and 3D rendering of temporal bone anatomy. *Otol Neurotol*, 30(4):436–442, Jun 2009.

[NIC09]    U.S. National Institute on Deafness and Other Communication Disorders (NIDCD). NIDCD Fact Sheet - Cochlear Implants. Publication No. 09-4798, Updated August 2009.

[NIH95]    NIH consensus conference. Cochlear implants in adults and children. *JAMA*, 274(24):1955–1961, Dec 1995.

[NIH06]    U.S. National Institutes of Health. Fact Sheet - Cochlear Implants, Updated September 2006. Accessed 15.02.2010.

[NWLD08]   J. H. Noble, F. M. Warren, R. F. Labadie, and B. M. Dawant. Automatic segmentation of the facial nerve and chorda tympani in CT images using spatially dependent feature values. *Med Phys*, 35(12):5375–5384, Dec 2008.

[OWH⁺06]   T. Ortmaier, H. Weiss, U. Hagn, M. Grebenstein, M. Nickl, A. Albu-Schaffer, C. Ott, S. Jorg, R. Konietschke, L. Le-Tien, and G. Hirzinger. A hands-on-robot for accurate placement of pedicle screws. In *Proc. IEEE Int. Conf. Robotics and Automation ICRA 2006*, pages 4179–4186, 2006.

[Pol04]    Polaris tool design guide. Technical Report IL 1070071, Northern Digital Inc., 2004.

[PS02]     P. Pott and M. Schwarz. Robots, navigation, telesurgery: state of the art and market overview. *Z Orthop Ihre Grenzgeb*, 140(2):218–231, 2002.

[RDF04]    W. R. Ross, C. Dawn, and P. Fitzgerald. *Performance and Preclinical Results from a Flat-panel based Volumetric CT System*. RSNA, Chicago, IL, 2004.

[RHL⁺07]   T. S. Rau, A. Hussong, M. Leinung, H. Eilers, S. Baron, T. Lenarz, and O. Majdani. Erfassung des Krümmungsverhaltens von CI-Elektroden für die robotergestützte, minimal-traumatische Insertion. In *Tagungsband der 6. Jahrestagung der Deutschen Gesellschaft für Computer- und Roboterassistierte Chirurgie*

*e.V., CURAC 2007*, Karlsruhe, 2007.

[RHL$^+$09] T. S. Rau, A. Hussong, M. Leinung, T. Lenarz, and O. Majdani. Automated insertion of preformed cochlear implant electrodes: evaluation of curling behaviour and insertion forces on an artificial cochlear model. *International Journal of Computer Assisted Radiology and Surgery*, 2009. published online 10.04.2009.

[RHS97] I. R. Hartley and P. Sturm. Triangulation. *Comput. Vis. Image Underst.*, 68(2):146–157, 1997.

[Rog08] J. Rogowska. Overview and Fundamentals of Medical Image Segmentation. In Isaac N. Bankman, editor, *Handbook of Medical Image Processing and Analysis*, pages 73–90. Academic Press Inc, 2008.

[RSH$^+$86] D. W. Roberts, J. W. Strohbehn, J. F. Hatch, W. Murray, and H. Kettenberger. A frameless stereotaxic integration of computerized tomographic imaging and the operating microscope. *J Neurosurg*, 65(4):545–549, Oct 1986.

[SAG07] A Consensus Document on Robotic Surgery: Prepared by the SAGES-MIRA Robotic Surgery Consensus Group. Society of American Gastrointestinal and Endoscopic Surgeons (SAGES), Nov 2007. available: http://www.sages.org/publication/id/ROBOT/.

[Sch66] P. H. Schönemann. A generalized solution of the orthogonal Procrustes problem. *Psychometrika*, 31:1–10, 1966.

[SDB$^+$08] G. Strauss, E. Dittrich, C. Baumberger, M. Hofer, M. Strauss, S. Stopp, K. Koulechov, A. Dietz, and T. Lüth. Improvement of registration accuracy for navigated-control drill in mastoidectomy (autopilot). *Laryngorhinootologie*, 87(8):560–564, Aug 2008.

[SHK$^+$06] G. Strauss, M. Hofer, W. Korb, C. Trantakis, D. Winkler, O. Burgert, T. Schulz, A. Dietz, J. Meixensberger, and K. Koulechov. Accuracy and precision in the evaluation of computer assisted surgical systems. A definition. *HNO*, 54(2):78–84, Feb 2006.

[SJSS09] R. R. Shamir, L. Joskowicz, S. Spektor, and Y. Shoshan. Localization and registration accuracy in image guided neurosurgery: a clinical study. *Int J Comput Assist Radiol Surg*, 4(1):45–52, Jan 2009.

[SKA$^+$04] J. Schipper, T. Klenzner, A. Aschendorff, I. Arapakis, G. J. Ridder, and R. Laszig. Navigation-controlled cochleostomy. Is an improvement in the quality of results for cochlear implant surgery possible? *HNO*, 52(4):329–335, Apr 2004.

[SKR$^+$05] G. Strauss, K. Koulechov, R. Richter, A. Dietz, C. Trantakis, and T. Lüth. Navigated control in functional endoscopic sinus surgery. *Int J Med Robot*, 1(3):31–41, Sep

2005.

[SMDM07]  G. Strauss, J. Meixensberger, A. Dietz, and D. Manzey. Automation in surgery: a systematical approach. *Laryngorhinootologie*, 86(4):256–262, Apr 2007.

[SML06]  W. Schroeder, K. Martin, and B. Lorensen. *Visualization Toolkit: An Object-Oriented Approach to 3D Graphics*. Kitware Inc., 4th edition, 2006.

[SMME⁺89]  G. Schlöndorff, R. Mösges, D. Meyer-Ebrecht, W. Krybus, and L. Adams. CAS (computer assisted surgery). A new procedure in head and neck surgery. *HNO*, 37(5):187–190, May 1989.

[TJ03]  R. H. Taylor and L. Joskovicz. Computer-integrated surgery and medical robotics. pages 29.23–29.45. McGraw Hill, New York, 2003.

[TMFD08]  R. H. Taylor, A. Menciassi, G. Fichtinger, and P. Dario. Medical robotics and computer-integrated surgery. In *Springer Handbook of Robotics*, pages 1199–1222. Springer Berlin Heidelberg, 2008.

[TPM⁺90]  R. H. Taylor, H.A. Paul, B. D. Mittelstadt, W. Hanson, P. Kazanzides, J. Zuhars, E. Glassman, B. L. Musits, W. Williamson, and W.L. Bargar. An image-directed robotic system for precise orthopaedic surgery. In *Proc. Twelfth Annual Int Engineering in Medicine and Biology Society Conf. of the IEEE*, pages 1928–1930, 1990.

[TZG96]  G. Taubin, T. Zhang, and G. H. Golub. Optimal surface smoothing as filter design. In *ECCV (1)*, pages 283–292, 1996.

[Wal45]  A. Wald. Statistical decision functions which minimize the maximum risk. *The Annals of Mathematics*, 46(2):265–280, 1945.

[Wei10]  M. Weinstein. Vergleich von 3D-Segmentierungen des Gesichtsnervs aus CT und Schliffbildgebung. Study thesis, University of Hannover, Institute of Mechatronic Systems, 2010. Unpublished.

[Wes09]  G. Wessels. Medizinische Bildgebung. In *Medizintechnik - Life Science Engineering*, pages 1071–1111. Springer Berlin Heidelberg, 2009.

[WLFP08]  A. D. Wiles, A. Likholyot, D. D. Frantz, and T. M. Peters. A statistical model for point-based target registration error with anisotropic fiducial localizer error. 27(3):378–390, March 2008.

[WTF04]  A. D. Wiles, D. G. Thompson, and D. D. Frantz. Accuracy assessment and interpretation for optical tracking systems. In Robert L. Galloway Jr., editor, *Medical imaging 2004: Visualization, Image Guided Procedures, and Display*, volume 5367, pages 421–432, San Diego, CA, USA, 2004. SPIE.

[Zen07]  H.-P. Zenner. Die Kommunikation des Menschen: Hören und Sprechen. In *Physiologie des Menschen*, Springer-Lehrbuch, pages 343–366. Springer Berlin Heidelberg, 2007.

[ZWM$^+$08]  J. Zhang, W. Wei, S. Manolidis, J. T. Roland Jr., and N. Simaan. Path planning and workspace determination for robot-assisted insertion of steerable electrode arrays for cochlear implant surgery. In *MICCAI '08: Proceedings of the 11th International Conference on Medical Image Computing and Computer-Assisted Intervention, Part II*, pages 692–700, Berlin, Heidelberg, 2008. Springer-Verlag.

# A Curriculum Vitae

| **Anschrift** | Hubertus Eilers |
| | Oststr. 5 |
| | 49176 Hilter a.T.W. |
| **Geburtsdatum** | 05.11.1977 |

## Schulausbildung

| 1984 - 1988 | Grundschule Glane |
| 1988 - 1990 | Orientierungsstufe Bad Iburg |
| 1990 - 1997 | Gymnasium Bad Iburg |

## Hochschulausbildung

| 10/1998 - 04/2004 | Maschinenbaustudium, Studienrichtung Mechatronik |
| | Gottfried Wilhelm Leibniz Universität Hannover |
| 09/1998 - 10/1998 | Praktikum |
| | Wilhelm Karmann GmbH, Osnabrück |
| 11/2002 - 01/2003 | Praktikum |
| | Airbus Deutschland GmbH, Hamburg |
| 02/2003 - 05/2003 | Gastwissenschaftler |
| | University of Alberta, Edmonton, Kanada |
| 06/2003 - 08/2003 | Praktikum |
| | Wilhelm Karmann GmbH, Osnabrück |

## Berufliche Tätigkeit

| 06/2004 - 07/2010 | Wissenschaftlicher Mitarbeiter |
| | Institut für Mechatronische Systeme (bis 12/2008: Institut für Robotik) |
| | Gottfried Wilhelm Leibniz Universität Hannover |
| seit 11/2010 | Technologie Consultant |
| | SALT AND PEPPER Nord GmbH & Co. KG |